



Université Claude Bernard Lyon 1



THÈSE de DOCTORAT DE L'UNIVERSITÉ DE LYON
Opérée au sein de :
l'Université Claude Bernard Lyon 1

Ecole Doctorale N° 512
Informatiques et Mathématiques

Spécialité de doctorat :
Neurosciences computationnelles

Soutenue publiquement le jj/mm/aaaa, par :
Arnaud Hubert

**Endocannabinoid-mediated synaptic plasticity
and its implication in fast learning**

A numerical and mean-field model approach

Devant le jury composé de :

Julijana, Gjorgjeva	Rapporteure
Tenured Professor, Technical University of Munich	
Laure, Buhry	Rapporteure
Maître de Conférence & HDR, IDMC, Université de Lorraine	
Andrew, Davison	Examinateur
Chargé de Recherche, Neuroinformatique , CNRS Paris-Saclay	
Matteo, Di Volo	Examinateur
Professor & HDR, Stem cell & Brain Research Institute , Inserm Lyon	
Hugues, Berry	Directeur de thèse
Directeur de Recherche, AIstroSight, Inria Lyon	
Responsable du Pôle IA & Numérique, Inserm	



List of Scientific Production

Preprint

Striatal endocannabinoid-long-term potentiation mediates one-shot learning

Charlotte Piette, Arnaud Hubert, Sylvie Perez, Hugues Berry, Jonathan Touboul, Laurent Venance

[bioRxiv2024.07.10.602953;doi:<https://doi.org/10.1101/2024.07.10.602953>](https://doi.org/10.1101/2024.07.10.602953)

Communication

Exploring behavioral correlations with neuron activity through synaptic plasticity (Poster).

Arnaud Hubert, Charlotte Piette, Hugues Berry, Laurent Venance, Jonathan Touboul

Bernstein Conference, Frankfurt am Main. September, 29 - October, 2, 2024

https://gitlab.inria.fr/ahubert/poster-bernstein-conference-2024/-/blob/main/poster_Bernstein_VF_HR3.png

Reconstructing Large-Scale Heterogeneous Quadratic-Integrate-and-Fire Networks Using Their Dominant Modes (Conference Paper)

Arnaud Hubert, Hugues Berry

International Conference on Computational and Mathematical Neuroscience , Paris. September, March 30 - March 31, 2026

Code repository

Synacomp

Arnaud Hubert, Jan-Michael Rye

https://gitlab.inria.fr/aistrosight/synacomp/-/tree/v2025.1?ref_type=tags

Titre: Plasticité endocannabinoïdienne et son implication dans l'apprentissage rapide. Une approche numérique et de champs moyens.

mots clefs: neurosciences computationnelles, apprentissage rapide, modèle mécanistique, modèle de champs moyen, synacomp.

Résumé: L'apprentissage et la mémoire comptent parmi les capacités les plus remarquables du cerveau. Ils permettent aux organismes d'adapter leur comportement à des environnements en perpétuelle évolution. Qu'il s'agisse de naviguer dans l'espace ou d'acquérir des compétences sensori-motrices, les expériences passées sont intégrées afin de guider les actions futures. Il est désormais bien établi que l'apprentissage repose de manière critique sur la plasticité synaptique — la capacité des synapses à se renforcer ou à s'affaiblir au fil du temps en réponse à des motifs d'activité neuronale. Comprendre comment ces capacités cognitives s'appuient sur un substrat physique — connu sous le nom d'engramme — demeure l'un des défis centraux des neurosciences.

Traditionnellement, l'apprentissage a été conceptualisé comme un processus incrémental, les expériences répétées consolident progressivement des changements durables de la force synaptique, conformément à la théorie hebbienne. Cependant, le comportement repose également sur des formes complémentaires d'apprentissage. L'une d'elles est l'**apprentissage rapide** ou **one-shot learning**, par lequel une seule expérience brève suffit à induire des changements durables. Une question fondamentale est de savoir quels mécanismes synaptiques et circuits soutiennent une telle adaptation rapide. Alors que l'apprentissage incrémental a été associé à une plasticité dépendante des récepteurs NMDA, l'apprentissage rapide semble reposer sur des voies alternatives, dotées de signatures temporelles distinctes, parmi lesquelles le système endocannabinoïde (eCB) est apparu comme un candidat majeur.

En parallèle, les neurosciences théoriques ont développé de puissants cadres mathématiques et computationnels pour formaliser la dynamique des circuits et des synapses neuronaux. Des modèles de champ moyen décrivant de larges populations de neurones à potentiel d'action, aux modèles biochimiques mécanistes des cascades de signalisation, ces approches offrent des éclairages complémentaires à différentes échelles, microscopiques et macroscopiques, ainsi que sur leurs interactions. Pourtant, relier les enregistrements neuronaux *in vivo*, les modèles biophysiques de plasticité synaptique et les descriptions abstraites au niveau populationnel demeure un défi ouvert.

Cette thèse est consacrée à l'exploration de ces questions selon deux axes principaux. À l'échelle microscopique, par une approche conjointe expérimentale et computationnelle, impliquant un modèle mécaniste de la synapse. À l'échelle macroscopique, par une approche théorique fondée sur le modèle de champ moyen, visant à capturer quelles caractéristiques émergent au niveau du réseau. Chacun de ces axes correspond à un chapitre dédié de cette thèse, organisé comme suit :

1. **Chapitre 1 : Prémices.** Nous proposons une introduction générale aux neurosciences computationnelles et présentons deux articles fondateurs sur lesquels se construit le travail ultérieur.
2. **Chapitre 2 : Exploration de l'hypothèse de l'engramme endocannabinoïde pour le one-shot learning à travers des simulations.** En nous appuyant sur le modèle biophysique de Cui *et al.* (2016) [21], nous étudions comment la voie eCB peut servir d'engramme pour l'apprentissage rapide. À l'aide d'enregistrements Neuropixel lors d'un nouveau paradigme comportemental (la tâche d'évitement du ruban adhésif), nous intégrons des données expérimentales avec des simulations afin d'inférer des dynamiques synaptiques inaccessibles *in vivo*. Pour cela, nous avons développé **Synacomp**, un cadre computationnel permettant l'analyse systématique de la plasticité cortico-striatale au niveau synaptique.
3. **Chapitre 3 : Reconstruction de réseaux de neurones de type "Quadratic-Integrate-and-Fire" avec poids synaptiques hétérogènes, à partir de leurs modes dominants.** Nous étendons la théorie de champ moyen introduite par Montbrió, Pazó et Roxin. En partant de leur ansatz lorentzien, qui permet une description de faible dimension de réseaux de neurones quadratiques à intégration-décharge, nous incorporons une hétérogénéité synaptique individuelle. Ce travail vise à ouvrir la voie à l'inclusion d'une règle de plasticité au sein du réseau. À terme, un tel cadre pourrait aider à comprendre comment la connectivité neuronale façonne la dynamique populationnelle.
4. **Annexe :** Nous fournissons des étapes intermédiaires supplémentaires soutenant les calculs présentés au Chapitre 1.

Ensemble, ces deux perspectives complémentaires visent à éclairer les processus multi-échelles qui soutiennent l'apprentissage rapide dans le cerveau. D'une part, nous proposons que le système endocannabinoïde constitue un substrat biologique de l'apprentissage rapide dans les circuits cortico-striataux. D'autre part, nous clarifions les conséquences mathématiques de l'introduction d'une hétérogénéité synaptique dans les modèles de population, préparant ainsi la voie à la compréhension de la manière dont l'apprentissage rapide pourrait également émerger au niveau du réseau.

Contents

Résumé en Français	iii
Introduction	xii
1 Premises	1
1.1 Biological Foundations	1
1.1.1 Neurons: The Fundamental Computational Units	1
1.1.2 Ion Channels	2
1.1.3 Action Potential: The Electrical Basis of Communication	3
1.1.4 Synapses: The Gate of Communication	4
1.1.5 Synaptic Plasticity	5
1.1.6 Learning	6
1.2 Computational Models	7
1.2.1 Neuron Models	8
1.2.1.1 Types of Neuronal Excitability	9
1.2.1.2 Conductance-Based Models: The Hodgkin–Huxley Formalism	9
1.2.1.3 Leaky Integrate-and-Fire (LIF) Model	11
1.2.1.4 Quadratic Integrate-and-Fire (QIF)	12
1.2.1.5 Theta Neuron	14
1.2.2 Neural Mass Models	14
1.2.2.1 Population Model: Wilson–Cowan	15
1.2.3 Mean field model	16
1.2.4 STDP model	18
1.2.4.1 Biphasic Spike-Timing-Dependent Plasticity (STDP)	18
1.2.4.2 Graupner Brunel STDP	19
1.3 Montbrió–Pazó–Roxin (2015) and the Lorentzian Ansatz	20
1.4 eCB Fast learning	23
1.4.1 The mystery of fast learning	23
1.4.2 Graupner–Brunel CaMKII Model	23
1.4.3 The diversity of synaptic plasticity	27
1.5 Conclusion	32
2 Exploring the Endocannabinoid Engram Hypothesis for One Shot Learning Through Simulations	35
2.1 Introduction	35
2.1.1 Numerical Simulation as a Window into In Vivo Plasticity	36
2.1.2 Model Overview	37
2.2 ExperimentCuial Setup	38

CONTENTS

2.2.1	The sticky tape avoidance task	38
2.2.2	Raw Data Processing	40
2.2.2.1	Spike sorting.	41
2.2.2.2	Manual curation.	42
2.2.2.3	Anatomical localization.	42
2.2.2.4	Cortical interneuron filtering.	42
2.3	Adaptation and Application of the Synaptic Plasticity Model to In Vivo Data: Methods and Results	43
2.3.1	Numerical Implementation	44
2.3.2	In Vivo / Ex Vivo Challenges	44
2.3.3	Post-synaptic weight study	45
2.3.4	All to one connection	49
2.3.4.1	Exploring glutamate release	50
2.3.4.1.1	pre-synaptic activity only.	50
2.3.4.1.2	For all synapses.	51
2.3.5	One to one connection	55
2.3.5.1	Active pairs definition	57
2.3.5.2	Parameters modification	58
2.3.5.3	Results for NMDA pathway	59
2.3.5.4	Method for eCB pathway: The plasticitymeter	60
2.3.5.5	Results for eCB pathway	63
2.4	Additional Exploratory Directions	68
2.4.1	Using LFP information	68
2.4.2	On neuron and synaptic specialization	69
2.5	Python Package: Synacomp	69
2.6	Conclusion	71
3	Reconstructing Large-Scale Heterogeneous Quadratic-Integrate-and-Fire Networks Using Their Dominant Modes.	75
3.1	Introduction	75
3.2	From Global to Pairwise Synaptic Heterogeneity	76
3.3	Introducing Heterogeneity	78
3.4	Modal Decomposition	79
3.5	Numerical comparison	80
3.6	Code and Simulation Details	81
3.6.1	Simulations details	82
3.7	A Hint on Bifurcation	83
3.8	Conclusion and Discussion	85
	General Discussion, Conclusion and Perspectives	87
	Annexe	91
	Annexe	91
	Trivial solutions	91
	Firing rate	91
	Mean membrane potential	92
	Mean membrane potential	92
	Special case of Lorentzian excitability	93
	Solved firing rate	94

List of Figures

1.1	Basic structure of a neuron	2
1.2	Phases of the action potential	3
1.3	Electrical circuit representation of the Hodgkin-Huxley model	10
1.4	Electrical circuit representation of the LIF model	12
1.5	Schematic representation of the Wilson–Cowan model	16
1.6	Biphasic response of plasticity	18
1.7	CaMKII pathway, and subunit configurations. From Graupner & Brunel, 2007 [40]	24
1.8	Bifurcation diagramm of total phophorylated CaMKII. From Graupner & Brunel, 2007 [40]	26
1.9	Biological model proposed by Cui <i>et al.</i> 2016 [21]	28
2.1	Summary of <i>ex vivo</i> and <i>in vivo</i> context	37
2.2	STDP map produced by the model from Cui <i>et al.</i> 2016 [21]	38
2.3	Mice trajectory and avoidance index for STA. Adapted from Piette <i>et al.</i> (2024) [83]	39
2.4	Mice performance at STA task. Adapted from Piette <i>et al.</i> (2024) [83]	40
2.5	Neuropixel recording setup. Adapted from Piette <i>et al.</i> (2024) [83] . .	41
2.6	Number of spikes per sorted neuron. From Piette <i>et al.</i> 2024 [83] . . .	43
2.7	Experimental conditon and model abstraction of synaptic stimulation	45
2.8	Stable state of PP1 & IP1	46
2.9	Bifurcation diagrams of total phosphorylated CaMKII for the model parameters	46
2.10	Illustration of UP to DOWN transition	47
2.11	Illustration of DOWN to UP transition	48
2.12	Exploration tree for Glu_{\max} value for pre-activity only	51
2.13	Exploration tree for Glu_{\max} value, all-to-one connection	53
2.14	Mean post-synaptic weight by mice, all-to-one connection	56
2.15	Mean pre-synaptic weight by mice, all-to-one connection	56
2.16	Illustration of paired spike and active pairs definition. From Piette <i>et al.</i> 2024 [83]	58
2.17	Number of paired spikes per neurons pairs. From Piette <i>et al.</i> 2024 [83]	59
2.18	Percentage of synapses in the UP state over time, shown for all synaptic pairs (blue) and for the active pairs only (red), for each mouse. Dotted vertical lines indicate the start and end of the contact period.	60
2.19	Illustration of pre-synaptic weight model output	62
2.20	Main plasticitymeter results. Adapted from Piette <i>et al.</i> 2024 [83] . .	64
2.21	Additional plasticitymeter results. Adapted from Piette <i>et al.</i> 2024 [83]	65

LIST OF FIGURES

2.22	Plastitime	66
2.23	Mice performance with impaired eCB pathway. From Piette <i>et al.</i> 2024 [83]	67
2.24	Performance index up to second retrieval session. From Piette <i>et al.</i> 2024 [83]	67
2.25	Plasticitymeter and firing for specialized subgroup of synapses	70
2.26	Schematic overview of the Synacomp package architecture	71
2.27	Synacomp : YAML configuration file defining model parameters and mouse assignments	74
2.28	Synacomp : YAML configuration file defining a Mouse object	74
3.1	Eigenvectors (blue curves) and their eigen-values (top right corner val- ues), of connectivity matrix used for simulations, defined in Eq 3.14 with $R = 10$, $J_{\max} = 15$. Eigenvectors correspond to the discrete Fourier basis, whose profiles exhibit sinusoidal oscillations with in- creasing spatial frequency. The $k = 0$ mode, associated with the largest eigenvalue ($\lambda_0 = 15$), represents a nearly homogeneous activ- ity pattern across populations.	81
3.2	A–B. Comparison between the full heterogeneous QIF simulation, the full MPR population model, and the truncated modal reconstruction. The modal approach faithfully reproduces the time evolution of both the mean firing rate $r(t)$ and the mean membrane potential $v(t)$ across the network for multiple types of external input: (A) constant and (B) sinusoidal.	82
3.3	Spatiotemporal dynamics of the firing rate across populations for the full QIF network under constant external input. The dominant pat- terns observed are accurately reconstructed using only the first ten synaptic modes.	83
3.4	A–B. Comparison between the full heterogeneous QIF simulation, the full MPR population model, and the truncated modal reconstruc- tion under non-circulant connectivity and sinusoidal input. A small change in the total synaptic strength ($J_{\max} = 15$ in A, $J_{\max} = 13$ in B) induces a qualitative change in network dynamics, which is captured by the reduced modal system.	84

List of Tables

2.1	Number of sorted cluster per mice	43
2.2	Number of spikes by neuron for each mice	51
2.3	Number of pairs, one-to-one connection	57

Introduction

Learning and memory are among the most remarkable capabilities of the brain. They allow organisms to adapt their behavior to ever-changing environments. From navigating in space to acquiring sensorimotor skills, past experiences are integrated in order to guide future actions. It is now well established that learning rely critically on synaptic plasticity – the ability of synapses to strengthen or weaken over time in response to patterns of neural activity. Understanding how these cognitive and procedural capabilities rely on a physical substrate – known as the engram [91] – remains one of the central challenges of neuroscience.

Traditionally, learning has been conceptualized as an incremental process: repeated experiences progressively consolidate long-lasting changes in synaptic strength, in accordance with Hebbian theory [44]. This paradigm has been extensively studied in rodents, typically performing maze-based learning tasks, where evidence of learning emerges only after dozens of trials. However, behavior also relies on complementary forms of learning. One of them is fast or one-shot learning, in which a single, brief experience is sufficient to form durable changes [84]. A fundamental question is which synaptic and circuit mechanisms support such rapid adaptation. While incremental learning has been linked to NMDA receptor-dependent plasticity [60], fast learning appears to rely on alternative pathways with distinct temporal signatures, among which the endocannabinoid (eCB) system has emerged as a strong candidate [84].

In parallel, theoretical neuroscience has developed powerful mathematical and computational frameworks to formalize the dynamics of neural circuits and synapses. From mean-field models describing large populations of spiking neurons to mechanistic biochemical models of signaling cascades, such approaches provide complementary insights across microscopic and macroscopic scales, as well as their interactions. Yet, bridging the gap between *in vivo* neural recordings, biophysical models of synaptic plasticity, and abstract population-level descriptions remains an open challenge.

This thesis is devoted to exploring these questions through two main axes. At a microscopic scale with a joint experimental and computational approach, involving a mechanistic model of synapse. At a macroscopic scale, with a theoretical approach of mean-field model, that aims to capture which characteristic emerges at the network level. Each of these axes corresponds to a dedicated chapter of this thesis, organized as follows:

1. **Chapter 1: Premises.** We provide a general introduction to computational neuroscience and present two foundational articles upon which the subsequent work is built.
2. **Chapter 2: Exploring the Endocannabinoid Engram Hypothesis for**

One Shot Learning Through Simulations. Building upon the biophysical model of Cui *et al.* (2016) [21], we investigate how the eCB pathway can serve as an engram for rapid learning. Using Neuropixel recordings during a novel behavioral paradigm (the sticky tape avoidance task), we integrate experimental data with simulations to infer synaptic dynamics that remain inaccessible *in vivo*. To achieve this, we developed **Synacomp**, a computational framework that enables the systematic analysis of cortico-striatal plasticity at the synaptic level.

3. **Chapter 3: Reconstructing Large-Scale Heterogeneous Quadratic-Integrate-and-Fire Networks Using Their Dominant Modes.** We extend the mean-field theory introduced by Montbrió, Pazó, and Roxin. Starting from their Lorentzian ansatz, which enables a low-dimensional description of quadratic integrate-and-fire networks, we incorporate one-to-one synaptic heterogeneity. This work aims to pave the way for the inclusion of a plasticity rule within the network. Ultimately, such a framework could help capture how neural connectivity shapes population dynamics.
4. **Annexe:** We provide additional intermediate steps supporting the calculations presented in Chapter 1.

Together, these two complementary perspectives aim to shed light on the multi-scale processes that support fast-learning in the brain. On the one hand, we propose that the endocannabinoid system provides a biological substrate for fast-learning in cortico-striatal circuits. On the other, we clarify the mathematical consequences of introducing synaptic heterogeneity into population models, preparing the way to understand how fast-learning could emerge also from a network level.

Chapter 1

Premises

Il vaut mieux savoir un peu de tout que tout sur très peu.

Blaise Pascal

1.1 Biological Foundations

Understanding the brain as a computational system is a fundamental challenge in neuroscience. The study of how neurons process information, communicate, and adapt through plasticity mechanisms has led to significant advancements in both theoretical neuroscience and artificial intelligence. This chapter introduces the biological foundations needed to understand the basic mechanisms in neuroscience [45], followed by a presentation of the mathematical tools and models used in the field.

1.1.1 Neurons: The Fundamental Computational Units

Neurons are the basic computational elements of the nervous system. They receive, process, and transmit information through **synapses**, using **electrical** and **chemical signals**. The vast interconnected networks they form, underlie cognition, perception, and behavior. The brain contains approximately 86 billion neurons [5], each forming thousands of synaptic connections. There exists a large diversity of neuronal types, with important morphological and functional variations across brain regions. Here we briefly recall the most common structure of a neuron, illustrated Fig 1.1.

Neuron structure consists of:

- **Cell body (Soma):** The metabolic hub containing the nucleus and essential organelles. The cell membrane of the soma integrates incoming signals and determines whether to generate an output signal known as **action potential**.
- **Dendrites:** Tree-like extensions that end in very small protrusions, containing many neurotransmitter receptors. They receive signals from other neurons and convey them to the cell body.
- **Axon:** A long projection that propagates action potentials toward other neurons.

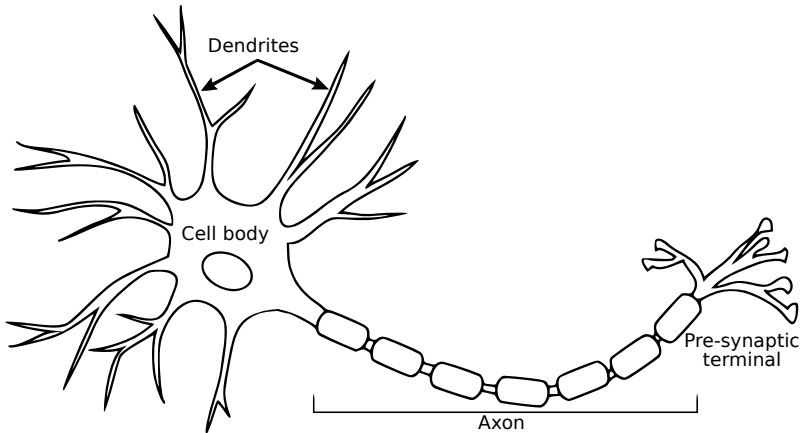


Figure 1.1: Basic structure of a neuron. From <https://openbooks.lib.msu.edu/neuroscience/chapter/the-neuron/> (CC-BY-NC-SA) 4.0 International License.

1.1.2 Ion Channels

The cell membrane, while separating the inside of the cell from the outside, is still permeable. A wide range of ion transfers occurs at the membrane. These transfers are made possible by the presence of **ion channels**.

There are numerous types of ion channels, each defining specific rules of permeability. Here, we list some of the major types:

- **Leak channels:** These channels are constantly open, allowing a continuous transfer of ions until an electrochemical equilibrium is reached. The presence of leak channels explains the resting membrane potential of approximately -65 mV. This value arises from the differential permeability to ions such as potassium (with an equilibrium potential around -80 mV) and sodium (around $+60$ mV), as well as their concentration gradients [38]. The Nernst equation is used to determine these equilibrium potentials [113].
- **Voltage-gated channels:** These channels are sensitive to changes in membrane potential. They typically open or close depending on whether a threshold voltage is reached. The initial variation in membrane potential can result from ion flux through other channels or from the back-propagation of an action potential.
- **Ligand-gated channels:** These channels open in response to the binding of a ligand, which induces a conformational change in the channel structure. Most ligands are neurotransmitters. Notably, AMPA and NMDA receptors are two main types of ligand-gated ion channels activated by the neurotransmitter glutamate.
- **Ion pumps and transporters:** While not channels strictly speaking, pumps such as the Na^+/K^+ -ATPase or Ca^{2+} -ATPase play a crucial role in maintaining ionic gradients across the membrane. After an action potential, they actively restore the resting membrane potential against the concentration gradients. To operate, they consume Adenosine Triphosphate (ATP) as an energy source [78].

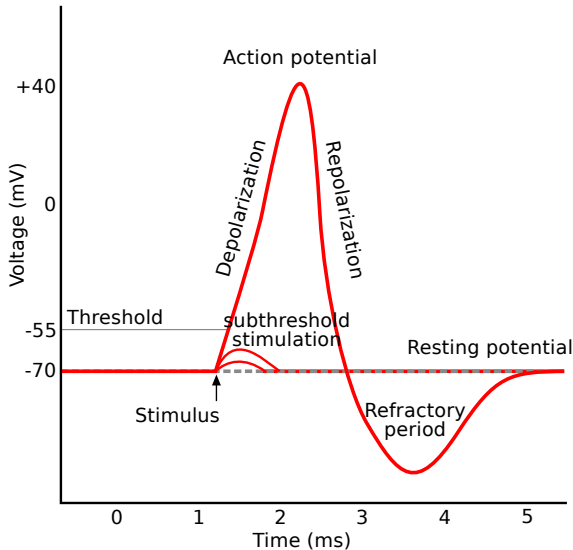


Figure 1.2: Phases of the action potential. Adapted from the original by en:User:Chris 73, updated by en:User:Diberri, converted to SVG by tiZom - Own work, CC BY-SA 3.0, <https://commons.wikimedia.org/w/index.php?curid=2241513>

1.1.3 Action Potential: The Electrical Basis of Communication

Neurons communicate through action potentials, rapid and prototypical electrical impulses initiated when the membrane potential crosses a specific threshold.

Three main phases, illustrated Fig 1.2, characterize the formation of an action potential:

- **Depolarization (Rising phase):** When the membrane potential reaches a threshold, voltage-gated sodium channels open, allowing a large influx of positively charged sodium ions. This depolarizes the membrane and initiates the propagation of an electrical impulse along the axon.
- **Repolarization (Falling phase):** Shortly after, voltage-gated potassium channels open while sodium channels become inactivated. The efflux of potassium ions causes a rapid repolarization of the membrane potential.
- **Refractory period & Rest:** Both sodium and potassium channels close, returning to a state where they are ready to be activated again. However, potassium continues to flow out briefly, leading to a transient hyperpolarization known as the undershoot. Leak channels and ionic pump then restore the membrane potential to its resting level.

As mentioned above, sodium channels undergo an inactivation period during which they cannot reopen, regardless of the membrane potential. This gives rise to the concept of the **refractory period**, which includes an absolute phase during which the neuron cannot fire another action potential.

The generated action potential travels along the axon and reaches the dendrites of other neurons at specialized junctions called synapses. There, it may trigger the

release of neurotransmitters and propagate a signal to the post-synaptic neuron. The multiple inputs received via dendrites are integrated by the post-synaptic neuron, resulting in changes in its membrane potential that may, in turn, initiate a new action potential—thus continuing the cycle of neural communication.

1.1.4 Synapses: The Gate of Communication

Synapses form the interface between neurons, enabling the transfer of information. They are generally classified into two types:

- **Chemical synapses:** These represent the vast majority (>99%) of synapses in the mammalian brain. For an adult human brain, their number in the neocortex region alone is estimated at around 164×10^{12} [103], compared to approximately 8.1×10^{10} for mouse [92]. The incoming electrical signal is converted into a chemical signal at the synaptic junction, and then reconverted into an electrical signal in the post-synaptic neuron. Transmission through chemical synapses takes about 1–5 ms. These synapses are thought to be central to learning and adaptation processes.
- **Electrical synapses:** These allow direct signal transmission via ion flow between neurons. They are faster, with transmission times typically under 1 ms, and are often involved in synchronization of neuronal activity.

Chemical synapses rely on the release of neurotransmitters, triggered by an action potential arriving at the presynaptic terminal. This event initiates a cascade of reactions, collectively known as a **signaling pathway**, which can either lead to the direct opening of ion channels (ionotropic transmission) as NMDA, AMPA or GABA-A receptors; or to the activation of **metabotropic** receptors. These receptors are not ion channels directly, but modulate them via intracellular signaling cascades. We can denote mGlu, dopamine or GABA-B as such receptors. Both mechanisms ultimately influence the post-synaptic membrane potential and excitability, either rapidly via electrochemical gradients or more slowly through biochemical modulation.

Depending on the nature of the pathway involved, this can produce:

- an **excitatory post-synaptic potential (EPSP)** through depolarization, increasing the likelihood of an action potential in the post-synaptic neuron;
- an **inhibitory post-synaptic potential (IPSP)** through hyperpolarization, decreasing that likelihood.

Key **neurotransmitters** and their primary functions include:

- **Glutamate:** The main excitatory neurotransmitter.
- **GABA:** The principal inhibitory neurotransmitter.

The complex interplay of EPSPs, IPSPs, and action potentials at the level of individual neurons enables highly precise and dynamic communication. When neurons are organized into networks, the diversity of possible computations and emergent dynamics increases exponentially.

1.1.5 Synaptic Plasticity

Complex mechanisms such as firing rate propagation and network organization of neurons already allow the brain to perform sophisticated tasks and generate dynamic activity. However, one of the brain's major strengths lies in its capacity to adapt and learn. To support this, it must undergo long-lasting changes that enable new capabilities to emerge. These modifications occur primarily at the synaptic level. The ability of synapses to change over time is known as **synaptic plasticity**.

This dynamic process allows neurons to adjust their connectivity and activity. The concept of **synaptic weight** (also referred to as **synaptic efficacy** or **synaptic strength**) is used to quantify this adjustment. A change in synaptic weight means that a given pre-synaptic stimulation can produce different post-synaptic responses across repetitions. This concept integrates well with the experimental context, as variations in post-synaptic response amplitude can be directly measured, relatively to a baseline, giving synaptic plasticity a measurable dimension.

It is now established that changes in synaptic weight directly result from various forms of learning and memory, forming its biological basis [49, 65].

These changes can vary in nature, location, and duration. As described by Malenka & al. (2004) [62], several classifications can be used to specify plasticity mechanisms:

- **Long-Term Potentiation (LTP):** A lasting increase in synaptic strength. It is commonly subdivided into an early phase, which typically persists for up to about 60 minutes, and a late phase, which requires protein synthesis and can persist for days or longer.
- **Long-Term Depression (LTD):** A lasting decrease in synaptic strength. Similar to LTP, LTD can also be subdivided into early and late phases.

More specific canonical mechanisms can also be identified [17, 117].

- **Pathway-specific plasticity:** The synaptic changes can be mediated by specific molecular pathway. These will be addressed later.
- **Short-term synaptic facilitation:** A group of transient increases in synaptic strength, including facilitation, augmentation, and potentiation. These effects range from a few milliseconds to a few seconds and can result from increased neurotransmitter release or the occurrence of miniature EPSPs.
- **Short-term synaptic depression:** Also called synaptic fatigue, this occurs when the neurotransmitter pool is temporarily depleted. Despite the existence of a reserve pool and recycling mechanisms, exhaustion of available neurotransmitter can impair EPSP generation.

Concretely, plasticity can result from changes in the amount of neurotransmitter released (presynaptic mechanisms) [117] or in the number and sensitivity of post-synaptic receptors (post-synaptic mechanisms) [10]. Depending on the site of modification, we distinguish between **pre-synaptic weight** and **post-synaptic weight**. In many contexts, it is useful to refer to a specific form of plasticity in order to focus on the underlying biological pathway. Detailed mechanisms at both synaptic sites will be discussed in later sections.

Experience-dependent plasticity refers to synaptic modifications that arise as a consequence of neural activity patterns linked to an individual’s experiences [17, 32]. A canonical example is the **Hebbian theory** [44]: if a pre-synaptic neuron consistently fires just before a post-synaptic neuron, the strength of their synapse increases. Conversely, in the absence of such temporal correlation, the connection may weaken.

In addition, recent studies have revealed the significant role of glial cells—particularly astrocytes—in modulating synaptic plasticity. Astrocytes can release gliotransmitters that influence neuronal activity, adding a new dimension to the regulation of plasticity and contributing to the adaptability of the neural network [3, 100].

These mechanisms enable the nervous system to adapt to new experiences and optimize its responses to environmental stimuli, forming the biological foundation for complex behaviors and cognitive functions. Processes of synaptic modification are thought to underlie higher-order capacities such as pattern recognition, motor learning, and long-term memory consolidation. In computational neuroscience, these processes are often modeled to investigate the underlying algorithms that govern learning and adaptation in neural networks.

1.1.6 Learning

Learning processes can be categorized based on how experiences are integrated over time. In this context, **incremental learning** and **fast learning** are two fundamental forms that differ primarily in the number of exposures required for memory consolidation.

Incremental learning refers to the gradual accumulation of knowledge through repeated experiences. It typically involves multiple trials to reinforce synaptic changes and progressively improve performance. This form of learning is closely associated with long-term synaptic plasticity mechanisms. Through repeated exposure, synaptic efficacy is enhanced over time, leading to the consolidation of learned information, in accordance with Hebbian theory [60].

In contrast, **fast learning** – often referred to as **one-shot learning** – occurs when a memory is formed after a single, brief experience. This type of learning is essential in situations requiring immediate behavioral adaptation, such as avoiding a painful stimulus or uncomfortable situation, after one encounter [31, 84]. Researchers often aim to identify the physical substrate that encodes a memory trace, known as **engram**. It can refer for examples to a specific ensemble of neurons undergoing lasting biochemical or structural changes [91]. In a one-shot learning context, the engram formed relies on sparse and transient firing events that are nevertheless sufficient to induce robust, long-lasting synaptic modifications, without requiring the multiple repetitions typical of incremental learning.

In this thesis, we present further evidence suggesting that **endocannabinoid-mediated long-term potentiation (eCB-LTP)** is a strong candidate mechanism underlying the engram of fast learning. This hypothesis will be explored in greater detail in subsequent chapters.

One of the main challenges in studying these types of learning lies in identifying the specific neural circuits involved in each. Incremental learning is associated with multiples brain structures such as the neocortex [39], hippocampus [60] or basal ganglia [115], which undergo gradual adaptations through repeated experience. In

contrast, fast learning involves rapid synaptic changes in circuits such as the dorsal striatum [42], where eCB-LTP plays a pivotal role [82]. This synaptic remodeling is believed to occur in response to sparse neural activity, allowing the system to encode a memory trace with minimal input.

The distinctions between incremental- and fast-learning suggests that they are governed by distinct molecular pathways and signaling networks, a realization that opens up promising avenues for targeted therapeutic strategies in the treatment of cognitive and learning disorders.

1.2 Computational Models

Building upon the biological foundations previously discussed, computational models use mathematical frameworks to systematically describe, interpret, and predict neural phenomena. Mathematics provides essential tools for abstracting biological complexity, transforming intricate cellular interactions and neural circuitry into formal representations that support rigorous analysis and simulation [22, 47].

With the emergence of computational neuroscience as a distinct discipline, and the increasing integration of fields such as computer science, mathematics, and physics, computational approaches have demonstrated their capacity not only to formalize and confirm empirical findings, but also to guide experimental design and open new avenues of research. Mathematical models are not universal solutions. Neural activity spans multiple spatial and temporal scales, and our understanding of biological reality remains limited by current experimental techniques.

Several axes can be used to characterize different modeling approaches, providing a framework to understand what a model can or cannot do. These axes are, of course, non-exhaustive and may overlap or be combined in various ways.

Foundational Approach:

- **Mechanistic models:** Built upon detailed biological knowledge, these models aim to faithfully simulate biological processes.
- **Phenomenological models:** Designed to reproduce or emulate specific features or behaviors of neural dynamics, without the necessity of direct biological grounding.

Scale of Modeling:

- **Microscopic:** Models that describe individual components, such as a single neuron (e.g., Hodgkin-Huxley, QIF) or a synapse.
- **Mesoscopic:** Models that describe populations of neurons or local circuits (e.g., Wilson-Cowan).
- **Macroscopic:** Models that capture large-scale brain activity, including inter-regional interactions and whole-brain connectivity (e.g., connectome-based modeling).

Modeling Purpose:

- **Descriptive (What):** Aimed at capturing empirical data accurately. Descriptive models are often a first step, but do not necessarily imply mechanistic understanding.

- **Predictive (How):** These models seek to anticipate the outcome of experiments, especially when direct measurements are not feasible. They also help guide experimental design by identifying relevant variables.
- **Explanatory (Why):** These models aim to uncover underlying mechanisms or principles, such as optimization strategies, that drive observed dynamics. They not only predict outcomes but also provide insight into the intermediate steps leading to them, making them valuable for hypothesis generation and clinical applications.

This integration is typically achieved using differential equations to model neuronal firing and synaptic dynamics, probabilistic frameworks to interpret neural data, and graph theory to analyze network architecture and functional connectivity [6,24]. Furthermore, advanced tools such as dynamical systems theory, stochastic modeling, and machine learning algorithms enhance the predictive power of computational models, allowing the simulation of diverse experimental and pathological scenarios [37].

In this chapter, we will review a selection of foundational models, highlighting the key features and functional insights each provides.

1.2.1 Neuron Models

Biophysically detailed models such as the Hodgkin-Huxley model, which will be nextly presented below, are computationally expensive and analytically challenging. While they provide an accurate representation of ionic mechanisms, it is often necessary to consider simpler and more computationally efficient models that still capture the essential features of neuronal behavior. In this regard, tools such as phase plane analysis and dimensionality reduction are powerful methods for extracting the core dynamics of neurons [37]. Notable examples of such approaches include the Morris-Lecar model [70] and the FitzHugh–Nagumo model [71].

In this section, we present two simplified canonical models [47]:

- The **Leaky Integrate-and-Fire (LIF)** model provides a classical and widely-used framework for describing neuronal dynamics. It was interestingly proposed in 1907, way before the understanding of the underlying mechanisms [1]. It models the membrane potential of a neuron as a leaky integrator of synaptic inputs, with a spike emitted when the potential crosses a fixed threshold. Its balance between biological plausibility and mathematical simplicity makes it an essential tool for large-scale network simulations and theoretical studies.
- The **Quadratic Integrate-and-Fire (QIF)** model extends the LIF framework by introducing a nonlinear voltage-dependent term—specifically, a quadratic component. This modification enables the model to reproduce the spike initiation dynamics near a saddle-node bifurcation, characteristic of type I neuronal excitability, as defined below. Due to its minimal mathematical form and rich dynamical behavior, the QIF model is considered the canonical normal form for type I excitable systems. It plays a central role in neural field models and mean-field reductions, particularly in the study of collective phenomena in spiking networks [69].

1.2.1.1 Types of Neuronal Excitability

A classification of neuronal excitability based on how neurons respond to input currents was first proposed by Hodgkin and Huxley in 1952 [46], and later formalized by Izhikevich in 2007 [47]. This framework categorizes neurons into three types of excitability: **Type I**, **Type II**, and **Type III**.

- **Type I** excitability is characterized by a continuous onset of firing as the input current increases. Neurons of this type can fire at arbitrarily low frequencies, with a smooth and continuous frequency-current (f–I) relationship starting from zero. This behavior is typically associated with a saddle-node bifurcation on an invariant circle since the period of the invariant circle diverges at the bifurcation.
- **Type II** excitability exhibits a discontinuous jump in firing frequency once the input surpasses a threshold. Neurons of this type begin spiking at a finite, nonzero frequency, and their dynamics are commonly linked to a sub-critical Hopf bifurcation. They are frequently associated with resonant or bursting behavior.
- **Type III** excitability refers to neurons that do not support sustained spiking in response to constant stimulation. Instead, they produce brief, transient responses to rapid changes or perturbations. These neurons often function as coincidence detectors or are specialized for fast, transient signal processing.

This classification provides a theoretical foundation for understanding the diversity of neuronal firing behaviors and has important implications for how different types of neurons encode and transmit information.

1.2.1.2 Conductance-Based Models: The Hodgkin–Huxley Formalism

The Hodgkin–Huxley model was the first prototype of what would later be more generally referred to as conductance-based models. At the level of the membrane, ionic currents follow the principles of electrical circuits, modulated by the biological mechanisms introduced earlier. The Hodgkin–Huxley model represents a first level of abstraction in which the cell membrane is treated as an electrical circuit. This formalism enables the use of differential equations to describe the system’s dynamics with precision.

It is called a conductance-based model because each ionic current is expressed as a function of its conductance and driving force. The original model proposed by Hodgkin and Huxley, only include sodium and potassium dynamics. However, a wide variety of ion channels exist across brain regions and neuronal types, each contributing distinct electrophysiological properties [26]. Hence this framework offers a flexible and extensible base for incorporating such biological diversity into more specialized or region-specific models.

For sodium and potassium dynamics only, the model reads:

$$\begin{aligned} I_c &= -I_{Na} + -I_K + -I_L, \\ C_m \frac{dV}{dt} &= -g_{Na}(V - V_{Na}) - g_K(V - V_K) - g_L(V - V_L). \end{aligned} \quad (1.1)$$

where:

- $I_c = C_m \frac{dV}{dt}$ is the capacitive current, based on Coulomb's law of capacitance;
- $I_X = g_X(V - V_X)$ is the current through ion channel $X \in \{Na, K, L\}$, following Ohm's law;
- C_m is the membrane capacitance;
- g_{Na}, g_K, g_L are the conductances for sodium, potassium, and leak channels, respectively;
- V_{Na}, V_K, V_L are the corresponding reversal (Nernst) potentials. These reflect the electrochemical equilibrium for each ion species. When the membrane potential equals the Nernst potential, the net current of that ion is zero. The overall membrane potential results from the weighted contribution of each ion's equilibrium potential.

The corresponding electrical circuit representation is illustrated Fig 1.3.

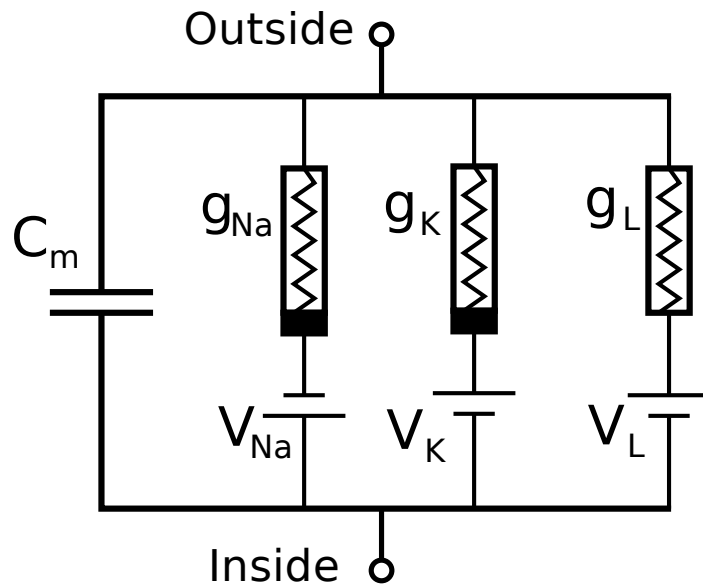


Figure 1.3: Electrical circuit representation of the neuronal membrane corresponding to Eq 1.1, as proposed by Hodgkin and Huxley (1952). Adapted from <https://commons.wikimedia.org/wiki/File:Hodgkin-Huxley.svg>

The expressions for the ion-specific conductances were derived empirically to reproduce observed neuronal responses:

$$g_{Na} = \overline{g_{Na}} m^3 h, \quad (1.2)$$

$$g_K = \overline{g_K} n^4, \quad (1.3)$$

$$g_L = \overline{g_L}. \quad (1.4)$$

where m , h , and n are gating variables governed by voltage-dependent kinetics of the form:

$$\frac{dX}{dt} = \alpha_X(V)(1 - X) - \beta_X(V)X, \quad X \in \{m, h, n\} \quad (1.5)$$

Although these equations are empirical, they remain closely tied to biological reality. For example, in equation (1.3), the exponent 4 applied to the gating variable n corresponds to the four subunits that must simultaneously open to allow potassium ions to pass through the channel.

1.2.1.3 Leaky Integrate-and-Fire (LIF) Model

We remind that an action potential is a rapid electrical impulses generated after a flow cascade, when voltage depend ion sodium opens at a threshold. It is the most elementary component of neural communication. The Leaky Integrate-and-Fire (LIF) model is one of the simplest and most widely used mathematical models for describing neuronal dynamics. Despite its simplicity, it effectively captures the fundamental aspects of neuronal spiking behavior and is widely employed in computational neuroscience. The LIF model describes the formation mechanism of action potential. It abstracts the biological components to its deterministic behavior, providing a mathematical representation of a neuron.

In this model, the neuron is treated as a current based neuron, as all channels are represented as an electric current, with a leaky term. The corresponding electrical circuit representation is illustrated Fig 1.4. We can express the total current I like:

$$\begin{aligned} I_C &= -I_L, \\ C_m \frac{dV}{dt} &= \tau(V - V_{\text{rest}}). \end{aligned} \quad (1.6)$$

with:

- $I_L = \tau(V - V_{\text{rest}})$, the leaky current. It is a linear simplification of all ionic current.
- $I_C = C_m \frac{dV}{dt}$, the membrane current where the membrane act like a capacitor with capacitance C_m .

The model works as follows:

1. The neuron integrates input currents over time, causing its membrane potential $V(t)$ to increase.
2. When the membrane potential reaches a predefined **threshold voltage** V_{th} , the neuron generates an **action potential (spike)**.
3. After spiking, the membrane potential is immediately reset to a lower value V_{reset} .

The threshold generating a spike imitates the opening of sodium channels and its transient ions entry. To reproduce the refractory period, other rules are usually used:

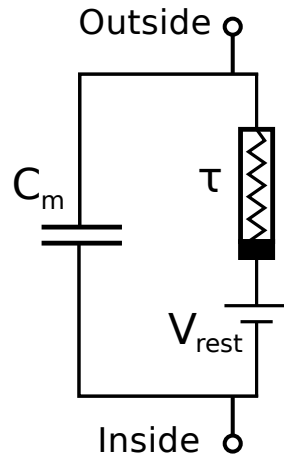


Figure 1.4: Electrical circuit representation of the LIF model, corresponding to Eq 1.6. Adapted from <https://commons.wikimedia.org/wiki/File:Hodgkin-Huxley.svg>

- After a spike, the voltage is locked for a fixed period and the neuron can not fire again [36], acting as the absolute closing of sodium channels.
- Instead of enforcing a complete block, refractoriness can be modeled as a temporary increase in the firing threshold, making spiking progressively more difficult but not impossible to trigger directly after a previous spike [73].
- An other approach consists in adding a transient inhibitory conductance $g_{ref}(t)$, often modeled as an exponentially decaying function of time after a spike. This conductance drives the membrane potential toward the potassium reversal potential, effectively reproducing the spike-triggered afterhyperpolarization observed experimentally [11].

The LIF model is widely used due to its balance between biological realism and computational efficiency as it accurately models the essential aspects of neuronal integration and spiking. It simplicity allow for easy complexification like the incorporation of Noise which transform the LIF model into an Ornstein-Ulenbeck process.

Besides its advantages, the LIF model does not account for detailed ion channel dynamics, making it less precise than biophysically detailed models like Hodgkin-Huxley. Also, formally, the LIF model should not be study with classical ordinary differential equation tools, because of the discontinuity triggered by a spike occurrence. The differential inclusion field of mathematics is instead devoted to this problematic. Still, it is effectively often used to model neuronal population dynamics and serves as the basis for many neural network simulator.

1.2.1.4 Quadratic Integrate-and-Fire (QIF)

The Quadratic Integrate-and-Fire (QIF) model is a canonical one-dimensional reduction of more complex conductance-based models, such as the Hodgkin-Huxley system. It naturally arises in the context of bifurcation theory, specifically as the

normal form of the saddle-node on invariant circle (SNIC) bifurcation, which describes the transition from rest to repetitive spiking in neurons exhibiting Type I excitability [29].

Mathematically, the QIF model is described by the differential equation:

$$\frac{dV}{dt} = \tau V^2 + I \quad (1.7)$$

where:

- τ is a time-scaling parameter,
- I represents the total input current.

As with the leaky integrate-and-fire (LIF) model, a reset mechanism is applied:

$$\text{if } V(t) \geq V_{\text{th}}, \text{ then } V \rightarrow V_{\text{reset}}, \text{ and a spike occurs.} \quad (1.8)$$

Unlike the LIF model, which features linear subthreshold integration, the QIF model includes a quadratic term that captures the sharp acceleration of membrane potential near spike threshold. This nonlinearity reflects the spike initiation dynamics seen in Type I neurons more accurately than linear models.

Despite its simplicity, the QIF model retains key nonlinear characteristics, making it both analytically tractable and biologically relevant. It has become a cornerstone in theoretical neuroscience, particularly in the modeling of population dynamics. Its structure permits exact mean-field reductions through phase-reduction techniques, enabling low-dimensional descriptions of large networks of spiking neurons [69]. These features position the QIF model as a powerful tool for linking single-neuron properties to emergent macroscopic neural behavior.

The solution to equation (1.7), for constant input $I > 0$, is given by:

$$V(t) = \frac{\sqrt{I}}{\sqrt{\tau}} \tan \left(\sqrt{I\tau} t + c_0 \right) \quad (1.9)$$

where:

- $c_0 = \arctan \left(\frac{\sqrt{\tau}}{\sqrt{I}} V_0 \right)$ is an integration constant determined by the initial condition $V(0) = V_0$.

Under constant positive input $I > 0$, the voltage trajectory diverges to $+\infty$ in finite time. From time t_0 , this occurs within:

$$t_{\text{spike}} = \frac{1}{\sqrt{\tau I}} \left(\frac{\pi}{2} - \arctan \left(\frac{\sqrt{\tau}}{\sqrt{I}} V(t_0) \right) \right) \quad (1.10)$$

This finite-time divergence is interpreted as the occurrence of a spike, necessitating a reset to V_{reset} to continue the simulation.

1.2.1.5 Theta Neuron

The θ -neuron is also a canonical model for Type I excitable neurons, offering a compact yet biophysically meaningful representation of spike generation near a saddle-node on invariant circle (SNIC) bifurcation [29]. The dynamics are described by a phase-like variable $\theta \in [-\pi, \pi]$, which evolves according to:

$$\frac{d\theta}{dt} = 1 - \cos \theta + (1 + \cos \theta)I, \quad (1.11)$$

where I denotes the external input current. When $I < 0$, the system has a stable fixed point corresponding to a quiescent resting state. For $I > 0$, the dynamics enter a limit cycle, corresponding to sustained periodic spiking. The point $\theta = \pi$ is conventionally interpreted as the spike emission phase.

A central feature of the θ -neuron model is its exact mathematical equivalence to the Quadratic Integrate-and-Fire (QIF) model. Via the nonlinear transformation $V = \tan\left(\frac{\theta}{2}\right)$, the QIF equation Eq (1.7) is mapped onto the θ -neuron equation Eq (1.11) [47]. This change of variables not only preserves the underlying bifurcation structure but also compactifies the unbounded voltage domain ($V \in \mathbb{R}$) into a bounded circular phase space ($\theta \in [-\pi, \pi]$), thereby eliminating the divergence at spike times and enabling continuous phase-based analysis.

As a result of this equivalence, the θ -neuron retains the excitability properties of the QIF model while offering a smooth and continuous representation of neuronal dynamics, including spike generation. The model's robustness and clarity have made it a widely used tool for simulating sparse and burst-like firing patterns—features often observed in circuits involved in rapid learning and synaptic plasticity, such as the dorsolateral striatum. Its analytical tractability also makes it a powerful tool for studying spike initiation, responses to noisy inputs, and synchronization phenomena in networks.

1.2.2 Neural Mass Models

Neural mass models aim to describe the collective dynamics of large populations of neurons by representing them as continuous variables—typically the average firing rate and/or the mean membrane potential. Rather than modeling individual spiking events, these models capture the macroscopic behavior of neuronal ensembles, making them particularly suited for linking neural activity to large-scale signals such as EEG or fMRI.

A fundamental assumption of neural mass modeling is that within a given population, neurons are sufficiently similar and densely connected so that their collective behavior can be approximated by smooth, deterministic equations. This simplification allows for tractable analysis of emergent behaviors such as oscillations, synchronization, and bistability, which are challenging to study in high-dimensional spiking networks.

One of the most influential neural mass models is the **Wilson–Cowan model**, which describes the temporal evolution of the mean firing rates of two interacting populations: one excitatory and one inhibitory. The model captures how the activity of each population evolves over time based on recurrent interactions and external input. Despite its simplicity, the Wilson–Cowan framework can generate a rich

repertoire of dynamical regimes including steady states, limit cycles, and excitability thresholds.

This modeling approach has been widely used to study cortical oscillations, perceptual bistability, working memory, and pathological dynamics such as epileptic seizures.

1.2.2.1 Population Model: Wilson–Cowan

The Wilson–Cowan model, introduced in the early 1970s by Hugh R. Wilson and Jack D. Cowan [109, 110], was one of the first formal attempts to describe the collective dynamics of interacting neural populations. Unlike conductance-based models such as Hodgkin–Huxley, which focus on the biophysics of individual neurons, the Wilson–Cowan framework operates at a mesoscopic scale. It models the mean firing rates of excitatory and inhibitory populations over time, abstracting away individual spiking activity in favor of continuous population-level variables.

The original motivation behind the model was to understand how local cortical circuits could give rise to emergent phenomena such as oscillations, multistability, and pattern formation. To do so, the model describes the evolution of the proportion of active neurons in each population using a pair of coupled nonlinear differential equations. As schematized Fig 1.5, it incorporates recurrent excitation and inhibition (w_{EE}, w_{II}), mutual excitation and inhibition (w_{IE}, w_{EI}), and saturating nonlinear activation functions (typically sigmoidal, Eq 1.14). It is thus enables to reproduce a rich variety of dynamical behaviors with relatively few assumptions.

Importantly, the Wilson–Cowan model does not attempt to reproduce spike waveforms or ion channel kinetics, but instead provides a powerful analytical framework for exploring how population-level excitation and inhibition interact to generate large-scale dynamics. It has thus played a foundational role in the development of neural mass and population models in computational neuroscience.

The model describes two interacting neural populations: an excitatory population E and an inhibitory population I , with dynamics governed by:

$$\tau_E \frac{dr_E}{dt} = -r_E + S_E(w_{EE}r_E - w_{EI}r_I + I_E^{\text{ext}}) \quad (1.12)$$

$$\tau_I \frac{dr_I}{dt} = -r_I + S_I(w_{IE}r_E - w_{II}r_I + I_I^{\text{ext}}) \quad (1.13)$$

where:

- r_E and r_I represent the mean firing rates of the excitatory and inhibitory populations,
- w_{XY} denotes the synaptic weight from population Y to population X , with $X, Y \in \{E, I\}$,
- I_E^{ext} and I_I^{ext} are external inputs to the respective populations,
- S_E and S_I are activation functions representing the nonlinear relationship between input and firing rate.

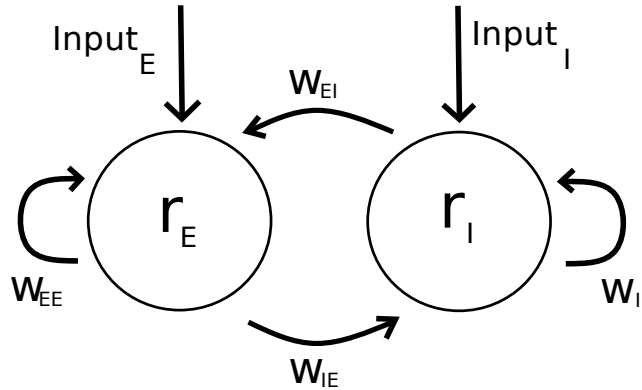


Figure 1.5: Schematic representation of the Wilson–Cowan model. w_{EE}, w_{II} are recurrent excitation and inhibition respectively. w_{IE}, w_{EI} are mutual excitation and inhibition respectively.

A typical form for the activation function $S(x)$ is:

$$S(x) = \alpha \left(\left(1 + e^{-\gamma(x-\theta)} \right)^{-1} - \left(1 + e^{\gamma\theta} \right)^{-1} \right), \quad (1.14)$$

where:

- α is the maximum firing rate,
- θ is the threshold (the inflection point of the sigmoid),
- γ is the gain, determining the slope near threshold,
- The subtraction term ensures that $S(0) = 0$, i.e., no firing in the absence of input.

Beyond its foundational role, the Wilson–Cowan model allows for rigorous mathematical analysis. Fixed points—corresponding to steady-state firing rates—are found by solving $\frac{dr_E}{dt} = \frac{dr_I}{dt} = 0$. Local stability is assessed by linearizing the system around these equilibria and examining the eigenvalues of the resulting Jacobian matrix.

Depending on the values of the synaptic weights and external inputs, the model can exhibit:

- monostability or multistability (coexistence of multiple stable states),
- oscillatory behavior via Hopf bifurcations,
- excitable transients and switching dynamics.

These dynamical regimes are not only mathematically rich but also biologically relevant. They have been used to model cortical rhythms, perceptual bistability, decision-making processes, and state transitions in sensorimotor systems.

1.2.3 Mean field model

Mathematics have been extensively applied within the field of neuroscience, aiming to uncover and understand the fundamental principles underlying neuronal dynamics and brain functions. Given the inherent complexity of biological neural networks

and the challenges associated with experimentally recording and interpreting large-scale neuronal interactions, mathematical models have become essential tools for describing and analyzing macroscopic brain activity.

Neural mass models, such as the Wilson–Cowan model, represent the dynamics of neuronal populations by directly linking the activity of excitatory and inhibitory groups through phenomenological equations. In contrast, **mean field models** aim to derive population-level dynamics from microscopic descriptions of individual neurons. This approach typically starts from simplified single-neuron models, like those presented in Section 1.2.1, and uses averaging techniques to extract macroscopic variables that capture the essential features of network behavior.

A classical example is the **Kuramoto model**, originally developed to study the synchronization of coupled oscillators and later extended to neuroscience. It can be derived from populations of phase oscillators such as θ -neurons (see Section 1.2.1.5) [29, 53]. By introducing a complex-valued **order parameter**, the Kuramoto model captures global synchronization dynamics in a concise manner. This parameter summarizes the coherence of the population’s phase distribution, providing key insights into transitions between asynchronous and synchronous regimes.

Another significant advancement in mean field modeling is demonstrated in the work by Montbrió, Pazó, and Roxin (2015), who developed the "Lorentzian ansatz" within a network of Quadratic Integrate-and-Fire (QIF) neurons. Starting from an individual QIF neuron description and considering the limit of an infinite network, they formulated the dynamics of the network using a probability density function. Under the assumption of a Lorentzian distribution of neuronal excitability (Lorentzian hypothesis), they successfully derived exact analytical equations describing the evolution of the mean firing rate and membrane potentials. This framework provides a powerful method for understanding the emergence of macroscopic behaviors - such as oscillations, synchronization, and bifurcation phenomena - from microscopic neuron-level dynamics. The Lorentzian ansatz will be discussed in detail in Section 1.3, as an extension of this approach constitutes the core of Chapter 3.

Conclusion

Since the inception of mean field theory in neuroscience, a wide variety of approaches have emerged from purely analytical frameworks to semi-numerical methods. Standardized formulations and classifications have been proposed in efforts to unify the field [81]. Yet, the foundations of mean field theory continue to be critically examined. A line of research focuses on quantifying finite-size effects, aiming to bridge the gap between idealized mean field descriptions in the infinite-size limit and the constraints imposed by real-world, finite neural networks [12].

Overall, neural mass and mean field models have significantly enriched our theoretical understanding of neural network behavior, paving the way of linking microscopic neuronal mechanisms with large-scale brain activity

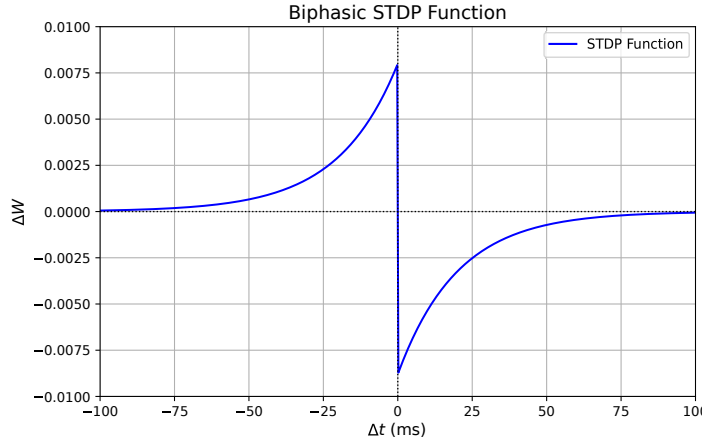


Figure 1.6: Biphasic response of plasticity, in respect to δt . δt denote the delay between pre- and post-synaptic spike. Negative delay happen when post-synaptic spike occurs before pre-synaptic one.

1.2.4 STDP model

1.2.4.1 Biphasic Spike-Timing-Dependent Plasticity (STDP)

One of the most well-known models of synaptic plasticity is **Spike-Timing-Dependent Plasticity (STDP)**, which adjusts synaptic strength based on the precise relative timing of pre- and post-synaptic action potentials. First observed by G. Bi and M. Poo (1998) [8], the **biphasic** nature of STDP refers to the fact that synaptic weights can either be **potentiated** (strengthened) or **depressed** (weakened) depending on the timing interval between spikes.

Song et. al (2000) [98], proposed a mathematical expression for the biphasic STDP. The synaptic weight change ΔW is modeled using an exponential function of the time difference $\Delta t = t_{\text{post}} - t_{\text{pre}}$, where t_{pre} and t_{post} denote the firing times of the pre- and post-synaptic neurons, respectively. Illustrated Fig 1.6, ΔW reads:

$$\Delta W = \begin{cases} A_+ e^{-\Delta t / \tau_+}, & \text{if } \Delta t > 0 \quad (\text{LTP}) \\ -A_- e^{\Delta t / \tau_-}, & \text{if } \Delta t < 0 \quad (\text{LTD}) \end{cases} \quad (1.15)$$

where:

- ΔW is the change in synaptic weight,
- A_+ and A_- are amplitude factors for potentiation and depression respectively,
- τ_+ and τ_- are time constants that control the temporal sensitivity of LTP and LTD.

In this model:

- If a **pre-synaptic spike precedes** a post-synaptic spike ($\Delta t > 0$), **long-term potentiation (LTP)** is induced, strengthening the synapse.
- If a **pre-synaptic spike follows** a post-synaptic spike ($\Delta t < 0$), **long-term depression (LTD)** occurs, weakening the synapse.

This learning rule is consistent with Hebbian plasticity, often paraphrased as "*neurons that fire together wire together*". Importantly, the presence of LTD introduces a competitive mechanism between synapses, which prevents unbounded potentiation and maintains synaptic balance.

The biphasic STDP model has been experimentally validated in several brain areas, including the hippocampus and neocortex. However, while this phenomenological model successfully reproduces the observed timing dependence of plasticity, it does not fully account for the underlying biological mechanisms. Consequently, numerous studies have since aimed to derive STDP from more biophysically grounded models, incorporating intracellular signaling cascades, dendritic integration, and neuromodulatory influences.

1.2.4.2 Graupner Brunel STDP

Understanding the mechanisms by which synaptic strength is modified in response to neural activity is central to computational neuroscience. A major advance in this domain was made by Graupner and Brunel (2012) [41], who proposed a unifying calcium-based model of synaptic plasticity. Their work aims to explain the diversity and complexity of experimentally observed long-term potentiation (LTP) and long-term depression (LTD) outcomes across different brain regions and stimulation protocols.

The core hypothesis of their model is that the post-synaptic calcium concentration serves as a key signal for the induction of plasticity. Rather than modeling detailed biochemical pathways, the authors adopt a simplified description of calcium dynamics and implement threshold-based rules to determine the direction of synaptic change:

- **Potentiation** occurs when calcium concentration exceeds an upper threshold θ_{pot} .
- **Depression** is induced when calcium remains above a lower threshold θ_{dep} but below θ_{pot} .

The evolution of synaptic efficacy $p(t) \in [0, 1]$ is governed by the following differential equation:

$$\tau \frac{dp}{dt} = -p(1-p)(p_* - p) + \gamma_p(1-p)\Theta(c(t) - \theta_p) - \gamma_d p\Theta(c(t) - \theta_d) + N(t) \quad (1.16)$$

where:

- p is the synaptic weight,
- $c(t)$ is the post-synaptic calcium concentration at time t
- p_* is an unstable fixed point; in the absence of calcium input, p converges to 1 if $p > p_*$ and to 0 if $p < p_*$
- θ_p and θ_d are the potentiation and depression thresholds, respectively,
- γ_p and γ_d are the rates of potentiation and depression,
- $\Theta(\cdot)$ denotes the Heaviside step function,

- $N(t)$ represents noise or variability in synaptic transmission.

This elegant and compact formulation replicates a wide variety of spike-timing dependent plasticity (STDP) curves observed experimentally in both hippocampal and neocortical synapses. It also accounts for the influence of spike frequency, temporal patterns, and dendritic location on synaptic outcomes—providing a unified framework for interpreting diverse forms of long-term plasticity.

By directly linking calcium transients to synaptic modification rules, the model bridges the gap between biophysical mechanisms and phenomenological plasticity rules. It stands out for its ability to make quantitative predictions, its analytical tractability, and its scalability for implementation in large-scale network simulations, making it a valuable tool for modeling learning and memory processes.

Conclusion

This chapter presented an overview of the biological foundations of neural computation, along with some computational models used to describe neuronal dynamics and synaptic plasticity. From detailed conductance-based models to reduced spiking neuron models and population-level formalisms, we have outlined the essential tools that link microscopic mechanisms to macroscopic brain activity.

We also reviewed key theories of synaptic plasticity, including phenomenological models such as STDP, as well as more biophysically grounded frameworks like the calcium-based model of Graupner and Brunel. Together, these models provide a mechanistic understanding of how neural systems can adapt and learn from experience.

In the following Section 1.3 and Section 1.4, we provide detailed reviews of two complementary modeling approaches: a macroscopic mean-field framework based on QIF neurons, and a microscopic mechanistic model of cortico-striatal synapses. These reviews will serve as foundations for Chapter 2 and Chapter 3, which present the two main lines of research developed in this thesis.

1.3 Montbrió–Pazó–Roxin (2015) and the Lorentzian Ansatz

In this work, we examine the framework introduced by Montbrió, Pazó, and Roxin [69], interpreted through the Lorentzian ansatz. Their approach departs from classical neural-mass models by building directly upon a detailed, single-neuron description. Specifically, each neuron is modeled as a Quadratic Integrate-and-Fire (QIF) unit.

Network formulation

The membrane potentials of a QIF population of N neurons, $(V_j)_{j \in \llbracket 1, N \rrbracket}$, obey

$$\frac{dV_j}{dt} = V_j^2 + I_j(t), \quad (1.17)$$

when $V_j > V_t$, $V_j \leftarrow V_r$ and a spike is produced.

Here I_j is the input current to neuron j , V_t the spiking threshold, and V_r the reset potential. In the “infinite-threshold” limit $V_t = -V_r \rightarrow +\infty$, this choice effectively encodes a refractory period. As noted in Section 1.2.1.4, if $\max(I_j(t)) = I_{max} > 0$, then from time t_0 , V_j diverges (i.e. emits a spike) in less than

$$\frac{1}{\sqrt{I_{max}}} \left(\frac{\pi}{2} - \arctan \frac{V(t_0)}{\sqrt{I_{max}}} \right). \quad (1.18)$$

The input current decomposes as

$$I_j = I(t) + \eta_j + J s(t), \quad (1.19)$$

where $I(t)$ is a common, time-varying external drive, η_j a static heterogeneity in excitability, and $J s(t)$ the recurrent contribution with

$$s(t) = \frac{1}{N} \sum_{j=1}^N \sum_{k | t_j^k < t} \int_{-\infty}^t a_\tau(t-t') \delta(t'-t_j^k) dt',$$

where t_j^k is the k th spike time of neuron j , δ the Dirac delta, and $a_\tau(t) = e^{-t/\tau}/\tau$ the residual EPSP signal.

Ininitely fast synapses

As $\tau \rightarrow 0$, $a_\tau(t)$ converges pointwise to a delta function. Hence for an infinitely fast synapse:

$$s(t) = \frac{1}{N} \sum_{j,k | t_j^k < t} \int_{-\infty}^t \delta(t-t') \delta(t'-t_j^k) dt' = \frac{1}{N} \sum_{j,k | t_j^k < t} \delta(t-t_j^k),$$

which counts the fraction of neurons spiking at time t . Denoting this mean firing rate by $r(t)$, the input becomes

$$I_j = I(t) + \eta_j + J r(t).$$

Continuum limit

In the limit $N \rightarrow \infty$, the infinite network’s states are represented by a distribution $\rho(V, \eta, t)$ so that $\rho(V|\eta, t) dV$ is the probability to find a neuron with voltage in $[V, V+dV]$ conditional on excitability η , which is distributed according to $g(\eta)$. Conservation of neurons implies the continuity equation

$$\frac{\partial \rho}{\partial t} + \frac{\partial}{\partial V} [(V^2 + \eta + Jr + I) \rho] = 0. \quad (1.20)$$

Stationary (trivial) solution

Setting $I = 0$ and $\partial_t \rho = 0$, eq (1.20) yields

$$\rho_0(V|t, \eta) = \frac{c_0}{V^2 + \eta + Jr}, \quad (1.21)$$

$$c_0 = \frac{\sqrt{\eta + Jr}}{\pi}.$$

which is a Lorentzian (Cauchy) distribution of half-width $x_0 = \sqrt{\eta + Jr}$ and center $y_0 = 0$ (See Sec 3.8 for intermediate steps). Montbrió et al. conjecture and provide both conformal-mapping arguments and numerical evidence that arbitrary solutions relax to a Lorentzian distribution. From now we will assume the following form for ρ :

$$\rho(V|t, \eta) = \frac{1}{\pi} \frac{x(t, \eta)}{(V - y(t, \eta))^2 + x^2(t, \eta)}. \quad (1.22)$$

Firing rate and mean voltage

The conditional firing rate is the probability flux at $V \rightarrow +\infty$:

$$r(t, \eta) = \lim_{V \rightarrow \infty} \rho(V|\eta, t) \frac{dV}{dt} = \frac{x(t, \eta)}{\pi}, \quad (1.23)$$

so that the population-averaged rate is

$$r(t) = \frac{1}{\pi} \int x(t, \eta) g(\eta) d\eta. \quad (1.24)$$

Likewise, the mean membrane potential (in the Cauchy principal-value sense) evaluates to

$$v(t, \eta) = y(t, \eta), \quad (1.25)$$

so that r and v completely characterize the network state.

See Sec 3.8 for intermediate steps of Eq 1.23, Sec 3.8 for Eq 1.25.

Reduced ODE system

Expressing

$$w(t, \eta) = x(t, \eta) + iy(t, \eta), \quad (1.26)$$

the continuity equation yields

$$\frac{dw}{dt}(t, \eta) = i[\eta + Jr - w^2(t, \eta) + I(t)]. \quad (1.27)$$

Together with the integral expression for $r(t)$ Eq 1.24, this is an integro-differential system.

Lorentzian heterogeneity and final reduction

Assuming now that $g(\eta)$ itself is Lorentzian with center $\bar{\eta}$ and half-width Δ , the residue theorem gives

$$\int f(\eta) g(\eta) d\eta = f(\bar{\eta} - i\Delta) \quad (1.28)$$

for suitable f . See Sec 3.8 for intermediate steps of Eq 1.28.

Hence, integrating Eq 1.26 against $g(\eta)$:

$$\pi r(t) + i v(t) = w(t, \bar{\eta} - i\Delta),$$

and plugging into the w -dynamics yields the two-dimensional Montbrió–Pazó–Roxin equations:

$$\begin{cases} \dot{r} = \frac{\Delta}{\pi} + 2 r v, \\ \dot{v} = v^2 - \pi^2 r^2 + J r + \bar{\eta} + I(t). \end{cases} \quad (1.29)$$

See Sec 3.8 for intermediate steps of Sys 1.29. This reduction provides a powerful bridge between single-neuron dynamics and macroscopic brain activity, with the Lorentzian ansatz rendering the system eminently tractable.

1.4 eCB Fast learning

1.4.1 The mystery of fast learning

Identifying the neural substrate, or engram, underlying fast learning—defined as the capacity to form lasting memories after minimal exposure to relevant stimuli—remains a significant challenge in neuroscience. Although fast learning is critical for adaptive behavior in dynamic environments, its mechanistic bases are not yet fully understood. The dorsolateral striatum (DLS), notably involved in procedural learning and habit formation, has been proposed as a potential region implicated in fast learning [42]. Specifically, corticostriatal synapses have been shown to exhibit distinct plasticity profiles depending on the training phases. Procedural learning from repetitive trials typically involves NMDA receptor-dependent long-term potentiation (NMDAR-LTP), whereas early-trial plasticity is predominantly NMDAR-independent [7, 116]. Importantly, fast learning is inherently characterized by sparse firing and few bursts of neuronal activity, which are nonetheless sufficient to induce durable synaptic modifications and persistent network activity alterations [84]. In line with these observations, recent studies [19, 21] highlighted a crucial role of the endocannabinoid (eCB) signaling pathway at corticostriatal synapses, capable of mediating long-term potentiation (LTP) triggered by sparse stimulation protocols (5–15 pairings). This form of eCB-dependent plasticity, involving cannabinoid type-1 receptors (CB1R), emerges as a strong candidate mechanism for the engram underlying fast learning. Therefore, we will first review a computational model by Graupner and Brunel that delineates the bistable CaMKII-dependent plasticity, providing a foundational theoretical framework for synaptic stability, before addressing experimental evidence from Cui et al. (2016) demonstrating the nuanced role of eCB signaling in corticostriatal synaptic plasticity.

1.4.2 Graupner–Brunel CaMKII Model

There is accumulating evidence that synaptic plasticity can exhibit all-or-none dynamics, contrasting with the continuous and incremental changes posited by classical plasticity models. Minimal stimulation experiments at hippocampal CA3–CA1 synapses revealed abrupt, step-like changes in synaptic efficacy following minimal activity, as shown by Petersen et al. and O’Connor et al. [74, 80].

To account for such observations, Graupner and Brunel developed a mechanistic model of the Ca^{2+} /calmodulin-dependent protein kinase II (CaMKII) signaling pathway. This pathway has been identified as having a structural role for induction and maintenance of long-term potentiation (LTP) at the synapse [59].

CaMKII is structured as a complex, with subunits arranged in a circular geometry. Upon binding with calmodulin, individual subunits become susceptible to phosphorylation. Phosphorylation of CaMKII alters glutamatergic receptor function at the post-synaptic membrane and, crucially, enables auto-phosphorylation of neighboring subunits; a positive feedback mechanism that allows persistent kinase activity even after the initial calcium signal has decayed (see Fig 1.7 a-e).

Dephosphorylation of CaMKII is mediated by phosphatases such as protein phosphatase 1 (PP1) and indirectly calcineurin (PP2B), both of which are modulated through calcium-dependent pathways. PP1 activity is inhibited by the phosphorylated form of inhibitor-1 (I₁), which is phosphorylated by protein kinase A (PKA) and dephosphorylated by calcineurin. The protein cascade regulating CamKII activity is summarized Fig 1.7.f .

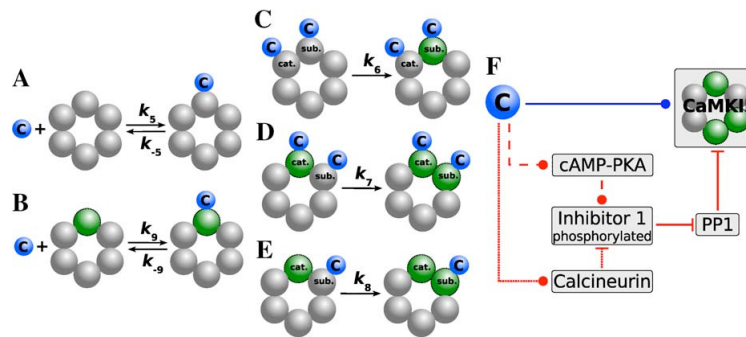


Figure 1.7: (A-E) Schematic representation of calmodulin (blue dots marked with a "c") binding to a CaMKII, for different intersubunits phosphorylation configurations. Grey are dephosphorylated subunits and green phosphorylated ones. (F) Protein Signaling Cascade. From Graupner & Brunel, 2007 [40].

This signaling cascade is captured in the model through the following reversible reactions:



where

- I_G and I denote dephosphorylated and phosphorylated inhibitor-1, respectively,
- D and D_I refer to free and inhibited PP1.

The phosphorylation and dephosphorylation rates are calcium-dependent and modeled using a Hill-type function plus constant:

$$\nu_X(C) = k_X^0 + \frac{k_X}{1 + \left(\frac{K_X}{C}\right)^n}, \quad X \in \{\text{CaN, PKA}\} \quad (1.32)$$

with

- k_X^0 a calcium/calmodulin - independant base activity
- k_X, K_X, n_X the Hill's function parameters corresponding respectively to the maximal activity, the half activity concentration and the Hill coefficient.

where k_X^0 is a calcium-independent basal activity, and k_X, K_X, n_X are Hill function parameters.

The dynamics of the concentrations of phosphorylated I1 and free PP1 are described by the differential equations:

$$\frac{dI}{dt} = -k_{13}ID + k_{-13}(D - D_0) - v_{\text{CaN}}(C)I + v_{\text{PKA}}(C)I_0 \quad (1.33)$$

$$\frac{dD}{dt} = -k_{13}ID + k_{-13}(D - D_0) \quad (1.34)$$

where $D_0 = D + D_I$ and $I_0 = I + I_G$ denote the total concentration of I1 and PP1.

To complete the model, Graupner and Brunel implemented a single-compartment Hodgkin-Huxley model of the post-synaptic membrane, omitting backpropagating action potentials:

$$C_m \frac{dV}{dt} = -I_L - I_{\text{Na}} - I_K - I_{\text{NMDA}} - I_{\text{CaL}} - I_{\text{AMPA}} + I_{\text{stim}} \quad (1.35)$$

with

- C_m the whole cell capacitance
- $I_X, (X \in \{\text{L, Na, K, NMDA, CaL, AMPA}\})$ the different ionic currents.
- I_{stim}

where C_m is the membrane capacitance and I_X represents the ionic currents: leak, sodium, potassium, NMDA, calcium (L-type), and AMPA-mediated. I_{stim} denotes an externally applied stimulation current.

The calcium dynamics model includes NMDA receptor-mediated and voltage-dependent calcium channel (VDCC) contributions:

$$\tau_{\text{Ca}} \frac{dC_a}{dt} = -(C_a - C_{a0}) + \tau_{\text{Ca}} \xi (\beta_{\text{NMDA}} I_{\text{NMDA}} + \beta_{\text{CaL}} I_{\text{CaL}}) \quad (1.36)$$

where

- C_a the free intracellular calcium concentration.
- τ_{C_a} is the time constance of exponential decay
- C_{a0} is the calcium resting concentration
- ξ, β_{NMDA} and β_{CaL} are unit conversion and scaling parameters.

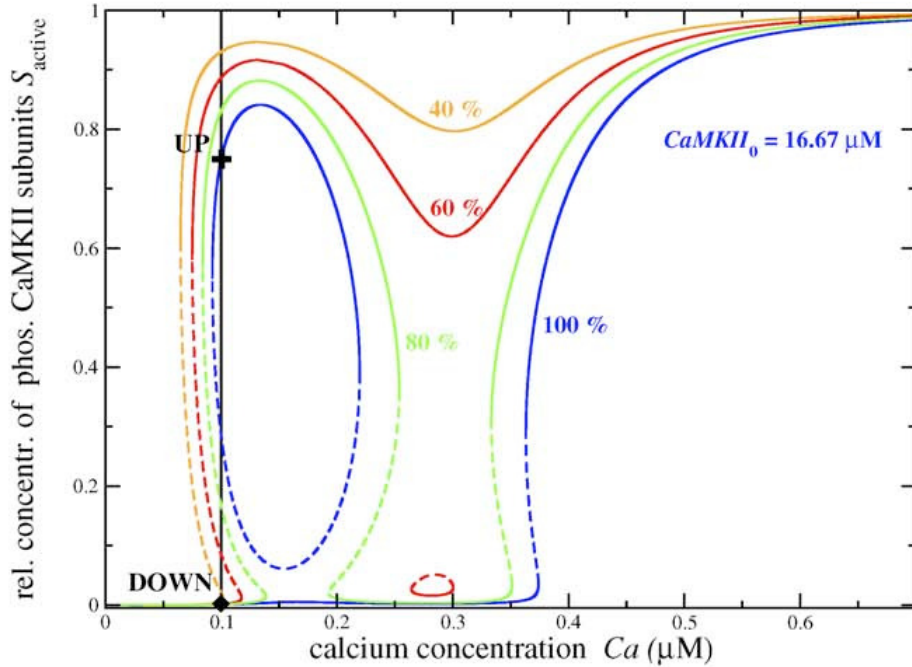


Figure 1.8: Bifurcation diagram of total phosphorylated CamK2 for different fixed levels of PP1. Calcium concentration is the bifurcation parameter. Full lines are stable steady states. Dashed lines are unstable steady states. Figure from Graupner & Brunel, 2007 [40].

where τ_{Ca} is the calcium decay time constant, Ca_0 is the resting calcium concentration, and ξ , β_{NMDA} , β_{CaL} are scaling and conversion factors.

The ionic conductance parameters were adopted from Poirazi et al. for calcium channels [85], and Purvis and Butera for sodium and potassium currents [86]. AMPA and NMDA receptor kinetics were drawn from prior studies [26, 48, 51]. Multiple parameters were fit on empirical data, like the ratio between calcium transients evoked by backpropagating action potentials and those driven by NMDA receptors was fixed at 2 [89]; or NMDA and CaL maximum conductance [61, 89].

Finally, the model captures a calcium-dependent bistability in the steady-state phosphorylation level of CaMKII. This dynamic is illustrated in the bifurcation diagram of Fig. 1.8, where calcium concentration is used as the bifurcation parameter for different fixed levels of PP1. The authors define the higher steady-state branch as the **UP state** and the lower one as the **DOWN state**. A transition from DOWN to UP can be interpreted as the induction of LTP, whereas a transition from UP to DOWN corresponds to LTD.

In the absence of PP1, the dynamics remain relatively simple: a stable DOWN plateau at very low calcium concentrations ($< 10 \mu\text{M}$), followed by a brief bistable region around $10 \mu\text{M}$, and then an UP plateau at higher calcium concentrations. The emergence and extent of bistability, however, are highly sensitive to the parameters controlling the PKA pathway (k_{PKA}^0 , k_{PKA} , K_{PKA} , n_{PKA}), which in turn modulate PP1 activity. At a critical threshold, PP1 can introduce a second DOWN window at intermediate calcium concentrations, thereby broadening the possible total CaMKII phosphorylation dynamics.

1.4.3 The diversity of synaptic plasticity

The computational model introduced by Graupner and Brunel provides a robust theoretical framework for understanding synaptic bistability mediated by CaMKII autophosphorylation dynamics, offering a mechanistic basis for long-term potentiation (LTP) and long-term depression (LTD) stability at synapses. However, experimental evidence suggests that synaptic plasticity in biological neural networks can involve additional neuromodulatory mechanisms beyond CaMKII signaling alone. In particular, Cui et al. (2015, 2016) [19, 21] demonstrated that endocannabinoid (eCB)-mediated signaling constitutes a critical regulatory mechanism capable of gating spike-timing-dependent plasticity (STDP) at corticostriatal synapses. Their work revealed a dual and dynamic role for the eCB pathway in modulating synaptic efficacy.

Conducting patch-clamp recordings in rodent brain slices, Cui and colleagues investigated synaptic changes at corticostriatal connections—specifically between layer 5 neurons of the somatosensory cortex and neurons in the dorsal striatum undergoing controlled stimulation protocols. In these experiments, synaptic stimulation was applied at a low frequency (1 Hz), and paired pre- and post-synaptic activation was required to induce plasticity. The relative spike timing (Δt) between pre- and post-synaptic spikes, varying from 0 to 30 ms, was identified as a critical determinant of the direction and magnitude of plasticity.

In pre–post pairing protocols, potentiation (tLTP) gradually increased with repeated stimulation, reaching a plateau around 50 pairings. In contrast, post–pre pairing protocols produced a biphasic effect: tLTP occurred with only a few pairings (5–10), disappeared with more repetitions (25–50), and then re-emerged when the number of pairings exceeded 50. This phenomenon illustrates a complex bidirectional form of STDP, wherein a 100-pairing protocol could lead to either spike-timing-dependent potentiation (tLTP) or depression (tLTD) depending on the pairing order and number of repetitions.

This form of tLTP induced by few pairings, was specifically dependent on the endocannabinoid (eCB) signaling pathway. This eCB-dependent tLTP (eCB-tLTP) necessitated post-synaptic synthesis of endocannabinoids, paired pre- and post-synaptic neuronal activity, and the activation of pre-synaptic cannabinoid type-1 receptors (CB1R) as well as post-synaptic transient receptor potential vanilloid type-1 (TRPV1) channels. Remarkably, this eCB bidirectionally can be induced sequentially in the same neuron independently of the order of induction protocols, highlighting the flexibility and reversibility of the underlying mechanisms.

This finding represented a significant breakthrough, as endocannabinoid signaling had been classically associated with synaptic depression, particularly through CB1R-mediated LTD. This form of LTD has been well established in several brain areas, including the cortex, striatum, and hippocampus [14–16]. The demonstration that eCBs can also support tLTP significantly broadens their functional role in synaptic plasticity and learning.

To support and extend their experimental findings, Cui et al. (2016) developed a computational model specifically tailored to cortico-striatal synapses. This model builds upon the calcium-based framework introduced by Graupner and Brunel, which originally accounted for NMDA receptor activity and CaMKII-mediated synaptic plasticity (presented in Sec 1.4.2).

The major innovation introduced by Cui and colleagues into the model, was the integration of the eCB signaling pathway and a **calcium induced calcium released** process. This addition enabled a more comprehensive mechanistic interpretation of synaptic changes observed experimentally. In particular, the model explicitly incorporated the dynamics of transient receptor potential vanilloid type-1 (TRPV1) channels—identified as a key downstream component in eCB-dependent tLTP. The implementation of TRPV1 dynamics followed the biophysical formulation proposed by Matta and Ahern (2007) [66].

The resulting computational framework effectively replicated various experimental protocols obtained from brain slice patch-clamp recordings by Venance Team at College de France, capturing critical characteristics of spike-timing-dependent plasticity (STDP).

Overview of the model

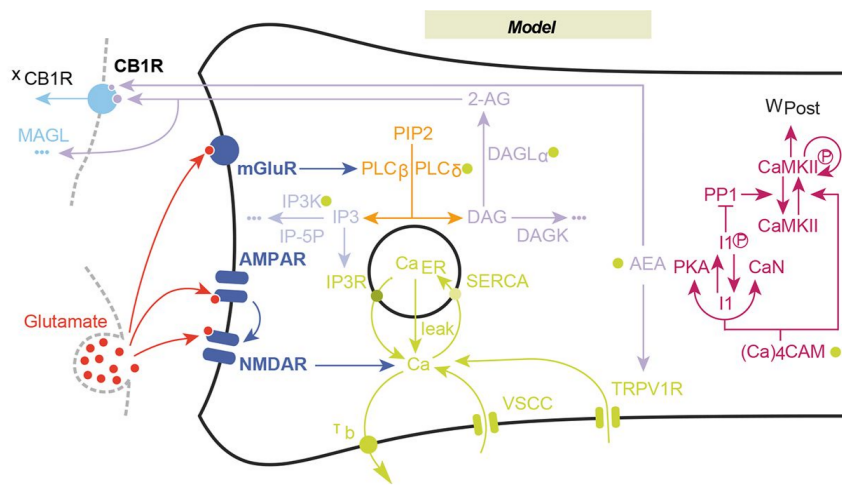


Figure 1.9: Schematic overview of the full biological model proposed by Cui et al. 2016 [21]. Color code: glutamate receptors: dark blue; PLC pathway: yellow; IP₃ pathway: powderblue; calcium pathways: green (green disks indicate calcium-dependent steps); DAGL α pathway: lavender; AEA pathway: light blue; CB1R pathway: blue. Figure from Cui et al. 2016, [21]

Figure 1.9 provides a comprehensive overview of the signaling network modeled by Cui et al. (2016) to capture the dynamics of endocannabinoid-dependent synaptic plasticity at cortico-striatal synapses. The synaptic weight W_{total} is expressed as the product of pre-synaptic and post-synaptic components, W_{pre} and W_{post} , respectively, allowing for independent but interacting modulation by distinct biochemical cascades.

The post-synaptic component W_{post} is regulated via NMDA receptor-mediated calcium influx and subsequent phosphorylation of CaMKII. This pathway embodies the classical NMDAR-dependent mechanism of LTP induction as described by Graupner & Brunel, (2007) (see Sec 1.4.2). In parallel, a second pathway—centered on endocannabinoid signaling—is activated by coincident stimulation of post-synaptic mGluRs and calcium entry through voltage-sensitive calcium channels (VSCCs) and TRPV1 channels. This leads to the synthesis of endocannabinoids 2- arachidonoyl-glycerol (2-AG) and anandamide (AEA), which serve as retrograde messengers.

The eCBs act on pre-synaptic CB1 receptors, modulating the synaptic output via w_{pre} . The inclusion of CB1R desensitization kinetics (represented by x_{CB1R}) is critical to reproduce experimentally observed timing- and repetition-dependent bidirectional plasticity.

Color-coded signaling pathways facilitate a clear distinction between glutamatergic, endocannabinoid, calcium-dependent, and intracellular signaling modules. The integration of these mechanisms into a unified model underscores the necessity of multi-pathway coordination to explain the full range of STDP observed experimentally in the corticostriatal system.

We now proceed to detail the mathematical formulation of the model, providing the explicit equations that describe its main features.

Synaptic Weight

To model the relationship between endocannabinoid (eCB) signaling and pre-synaptic plasticity, Cui et al. (2016) adopted a phenomenological approach, acknowledging the lack of detailed mechanistic models describing this pathway in the pre-synaptic compartment. Instead of relying on intracellular calcium concentration as the primary driver of plasticity, as in the classical framework proposed by Shouval et al. (2002) [94], they proposed that synaptic changes at the pre-synaptic terminal are governed by the level of CB1 receptor (CB1R) activation.

pre-synaptic plasticity is captured through the evolution of the pre-synaptic weight, w_{pre} , modulated by a plasticity direction function Ω , which depends on the total CB1R activation x_{CB1R} :

$$\Omega(x_{\text{CB1R}}) = \begin{cases} 1 - A_{\text{LTD}} & \text{if } x_{\text{CB1R}} \in [\theta_{\text{LTD}}^{\text{stop}}, \theta_{\text{LTP}}^{\text{start}}], \\ 1 + A_{\text{LTP}} & \text{if } x_{\text{CB1R}} > \theta_{\text{LTD}}^{\text{start}}, \\ 1 & \text{otherwise.} \end{cases} \quad (1.37)$$

Where total the CB1R activation is directly determined by 2-AG and AEA, weighted by α_{AEA} :

$$x_{\text{CB1R}} = 2\text{-AG} + \alpha_{\text{AEA}} \cdot AEA$$

Here, A_{LTP} and A_{LTD} set the target value (and effective rate) for synaptic potentiation or depression, while the threshold parameters $\theta_{\text{LTD}}^{\text{stop}}$ and $\theta_{\text{LTP}}^{\text{start}}$ determine the critical values of CB1R activation required to induce plasticity.

The dynamics of w_{pre} are governed by the difference between the current synaptic state and the plasticity target set by $\Omega(x_{\text{CB1R}})$, scaled by a plasticity time constant $\tau_{w_{\text{pre}}}$ that depends on the concentration of retrograde messengers:

$$\frac{dw_{\text{pre}}}{dt} = \frac{\Omega(x_{\text{CB1R}}) - w_{\text{pre}}}{\tau_{w_{\text{pre}}} (k_{\text{CB1R}} x_{\text{CB1R}} + D_2)}, \quad (1.38)$$

with the time constant defined as:

$$\tau_{w_{\text{pre}}}(x) = \frac{P_1}{(10^4 P_1)^{P_3} + (x_{\text{CB1R}})^{P_3}} + P_4. \quad (1.39)$$

This formulation ensures that high levels of the 2-AG and AEA accelerate plasticity induction, while very low concentrations lead to extremely slow changes, effectively introducing a memory-like behavior in synaptic dynamics. The parameter

P_1 , P_3 , and P_4 are tunable constants selected to match the desired plasticity kinetics. D_2 is an additive constant accounting for other sources of modulation affecting pre-synaptic plasticity.

Regarding the post-synaptic component of the synaptic weight (w_{post}), which is regulated by NMDAR-mediated signaling, the authors followed the modeling approach developed by Graupner and Brunel (2007) [40]. In this framework, w_{post} is directly linked to the cumulative activation of CaMKII.

post-synaptic Membrane Dynamics

The post-synaptic membrane is modeled using a conductance-based formalism, similar to the Hodgkin-Huxley framework [25]. The membrane potential V evolves according to capacitive and ionic currents, including a leak current, ligand-gated receptor currents, voltage-sensitive calcium channels, and back-propagating action potentials (bAPs). The membrane equation is given by:

$$C_m \frac{dV}{dt} = -g_L(V - V_L) - I_{\text{AMPA}}(V) - I_{\text{NMDA}}(V, G(t)) - I_{\text{VS}CC} - I_{\text{TRPV}1}(V, AEA) - I_{\text{act}}(t), \quad (1.40)$$

where C_m is the membrane capacitance, g_L is the leak conductance, and V_L is the leak reversal potential.

The synaptic and channel currents are defined as follows:

- $I_{\text{AMPA}}(V) = g_{\text{AMPA}} \cdot x_{\text{AMPA}} \cdot V$
- $I_{\text{NMDA}}(V) = \beta(V) \cdot g_{\text{NMDA}} \cdot x_{\text{NMDA}} \cdot V$
- $\beta(V) = \left(1 + \frac{[Mg^{2+}]}{\alpha_{\text{Mg}}} e^{-\tau_{\text{Mg}} V}\right)^{-1}$, a voltage-dependent magnesium block term [25]

post-synaptic Spike Currents The contribution of voltage-dependent calcium channels (VS CC) and bAP-induced depolarization follows the formulation of [112]:

$$I_{\text{VS}CC} = \Theta_{\text{act}}(t) \cdot DP_{\text{max}} + \text{bAP}(t) \quad (1.41)$$

- $\Theta_{\text{act}}(t)$ A square-like depolarizing current, multiplied by its amplitude DP_{max} , added symmetrically around the spike time and lasting for a duration DP_{dur} .
- $\text{bAP}(t)$ represents a residual depolarizing current, set to AP_{max} immediately following a spike, and decaying exponentially with a time constant τ_{bAP} .

These components collectively simulate the stereotypical depolarization waveform caused by an action potential reaching the dendritic spine, and are crucial for activating voltage-sensitive calcium channels and endocannabinoid synthesis. The TRPV1 current was modeled based on [66].

- $I_{\text{TRPV}1} = g_{\text{TRPV}1} \cdot P_{\text{open}}^{\text{TRPV}1}$, where $g_{\text{TRPV}1}$ is the maximal conductance and $P_{\text{open}}^{\text{TRPV}1}$ is the open probability of TRPV1 channels, modulated by AEA and temperature.

Note that Cui et al. (2016) reported difficulty in replicating the experimentally observed requirement for TRPV1 activation in eCB-mediated tLTP.

Calcium Dynamics. The intracellular calcium concentration Ca evolves under the influence of multiple calcium sources: NMDA receptors, VS_CC, TRPV1 channels, and internal stores via calcium-induced calcium release (CICR). The calcium dynamics follow:

$$J_{IP_3R} - J_{SERCA} + J_{leak} - \frac{Ca - Ca_b}{\tau_{Ca_b}} - \zeta_{NMDA} I_{NMDA} - \zeta_{VS_CC} I_{VS_CC} - \zeta_{TRPV1} I_{TRPV1}. \quad (1.42)$$

where:

- ζ_X , for $X \in \{\text{NMDA}, \text{VS_CC}, \text{TRPV1}\}$, are scaling factors converting ionic currents into calcium flux.
- J_{IP_3R} , J_{SERCA} , and J_{leak} represent fluxes resulting from CICR, modeled as in Pitta et al., 2009 [23].
- Ca_b is the basal cytosolic calcium level; in the absence of influx, Ca decays toward Ca_b with time constant τ_{Ca_b} .

The dynamics of calcium within the endoplasmic reticulum (ER), Ca_{ER} , are given by:

$$T_{Ca_{ER}}(Ca_{ER}) \cdot \frac{dCa_{ER}}{dt} = -\rho_{Ca_{ER}} \cdot (J_{IP_3R} - J_{SERCA} + J_{leak}), \quad (1.43)$$

where $\rho_{Ca_{ER}}$ is the ER-to-cytoplasm volume ratio. The time-scaling functions $T_X(x)$, for $X \in \{\text{Ca}, \text{Ca}_{ER}\}$, account for the effect of intracellular calcium buffers and follow:

$$T_X(x) = 1 + \frac{B_T}{K_{dB} \left(1 + \frac{x}{K_{dB}}\right)}, \quad (1.44)$$

with B_T the total buffer concentration and K_{dB} the dissociation constant.

This detailed biophysical representation of membrane and calcium dynamics allows the model to capture the critical interaction between synaptic inputs, action potential backpropagation, and intracellular calcium signaling that underlie plasticity induction.

CaMKII Pathway and Endocannabinoid Biosynthesis

The full phosphorylation cycle of CaMKII was modeled according to the approach proposed by Graupner and Brunel [40], originally developed for hippocampal spike-timing-dependent plasticity (STDP). However, Cui et al. (2016) applied this framework to the striatal context, specifically modeling medium spiny neurons (MSNs), which feature notable biochemical differences. For instance, protein phosphatase 1 (PP1) is regulated in MSNs by the striatum-specific phosphoprotein PPP1R1B (also known as DARPP-32), rather than by Inhibitor-1 [2], as in hippocampal neurons. Despite these biological differences, the authors argued that the essential functional divergence in the signaling cascade ultimately manifests at the level of protein kinase A (PKA) activation.

To reflect striatal signaling characteristics, they modified the calcium dependence of PKA activation by altering the Hill coefficient from $n_{PKA} = 8$ to $n_{PKA} = 3$, thereby reducing the cooperativity of calcium input on PKA signaling. This modification captures the experimentally observed sensitivity range of striatal PKA activity and ensures compatibility with the observed STDP profiles in the corticostriatal pathway.

Endocannabinoid Synthesis Pathways. Both anandamide (*AEA*) and 2–arachidonoylglycerol (2-*AG*) serve as retrograde messengers triggering pre-synaptic CB1R activation and subsequent modulation of synaptic strength. The synthesis pathways for these molecules were implemented in detail.

Production of *AEA* follows a two-step enzymatic cascade based on Starowicz et al. (2007) [99].

For 2-*AG* synthesis, the model follows the pathway described by De Pittà et al. (2009) [23]. Diacylglycerol (DAG), the precursor of 2-*AG*, is synthesized in a calcium- and IP_3 -dependent manner.

$$\frac{dDAG}{dt} = R_p(C, IP_3, G) - \frac{r_{DGL} \cdot DAGL \cdot \varphi_{DAGL} \cdot DAG}{DAG + K_{DAGL}} - r_{DAGK} \cdot DAG. \quad (1.45)$$

DAG is then converted to 2-*AG* by DAG lipase- α (DAGL α), whose own activity is also calcium-sensitive.

$$\frac{d2-AG}{dt} = \frac{r_{DGL} \cdot DAGL \cdot \varphi_{DAGL} \cdot DAG}{DAG + K_{DAGL}} - r_{MAGL} \cdot 2-AG. \quad (1.46)$$

Glutamate Clearance and post-synaptic Spike Currents. The concentration of glutamate in the synaptic cleft was modeled using a simple exponential decay:

$$\frac{dGlu}{dt} = -\frac{Glu}{\tau_{glu}}, \quad (1.47)$$

where τ_{glu} represents the decay constant of glutamate concentration following vesicular release. When a pre-synaptic spike occurs, *Glu* receive an instantaneous increment of amplitude Glu_{max} .

1.5 Conclusion

In this chapter, we proposed an introduction to neuroscience and computational neuroscience, providing a necessary background for the remainder of the thesis. We then focused on two research paper, each of which constitutes a building block for the following chapters and will be referred to throughout this work.

Section 1.4 presented the mechanistic model developed in Cui *et al.* (2016) [21]. A distinctive feature of this model is its incorporation of the eCB pathway, which mediates a form of LTP induced with very few spike pairings (5 to 15). As we will return to later, this eCB-LTP is a strong candidate for supporting one-shot learning. In Chapter 2, this model will be applied to *in vivo* data obtained from experiments where mice perform a one-shot learning task. We will describe

the data and experimental setup, discuss the difficulties encountered in adapting the model to realistic recordings, and detail the methodological strategies used to address them. Finally, we will present the predictions made by the model regarding synaptic plasticity during one-shot learning and how these predictions were tested experimentally.

Section 1.3 introduced the work of Montbrió–Pazó–Roxin (2015) [69] and the Lorentzian Ansatz. This mean-field framework will serve as the basis for an extension in which I incorporate synaptic weight heterogeneity. The ultimate goal of this line of work is to pave the way for including synaptic plasticity rules within mean-field models. This complementary approach seeks to provide insights into how different learning paradigms –particularly one-shot learning – can emerge at the network level.

Chapter 2

Exploring the Endocannabinoid Engram Hypothesis for One Shot Learning Through Simulations

Il en est ici comme de tous les autres arts : le modèle qui réussit le mieux en petit souvent ne peut s'exécuter en grand.

Georges-Louis Leclerc de Buffon

2.1 Introduction

Fast learning – introduced Sec 1.1.6 – is a crucial ability that allows animals, including humans, to adapt quickly to novel environments or stimuli based on only a few exposures [19, 31]. Despite its clear importance for survival and decision-making, the engram underlying fast learning is still elusive [84]. Moreover, the inherently brief time scale of fast learning (on the order of seconds or less) implies that it relies on sparse [102] or burst-like [97] neural activity, differing from classical incremental learning paradigms.

In the hippocampus, studies [9, 67] have revealed how dendritic plateau potentials can rapidly assign importance to spatial locations via synaptic potentiation occurring after only a handful of activations. These findings support the existence of single-trial learning engrams, but their generalizability to other brain regions and tasks remains underexplored.

The dorsal lateral striatum (DLS) is a brain region classically associated with sensorimotor integration and procedural learning. It has been extensively studied in the context of habit formation and long-term skill acquisition, and identified as critical in late learning stages [79]. However, growing evidence [7, 52] suggest that the DLS is also involved in early learning stages and may even contribute to rapid adaptations in behavior.

Recent *ex-vivo* electrophysiological experiments have provided compelling support for this view. In particular, patch-clamp recordings in corticostriatal slices have demonstrated that synaptic plasticity in the DLS can be mediated via two distinct

pathways:

- **An NMDA-dependent pathway**, which supports gradual, cumulative plasticity across repeated pairings.
- **An endocannabinoid (eCB)-dependent pathway**, which classically has been reported as supporting LTD [30,35]. However for a few years, pioneer collaborative works between Laurent Venance and Hugue Berry's teams demonstrated that it can also induce LTP after only a few spike pairings. This new plastic scheme has strong dependence on the exact timing between pre- and post-synaptic spikes [19, 21].

These findings demonstrate that the DLS is capable of bidirectional plasticity, depending on the recruited pathways and stimulation conditions. Importantly, the DLS is implicated in both early and late stages of learning. More specifically, eCB-LTP can be induced under sparse patterns of activity, while the inherently short timescale of fast learning suggests that it relies on sparse or burst-like firing events. Taken together, this indicates that both incremental and fast learning modes could be supported within the same structure, namely the DLS. In this context, the endocannabinoid pathway emerges as a particularly strong candidate mechanism for fast learning.

In the following sections, we simulate the eCB-based model introduced by Cui et al. (2016) and evaluate its potential to reproduce fast learning paradigm in behavioral data from mice.

2.1.1 Numerical Simulation as a Window into In Vivo Plasticity

Despite the compatible properties between eCB-LTP and One-Shot-Learning, direct evidence linking eCB plasticity to *in vivo* fast learning behavior remains elusive. Through an ongoing collaboration with the Venance lab (Collège de France) and notably ex-PhD student Charlotte Piette, our approach aims to integrate computational modeling and *in vivo* recordings. This synergy will help uncover whether eCB-LTP dynamics are indeed recruited as part of the engram supporting fast sensorimotor learning.

The modeling work of Cui et al. (2016) provided a mechanistic framework for understanding the endocannabinoid (eCB) pathway. This model successfully reproduces the synaptic plasticity changes induced by specific stimulation protocols in various conditions. As such, it offers a valuable tool to bridge the gap between experimental recordings and underlying synaptic dynamics. Remarkably, the models demonstrated its capability to adapt to several different experimental context. It served as a basis to study the interaction of the eCB STDP with GABA, Dopamine or Noise [20, 43, 106]. Its robustness make this model as a reliable tool to bridge the gap between experimental recording and underlying synaptic dynamics. Simulations allow to reveal modifications triggered by realistic corticostriatal activity (See Fig 2.1), in situations it can not be recorded.

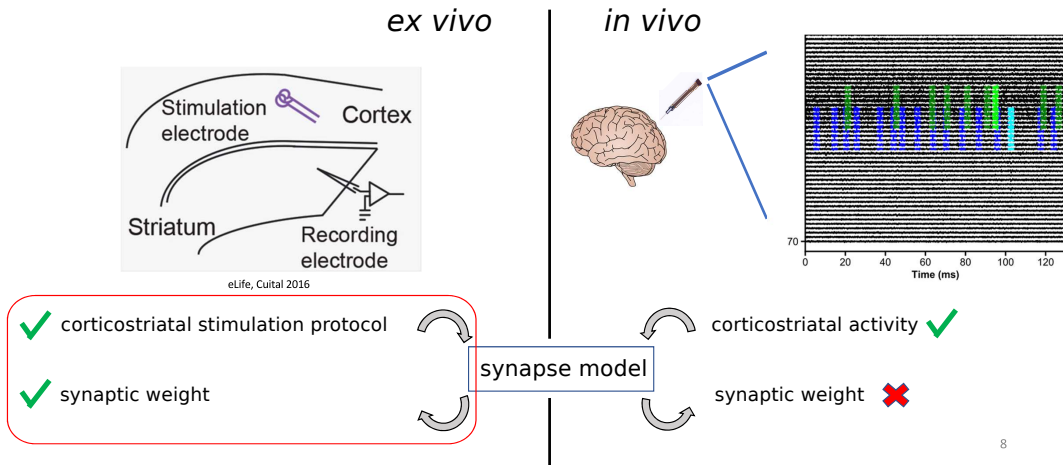


Figure 2.1: Summary of the joint experimental-computational pipeline combining *in vivo* recordings and simulations. In the *ex vivo* context, both corticostriatal stimulation protocols and the resulting synaptic weight changes can be directly measured. Computational modeling is then used to reconstruct how synaptic weights emerge from neural activity patterns. In contrast, in the *in vivo* context, modern Neuropixel recordings provide access to individual neuronal activity with high precision. However, direct measurement of synaptic weight is not feasible. To bridge this gap, we employ the previously established model to infer synaptic weight dynamics from recorded activity through simulation.

2.1.2 Model Overview

We used the mechanistic model developed by Cui et al. (2016), presented section 2.1.2, specifically designed to simulate synaptic plasticity at cortico-striatal synapses. The model integrates two major biochemical signaling pathways known to mediate plasticity:

- **NMDA-dependent pathway**, governing post-synaptic CaMKII activation;
- **Endocannabinoid (eCB) pathway**, mediating pre-synaptic modulation via CB1R.

This model operates by receiving two spike trains—one pre-synaptic and one post-synaptic—and simulating the resulting synaptic weight changes over time through a set of 28 coupled ordinary differential equations (ODEs). It separately computes the contributions of NMDA and eCB cascades, allowing the study of their respective impacts on plasticity.

The model was originally calibrated using *ex vivo* brain slice data from mouse dorsolateral striatum, under spike-timing dependent plasticity (STDP) protocols. It successfully reproduces the bidirectional STDP observed experimentally, including the distinct induction windows depending on stimulation repetition and timing (see Fig 2.2).

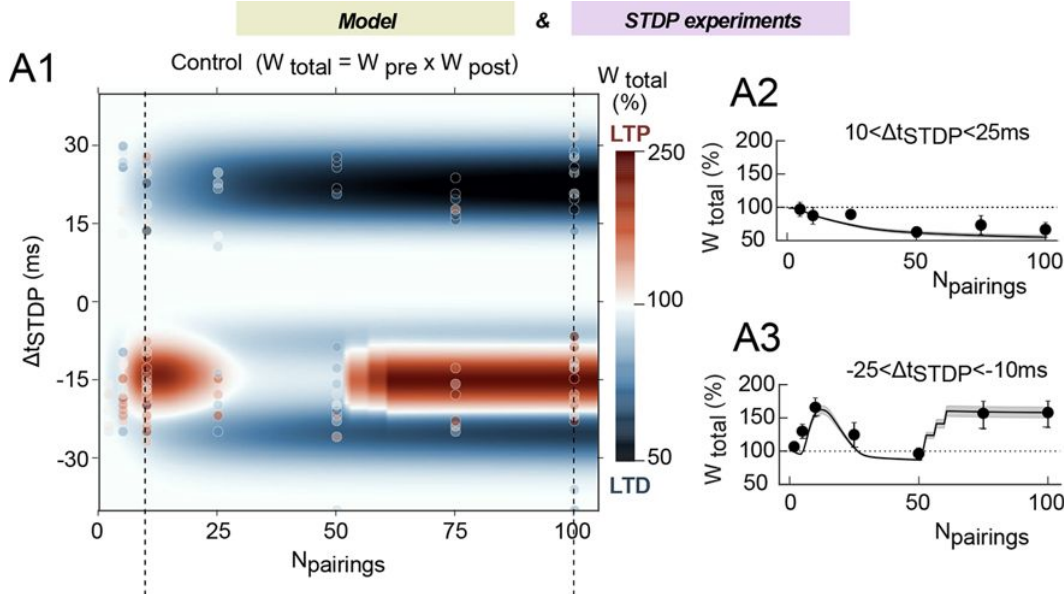


Figure 2.2: Figure from Cui et al. 2016 [21]. **A1.** STDP outcomes produced by the Cui et al. model under different pre-post pairing conditions. Plasticity sign and magnitude vary as a function of pairing number and timing interval (Δt). **A2-A3.** Comparison between model outcome (line) and experimental observation (dot). The model successfully capture the plasticity changes as a function of number of pairings, for two different timing of pairings.

2.2 ExperimentCuial Setup

2.2.1 The sticky tape avoidance task

The experimental paradigm, termed **Sticky Tape Avoidance** (STA), was developed by the Venance Team to investigate one-shot learning in a naturalistic, nonaversive context. This behavioral task is designed to elicit learning without the use of rewards, punishments, or fear-inducing stimuli.

In the STA paradigm, a small, loosely affixed piece of tape is placed in an open-field arena with its adhesive side facing upward. Mice are free to explore the arena. Upon encountering the tape, they typically momentarily stick for various time, and after active attempts, finally succeed to remove it. The task consists of two sessions:

1. A familiarization session, during which the mouse first encounters the tape;
2. A retrieval session, performed 24 hours later, in which the tape is placed in a different location.

To control for novelty and object-related exploration, a control group of mice was exposed to identical conditions but with a non-sticky piece of tape. Avoidance behavior of sticky tape, during retrieval session compared to familiarization session is a manifestation of an acquired long term memory. Such adaptation would occurs literally after a one-shot experience, namely a one shot learning situation. Typical example of a successful learning behavior is shown Fig 2.3 A.

A total of 54 mice were used in the main (sticky tape) group, and 22 mice served as controls. To compare avoidance behaviour between sessions, an avoidance index was quantified through a PCA method mixing several metrics, including:

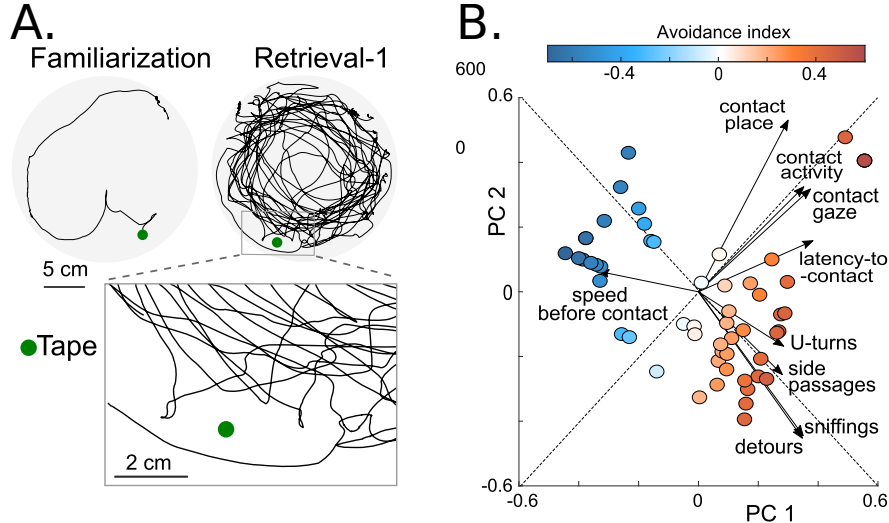


Figure 2.3: Figure from Piette *et al.* (2024) [83]. **A.** Example of a successfull mouse trajectory at familiarization and first retrieval. At familiarization, contact with tape is almost instantaneous, with no detours. At retrieval session, the full arena is explored without contact with tape, showing evidence of tape avoidance. Grey area is the arena space, green dot is the tape position. **B.** Principal component analysis of all displayed factors. Avoidance index is a linear combination of two main components. Arrow indicate the contribution of each factors to components.

- Time spent in the region near the tape,
- Latency before first contact with the tape,
- Number of detours around the sticky tape,
- Sniffing episode of the sticky tape.

The full metrics and PCA are shown Fig 2.3 B.

During the familiarization session, both experimental and control groups explored the arena similarly and contacted the tape directly. However, in the retrieval session, mice from the sticky tape group displayed a marked change in behavior: while only 7% exhibited more than two detours during familiarization, this number rose to 63% during retrieval (Fig 2.4 A). This clear separation between STA and n-STA is globally confirmed by the avoidance index (Fig 2.4 B). This indicates the acquisition of a memory associated with the experience of walking on the tape and being stuck.

Interestingly, the duration of tape contact and removal during the initial session varied widely, ranging from a few seconds to several minutes. Regarding the one-shot-learning paradigm, Venance's team applied a methodological separation, dividing mice into two groups:

- **Short-contact group:** Mice that successfully removed the sticky tape in less than 20 s. Within such a brief period, mice could only attempt a few removal trials as a direct reaction to the tape contact, with immediate success

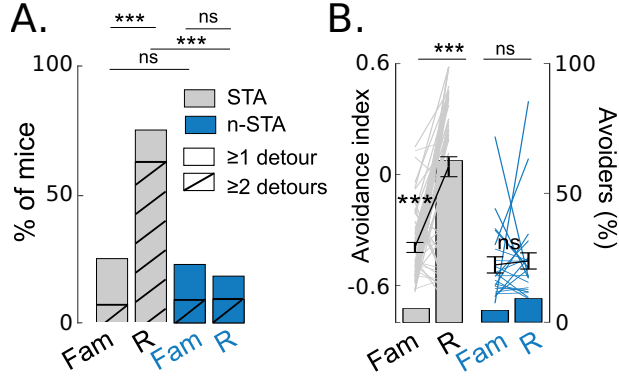


Figure 2.4: Adapted from Piette *et al.* (2024) [83]. **A.** Comparison of percent of mice performing at least 1 (filled area) or 2 (striped area) detours between familiarization (Fam) and first retrieval (R) session for both STA (grey) and non-STA (blue) setup. **B.** Comparison of avoidance index and avoiders percentage between familiarization (Fam) and first retrieval (R) session for both STA and non-STA setup. Paired two-sample t-test and McNemar test.

upon completion. These mice thus experienced a genuine one-shot learning situation.

- **Long-contact group:** Mice that required more than 20s to remove the tape, or failed to do so altogether. In the latter case, failure was defined as remaining stuck for several minutes, requiring human intervention for removal. In these long-contact cases, mice often alternated between active removal attempts and inactive phases, such as freezing or showing signs of discomfort during locomotion. Although these animals encountered the sticky tape only once, the extended interaction allowed multiple attempts separated by inactivity phases. This differs qualitatively from the short-contact case, questioning whether distinct mechanisms of learning or performance are at play.

Importantly, the contact duration was not correlated with subsequent avoidance behavior, suggesting that only a brief initial experience (a few seconds) was sufficient to induce lasting learning.

To evaluate memory retention, 17 mice underwent additional retrieval sessions up to one month after the initial exposure. These animals continued to exhibit significant avoidance behavior, comparable to their 24-hour retrieval performance. Moreover, a subset of 16 mice was tested in other striatum-dependent tasks, and their performance in those paradigms was independent of their STA results.

Altogether, the STA paradigm provides a robust and ethologically valid framework to study fast, single-trial learning, offering a rare behavioral correlate for investigating rapid synaptic plasticity mechanisms such as those mediated by the endocannabinoid system.

2.2.2 Raw Data Processing

During sticky tape avoidance task, the neural activity of some mice was recorded using **Neuropixels probes**. Those last generation probes offer high spatial and

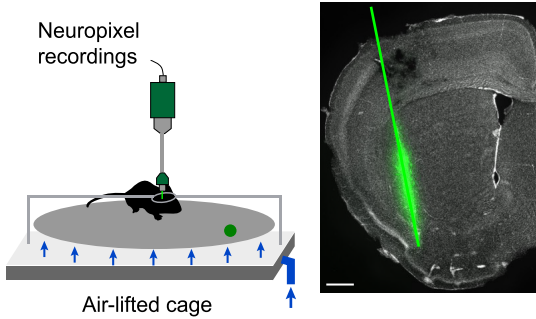


Figure 2.5: Figure from [83]. Schematic representation of neuropixel recording setup & brain slice image displaying neuropixel trajectory, used during craniotomy as referred to at Sec 2.2.2.3.

temporal resolution. Each probe features 382 recording sites distributed along a 10 mm shaft, with a vertical resolution of $20\text{ }\mu\text{m}$ [50]. During recording sessions, the mouse head was fixed to ensure probe stability, while allowing for voluntary locomotion using a mobile floor system. This floor was maintained in a floating state using an air cushion, enabling walking and exploration despite head fixation. However, this setup still slightly differ from completely free moving condition. (See Fig 2.5).

Signal acquisition was conducted using the **SpikeGLX** system. The signal was split into two frequency bands:

1. A **spike band** sampled at 30 kHz and high-pass filtered above 500 Hz;
2. A **local field potential (LFP) band** sampled at 2.5 kHz and low-pass filtered below 1000 Hz.

2.2.2.1 Spike sorting.

Spike sorting is the processing of electrophysiological data, that allow the extraction of individual neural activity from the electrical signal.

This step was performed using **Kilosort 2.5** [76], an advanced algorithm that combines spike detection and clustering into a single optimization procedure. Traditional spike sorting pipelines treat detection and clustering separately. In contrast, Kilosort uses a template-matching approach where spikes are matched against learned templates, which are iteratively refined using singular value decomposition (SVD) of spatiotemporal waveforms. This joint optimization improves the resolution of overlapping spikes and handles probe drift more effectively [77].

The output consists of:

- Spike times,
- Spatiotemporal waveforms,
- Assigned clusters representing individual putative neurons,
- Electrode channel locations for spatial localization,

- Confidence metrics and quality descriptors (e.g., isolation distance, amplitude, etc.).

2.2.2.2 Manual curation.

Post-processing curation – on which I contributed – was performed using the open-source software **Phy** [88]. This GUI-based tool provides access to a wide range of features for reviewing and refining spike clusters. Among them are present:

- Inter-spike interval (ISI) histograms,
- Waveform visualizations (mean and individual),
- Auto- and cross-correlograms,
- Amplitude and refractory period distributions.

Clusters can be manually split, merged, or discarded based on these metrics to ensure high-quality single-unit isolation. The final curated dataset typically included several hundred neurons per recording, and occasionally exceeded one thousand units.

2.2.2.3 Anatomical localization.

Thanks to craniotomy (See Fig 2.5) coordinates provided by collaborator Charlotte Piette, I directly had access to the brain region corresponding to each recording channel, distinguishing between neurons located in the cortex and those in the DLS.

2.2.2.4 Cortical interneuron filtering.

After inspection of firing statistics and discussions with Venance’s team, I add an other preprocessing of data. This additional step aimed to exclude **cortical interneurons**, which are not relevant for cortico-striatal projection analyses. They are intermediate neuron based in the cortex which project onto the cortex, contributing to local activity only. Interneurons are characterized by narrow spike waveforms and higher firing rates or bursting activity. I applied heuristic thresholds:

- Mean firing rate exceeding 15 Hz;
- Instantaneous burst rate exceeding 200 Hz.

Putative interneurons meeting these criteria were manually reviewed and excluded from subsequent analyses.

Final number of neurons by region by mouse are given Tab 2.1. Cumulative distribution function of spikes during contact are displayed Fig 2.6. A clear separation in number of spikes can be observed, between short contact group (light pink) and long contact group (green). This separation do not hold when considering the mean firing rate during contact period.

2.3. Adaptation and Application of the Synaptic Plasticity Model to In Vivo Data: Methods and Results

Label	<i>V7260</i>	Mouse1	<i>V7265</i>	<i>V4606</i>	Black	Blue	Red	<i>V4607</i>	<i>V4609</i>
Pre	77	58	77	98	32	32	37	38	70
Post	111	74	51	27	96	70	148	48	36

Table 2.1: Number of validated clusters (*i.e.*, neurons) for each mouse. Clusters are separated into **Pre** and **Post** labels, corresponding respectively to cortical and striatal regions. Mouse names in italics (*V7260*, *V4607*, *V4609*) indicate subjects integrated during the course of the study; they may therefore be absent from sections describing our early work.

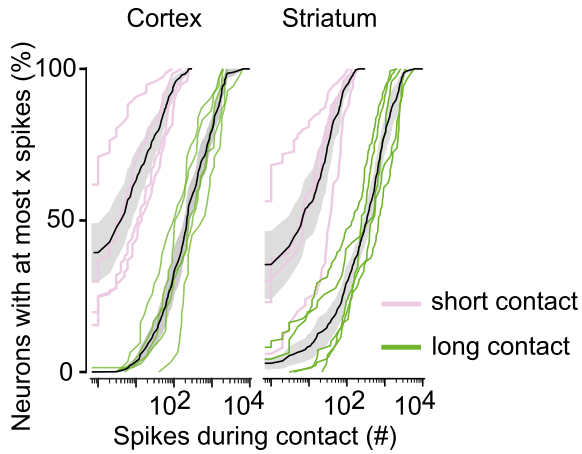


Figure 2.6: Cumulative distribution function for number of spikes during contact. Individual curves are displayed for each mice, separated in short contact (pink) and long contact (green). Standard error of the mean are shown for each group (black curve and grey area). From Piette *et al.* 2024 [83]

2.3 Adaptation and Application of the Synaptic Plasticity Model to In Vivo Data: Methods and Results

In the following section, I detail my personal contribution through this thesis. The major part of my work has been to apply the mechanistic synaptic plasticity model of Cui *et al.* (2016) to the characteristics of our *in vivo* Neuropixel recordings. While the original model was calibrated under controlled *ex vivo* STDP protocols, the rich, bursty, and heterogeneous spike patterns recorded during freely moving behavior required both numerical adjustments and conceptual considerations. I begin by outlining the numerical implementation and the specific challenges arising from the discrepancy between *ex vivo* and *in vivo* conditions. I then describe the steps taken to mitigate these issues, including strategies to prevent post-synaptic saturation, different approaches to connect cortical and striatal neurons, and parameter exploration for glutamate release. I continue with the presentation of the pathway-specific analysis for NMDA and eCB signaling, and introduce the *Plasticitymeter* method for quantifying eCB-mediated dynamics. I then expose the experiments run by collaborators from Laurent Venance’s Team at College de France, who tested the prediction made by the model. Finally, I report exploratory directions taken during

the research process and stemming from the results.

2.3.1 Numerical Implementation

The model described by Cui et al. (2016) [21] – originally implemented in matlab – was reimplemented in Python. It takes two arrays –corresponding to spike trains of one pre-synaptic and one post-synaptic– and simulates the evolution of synaptic weight over time. The output is split into two components: the post-synaptic weight (associated with the NMDA pathway) and the pre-synaptic weight (associated with the endocannabinoid, eCB, pathway).

The simulation relies on solving, over time, a set of 28 ordinary differential equations describing the dynamics of various biological components and molecular species within the synapse (Sec. 2.1.2). Numerical integration was performed using the Runge–Kutta 4(5) (RK45) adaptive scheme, as implemented in the `scipy.integrate` library [107]. The integration loop was optimized using `numba` [55] for computational efficiency. The resulting workflow and data handling procedures were encapsulated into a custom Python library named `Synacomp`, designed to support synaptic plasticity modeling and simulation (available at <https://gitlab.inria.fr/aistrosight/synacomp>, see Sec 2.5 for more details).

2.3.2 In Vivo / Ex Vivo Challenges

A key challenge of this study lies in bridging the *ex vivo* modeling and *in vivo* experimental data. The original Cui et al. model was calibrated on brain-slice experiments using low-frequency (1 Hz), short-duration (< 1 min), and well-controlled STDP stimulation protocols. In contrast, *in vivo* spike trains recorded via Neuropixels span several minutes and contain high-frequency bursts (>100 Hz), introducing a more complex and dynamic context.

A second fundamental difference concerns the nature of cortical stimulation. In the original *ex vivo* experiments, electrical stimulation was applied to cortical tissue, triggering the activity of large populations of neurons —about thousands— simultaneously. However, the synaptic model itself considers a single, abstracted synapse defined by a pair of spike trains (pre- and post-synaptic). In reality, the synaptic changes observed experimentally emerge from the convergent activity of many pre-synaptic cortical neurons projecting to a single striatal neuron (See Fig 2.7).

Neuropixels provide us with spike trains from individual cortical neurons, but the integration of their combined influence onto a striatal target is not trivial. We do not know the EPSPs induced by each spike, nor the rule by which multiple inputs sum within the dendritic tree. Furthermore, connectivity is unknown: we do not know which recorded cortical neurons are effectively connected to a given striatal neuron, which is crucial given the spike-timing dependence of plasticity.

This raises the central modeling question of how should cortical spike activity be represented within the plasticity model. We identified two main approach.

- A **one-to-one** configuration, where each individual activity is preserved and used as such in the model.
- An **all-to-one** configuration, where the collective activity of multiple cortical neurons is integrated as a global pre-synaptic drive.

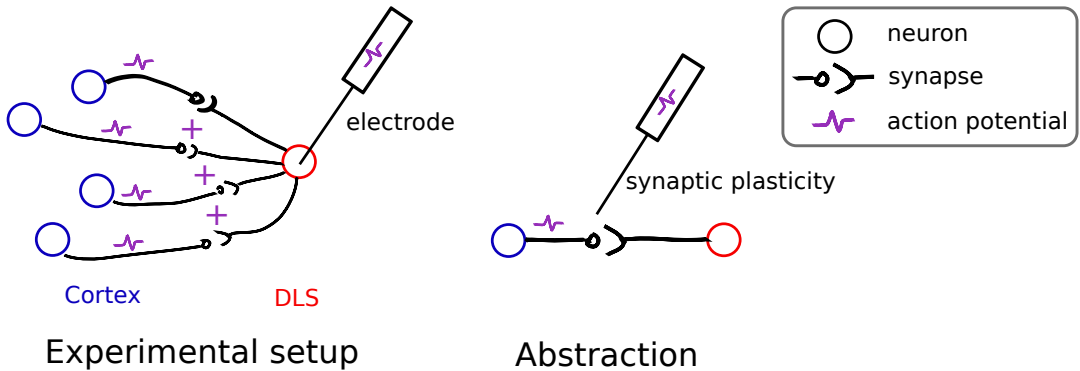


Figure 2.7: Schematic illustration of the difference between experimental and modeled conditions. **Left:** In *ex vivo* experiments, electrical stimulation of the cortex activates a large population of cortical neurons, leading to convergent synaptic input onto a single striatal neuron. **Right:** In the model, the synapse is represented abstractly by a single pair of spike trains (one pre- and one post-synaptic), ignoring the large-scale convergence and variability present in the biological situation. This discrepancy has major implications for how the model integrates and responds to high-intensity cortical activity.

In the following, we examine the general dynamics of total phosphorylated CaMKII, which lead the post-synaptic weight. Then, we explore both one-to-one and all-to-one strategies, each with its own assumptions and implications, in order to align our experimental observations with the mechanistic model of plasticity.

2.3.3 Post-synaptic weight study

We first examine the analytical properties of the CaMKII auto-phosphorylation cycle, as described in the Graupner–Brunel formalism and implemented with the parameter set proposed by Cui et al. (2016). This preliminary analysis provides insight into the intrinsic dynamics and stability of the post-synaptic component, which will prove critical for interpreting simulation outcomes under high-intensity spiking conditions.

We analyzed the bifurcation diagram of phosphorylated CaMKII subunits as a function of calcium and PP1 concentrations (Fig. 2.9). The system displays a characteristic bistable behavior, with two stable plateaus: a low-phosphorylation state (**DOWN**) and a high-phosphorylation state (**UP**). The resulting dynamics revealed an important feature: the strong asymmetry between the two transitions. Shifts from the UP to the DOWN state are only possible at very low calcium concentrations ($\lesssim 0.175 \mu\text{M}$ for high PP1 levels, and down to $\lesssim 0.09 \mu\text{M}$ for low PP1 levels). In contrast, transitions from the DOWN to the UP state occur once calcium exceeds a low threshold ($\gtrsim 0.225 \mu\text{M}$), largely independent of PP1 levels. These two regimes are separated by a narrow calcium range where a subcritical saddle-node bifurcation and its reversal occur, forming a bistability window.

This result has important implications for the model dynamics. In particular, once CaMKII phosphorylation reaches and maintains the UP state, the window for a transition back to the DOWN state is hard to reach.

Indeed, when examining PP1 equilibrium levels at various fixed calcium concentrations, we find that the equilibrium levels are identical.

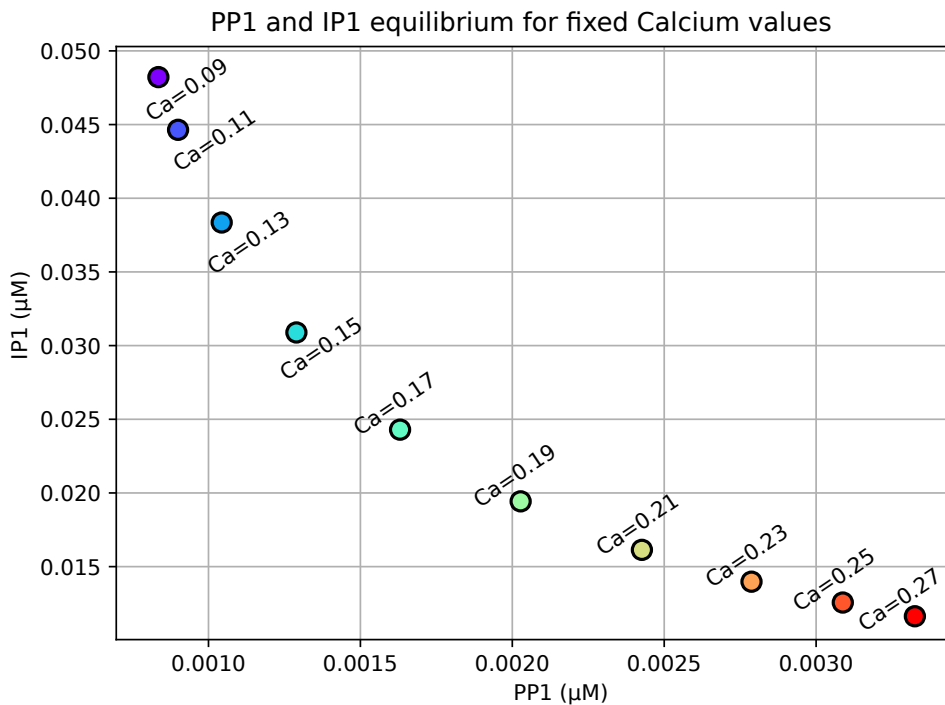


Figure 2.8: Stable state of PP1 & IP1 for fixed calcium value.

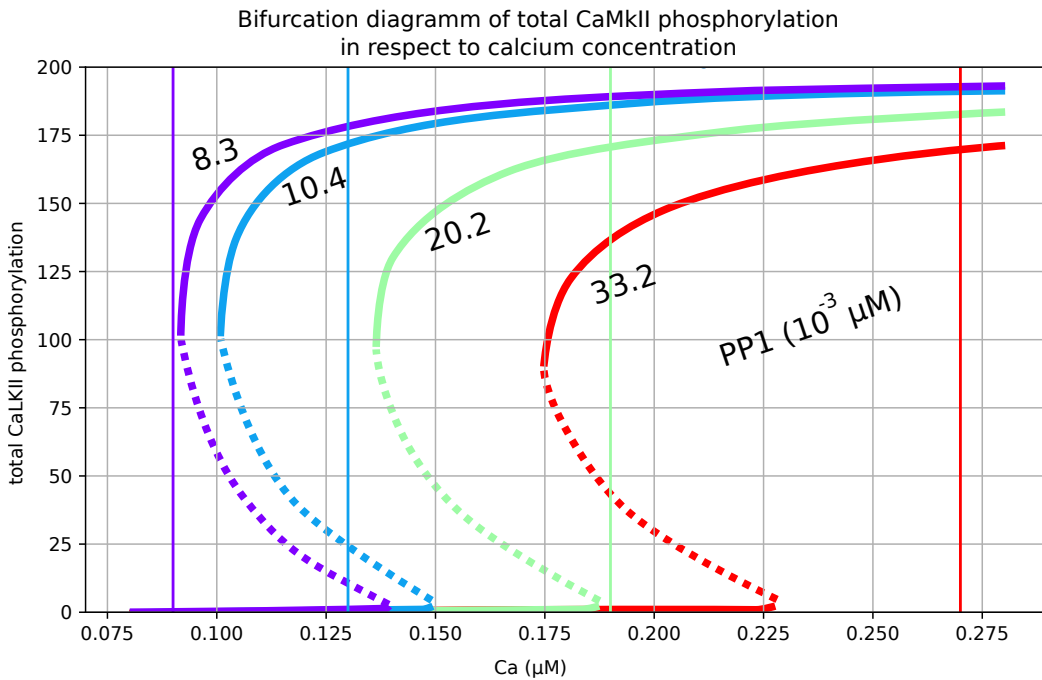


Figure 2.9: Bifurcation diagrams of phosphorylated CaMKII as a function of calcium and PP1 concentration. PP1 values were chosen as the PP1 equilibrium for the fixed calcium values $0.09, 0.13, 0.19$ and $0.27 \mu\text{M}$, See Fig 2.8. Thoses calcium values are denoted with vertical line and match color with the bifurcation for the corresponding PP1 equilibrium.)

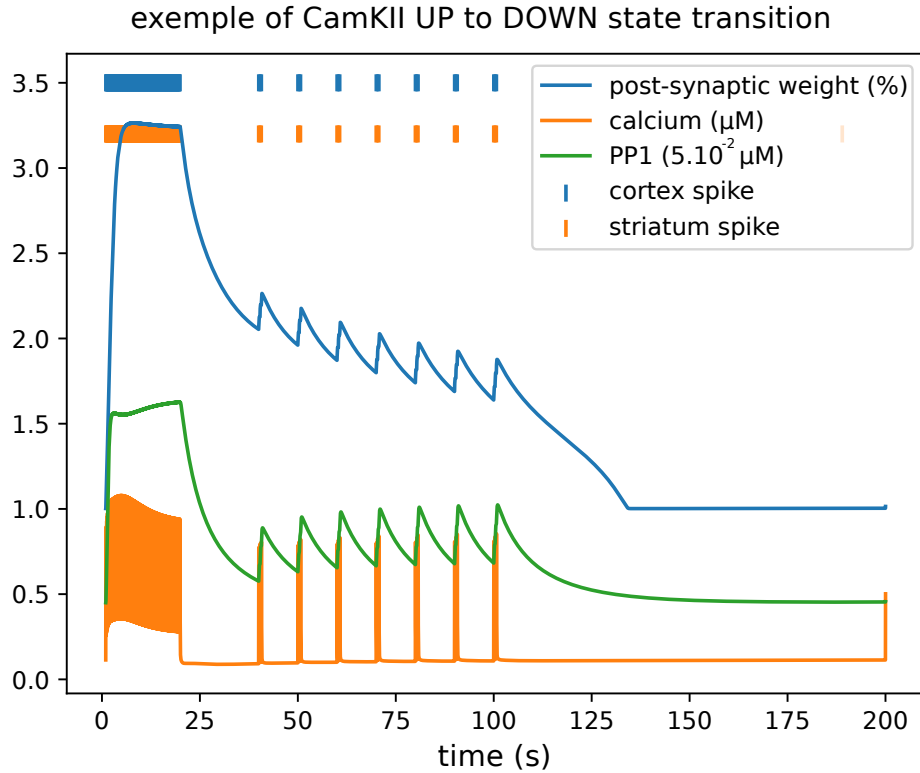


Figure 2.10: Exemple of an UP to DOWN state transition of total phosphorylated CaMKII (blue). Calcium (orange) and PP1 (green) are displayed, as they have been identified as leader of CaMK2 dynamics. On top, pre- and post synaptic spikes are represented by ticks, respectively blue and orange. The depotentiation is obtain with a fragile balance, where short burst are followed by prolonged silence. The fast calcium influx increase both post-synaptic weight and PP1. However, during the following silence, PP1 decrease slowly while calcium rest near to its basal value fastly. Looking at the bifurcation diagram Fig 2.9, depotentiation is triggered. This must be repeated before PP1 drop and prevent depotentiation at basal calcium level.

trations between 0.09 and $0.27 \mu\text{M}$ (Fig. 2.8), one observes that PP1 levels decrease as calcium decreases. However, a transition from the UP to the DOWN state requires very low calcium levels. Yet, at such low calcium levels, PP1 equilibrium is also reduced, which further lowers the calcium threshold required for the transition. As a result, at equilibrium, an UP to DOWN transition require calcium value below $0.09 \mu\text{M}$. Such calcium values are complex to induce – given that basal concentration is $0.1141 \mu\text{M}$ – so even harder to maintain long enough to let the system stabilize in the DOWN state. An other possibility is to rely on the different timescales of calcium and PP1 dynamics through transient excursions (see Fig 2.10 for an example on synthetic data). Both scenarios appear highly unlikely, which is consistent with the fact that such transition were almost never observed in our simulations.

We refer to this phenomenon as **”saturation”**, reflecting the fact that once the post-synaptic weight has reached the UP state, it can no longer effectively depotentiate. This transition can occur rapidly under bursty or sustained neural activity.

An example of saturation is provided in Fig. 2.11. At around 175 s, intense activ-

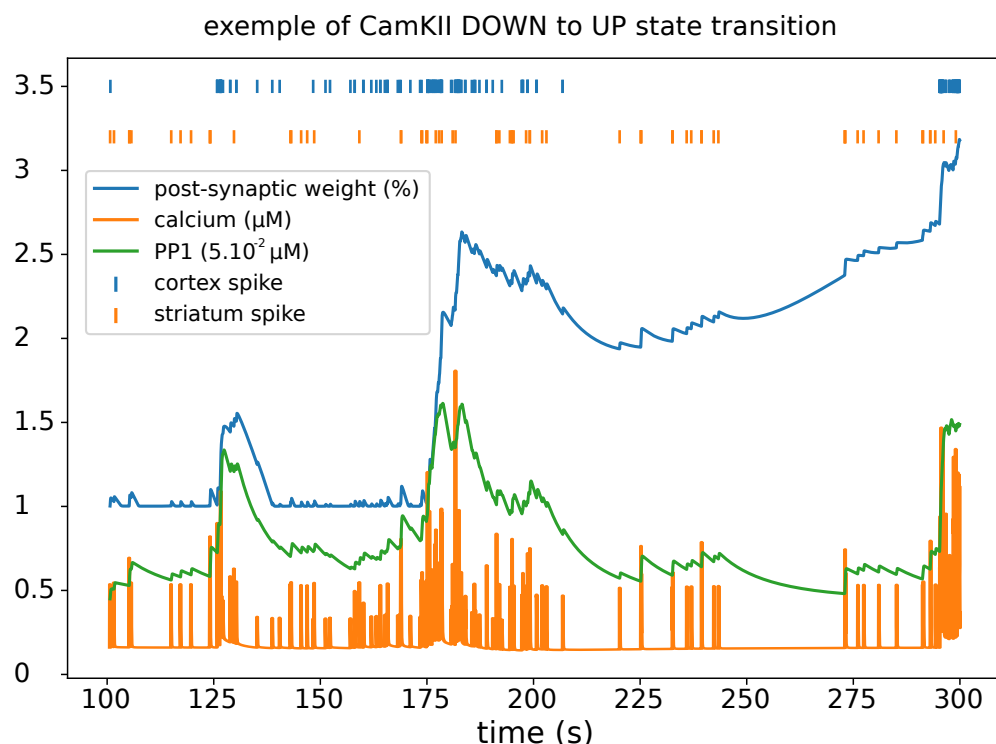


Figure 2.11: Exemple of an DOWN to UP state transition of total phosphorylated CaMKII (blue). Calcium (orange) and PP1 (green) are displayed, as they have been identified as leader of CaMK2 dynamics. On top, pre- and post synaptic spikes are represented by ticks, respectively blue and orange.

2.3. Adaptation and Application of the Synaptic Plasticity Model to In Vivo Data: Methods and Results

ity induces a sharp increase in calcium concentration, leading to a rapid transition of the post-synaptic weight toward the UP state. Subsequently, around 210 s, a quiescent period occurs. This highlights the impact of the different timescales governing calcium and PP1 dynamics. While calcium quickly returns to baseline, PP1 remains at an intermediate level, momentarily allowing for a depotentiation trajectory (see Fig. 2.9). However, this depotentiation process is slow, and PP1 returns to a level that blocks further depotentiation before the post-synaptic weight can fall below the unstable branch of the bistability. As a result, the system remains trapped in the UP state.

From a modeling perspective, *saturation* can play an important role in constraining parameters such as Glu_{\max} , the maximum glutamate release, which strongly influences calcium dynamics. Observing whether or not synapses reach saturation can therefore serve as an indirect validation criterion for realistic parameter ranges. It also provides a rationale for filtering out synapses that are already in a saturated state at baseline, as these are unlikely to exhibit further plastic changes during learning.

This dynamic feature should be regarded as a constrained limit of the model rather than an artifact or defect. As it will be discussed later, although the model yields predictions for the NMDA pathway that may appear "defective" in the context of our *in vivo* experiments, this dynamic reflects how it was originally fitted to *ex vivo* data. Indeed, postsynaptic depotentiation was not observed in the experiments conducted by Venance's team [19, 21]. One of the model's strengths lies in the fact that the precise STDP rule emerges naturally from its mechanistic structure. Interestingly, this STDP rule is inverted compared to the classical Hebbian rule: pre–post pairings induce LTD, whereas post–pre pairings induce LTP. In such conditions, modifying the model mechanisms – which already successfully reproduce *ex vivo* data – is a delicate task, and risks disrupting the unusual and importantly natural emergent STDP property." As will be detailed in the following sections, we therefore adopted alternative strategies to mitigate the effects of saturation without altering the core structure of the model.

2.3.4 All to one connection

To approximate the *ex vivo* stimulation context, the most natural modeling strategy is to aggregate the activity of all recorded cortical neurons into a single composite "super-neuron" projecting onto a given striatal neuron. This mirrors the *in vitro* condition where a single electrode stimulation in the cortex evokes the simultaneous firing of hundreds of excitatory cortical neurons, all targeting one downstream DLS neuron.

In this setup, each detected cortical spike—regardless of its origin—is interpreted as a pre-synaptic event contributing to the glutamatergic drive of the model. The pre-synaptic spike train becomes a merged sequence from all cortical units, thereby mimicking the global input observed in the *ex vivo* experiment.

However, this aggregation leads to intense pre-synaptic activity, far exceeding that of a typical single-neuron-to-neuron connection. To compensate for this, it becomes necessary to rescale the effective glutamate release per spike. This is done by adjusting the parameter Glu_{\max} , which controls the amplitude of glutamate transients following pre-synaptic activation.

Fitting Glu_{\max} is thus critical to ensure that the total glutamatergic input to the post-synaptic neuron remains within biologically plausible bounds, and that the resulting calcium dynamics remain in a regime where plasticity can be induced without saturation effects.

2.3.4.1 Exploring glutamate release

The phosphorylated CaMKII dynamics tend to saturate easily under sustained calcium influx. This behavior emerges from the bifurcation structure of the post-synaptic weight dynamics as a function of calcium concentration: transitions from Down to Up states are readily triggered by moderate and high calcium levels, whereas reverting from the Up to Down state requires very low calcium levels. Consequently, excessive glutamate release – via NMDA and AMPA receptor activation – leads to persistent calcium influx and thus irreversible sustain of the CaMKII autophosphorylation cycle.

Given the high level of spiking activity observed in cortical neurons during behavior, we anticipate that naive application of the model using unscaled Glu_{\max} would lead to systematic saturation of the post-synaptic weight – an outcome not biologically plausible during baseline or neutral episodes.

To address this, we sought to calibrate the glutamate release by identifying the right value of Glu_{\max} that avoids post-synaptic saturation under realistic spike input conditions. Our approach was guided by two key biological assumptions.

1. First, during baseline (i.e., before tape contact), the total phosphorylated CaMKII should remain below the attraction basin of the UP steady state. Entering the UP state prematurely would correspond to long-term potentiation initiated in the absence of behaviorally meaningful events, which contradicts the nature of one-shot learning related to the sticky tape avoidance task.
2. Then, we assume a monotonic relationship between glutamate release amplitude and post-synaptic saturation: stronger Glu_{\max} values induce stronger calcium influx, thereby increasing the likelihood of persistent CaMKII activation and synaptic saturation.

Based on these criteria, we conducted an iterative scan of Glu_{\max} values, simulating the model’s response to baseline spike trains. For each candidate value, we inspected the evolution of the post-synaptic weight and retained only those that avoided saturation throughout the pre-contact period. The toggle value, or, highest admissible value under this constraint, was retained as the calibrated Glu_{\max} , ensuring sensitivity to plasticity without violating biological plausibility.

2.3.4.1.1 pre-synaptic activity only.

As a first step, we calibrated Glu_{\max} using only the pre-synaptic activity from cortical neurons. In this configuration, glutamate is released and can bind to post-synaptic NMDA and AMPA receptors, but no back-propagating action potentials (bAPs) are present–meaning voltage-gated calcium channels such as TRPV1 and voltage-sensitives calcium channels remain inactive. This isolates the contribution of pre-synaptic input to calcium influx and post-synaptic weight changes.

To identify the highest acceptable glutamate release that avoids early synaptic potentiation, we employed dichotomy method. The procedure iteratively adjusted

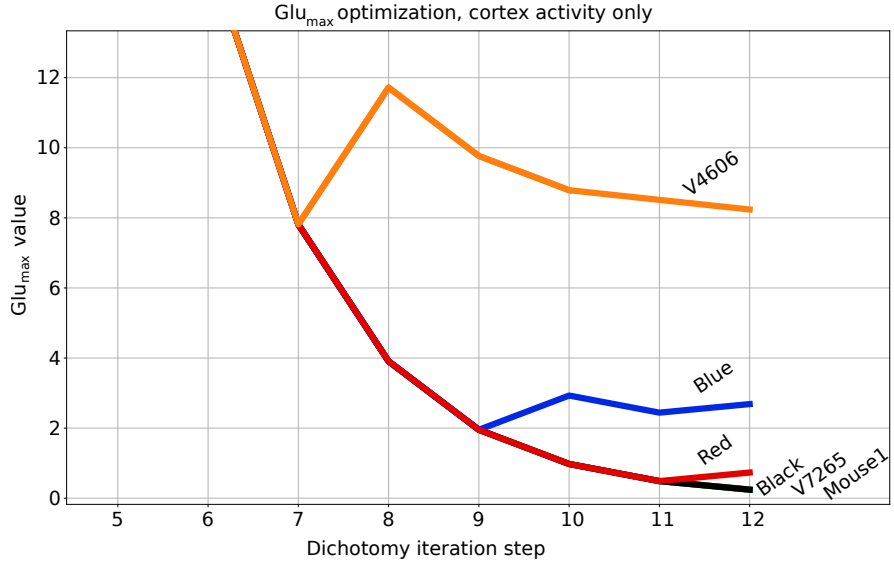


Figure 2.12: Dichotomy exploration tree of Glu_{\max} . Cui *et al.* (2016) model is run with pre-synaptic activity only, unified in a single "super" neuron. Objective is to find the toggle value of Glu_{\max} for which post-synaptic weight do not saturate during baseline period (until 10 second prior to the tape contact). If saturation occurs at step k , next value Glu_{\max}^{k+1} is set to $\text{Glu}_{\max}^k + 2^{-k} \times \text{Glu}_{\max}^0$, and $\text{Glu}_{\max}^k - 2^{-k} \times \text{Glu}_{\max}^0$ otherwise. We started with $\text{Glu}_{\max}^0 = 2000$ taken from the original model [21].

Glu_{\max} : decreasing its value if post-synaptic saturation occurred before the contact event, and increasing it otherwise. This allowed us to converge on a critical value that satisfies our biological constraint (no weight potentiation before behaviorally relevant stimulation).

The full optimization trajectory is illustrated in Fig. 2.12, which shows the evolution of the decision path for each tested value and the resulting toggle found for each mice.

Label	Mouse1	V7265	V4606	Black	Blue	Red
total spikes cortex	237053	297080	325799	285935	70754	100940
max spikes striatum	30804	13537	14110	9869	22128	15263
min spikes striatum	52	12	40	6	68	13

Table 2.2: Number of spikes for each mouse. Clusters are separated into **Pre** and **Post** labels, corresponding respectively to cortical and striatal regions. Mouse names in italics (*V7260*, *V4607*, *V4609*) indicate subjects integrated during the course of the study; they may therefore be absent from sections describing our early work.

2.3.4.1.2 For all synapses. In a second step, we incorporated the post-synaptic activity of individual striatal neurons, thereby enabling the activation of voltage-gated channels and modulating voltage-sensitive channels via bAPs. This allowed us to simulate complete synapses, each defined by a pair of spike trains: a shared pre-synaptic cortical train and a post-synaptic train specific to each striatal neuron. The number of simulated synapses then corresponds to the number of post-synaptic

neurons, ranging from 24 to 148 (See Tab 2.1 for all numbers per mice). Pre-synaptic super neuron range from 70754 to 325799 spikes (See Tab 2.2).

Starting from the global value of Glu_{\max} previously identified under pre-synaptic-only conditions, we refined the calibration for each synapse using a personalized dichotomic search. The objective remained the same: to determine the highest glutamate release value that avoids post-synaptic weight saturation during baseline activity.

Figure 2.13 illustrates this research process across striatal neurons. On the right, histograms summarize the final values obtained for each mouse after 7 dichotomy steps.

Interestingly, all mice exhibited a bimodal distribution of Glu_{\max} values as displayed Fig 2.13. In particular, each animal showed a large subpopulation of synapses that systematically reached post-synaptic saturation, even for the lowest tested glutamate release. Depending on the mice, these value range from $1.4e^{-3}$ to $5.1e^{-2}$. Even during coordinated activity with thousands of quasi-simultaneous spikes, the total glutamate release stay very low compared to the $\text{Glu}_{\max} = 2000$ triggered by a single spike in the original model. These synapses are referred to as "**saturated**" (red). The remaining synapses — referred as "**stable**" (blue), which successfully avoided NMDA-mediated saturation, converged to similar Glu_{\max} values within each mouse, reflecting a shared balance point in the model's dynamics.

NMDA pathway Figure 2.14 shows, for each mouse, the mean post-synaptic weight w_{post} over time, separately for the two identified groups of synapses. This weight reflects the level of phosphorylated CaMKII and thus the activation of the NMDA-dependent pathway. As expected from the Glu_{\max} calibration, the "stable" group exhibits little or no increase in w_{post} prior to tape contact. In contrast, the "saturated" group reaches high w_{post} levels almost instantaneously in some mice, and more gradually in others.

saturated group Except for mouse V7265, which shows an increase in w_{post} just before and during the tape contact, no substantial modulation is observed around the contact period in any mouse. This surprising increase — considered the property of saturated group's synapses which by definition are already in the UP state — is explained by the time windows used for this definition. We did not consider the 10 second preceding contact, as strong interactions with the tape like an approach or sniffing may already have started. With this context, we did not consider that NMDA-LTP should strictly be considered abnormal. This suggests that, for saturated synapses, the transition to the UP state occurs independently of direct sensory input related to the tape.

stable group Surprisingly, in the stable group, a temporary rise in w_{post} is observed at the beginning of the simulation across all animals. This phenomenon can be reproduced in the model by regular, controlled bAPs stimulation alone. When the post-synaptic spike rate increases, a temporary bump in w_{post} appears, which fades with continued stimulation. However, beyond a certain threshold, this bump becomes self-sustaining, triggering a switch to the UP state. Since this transition is driven purely by post-synaptic activity, it is unaffected by the regulation of Glu_{\max} , which only scales pre-synaptic input.

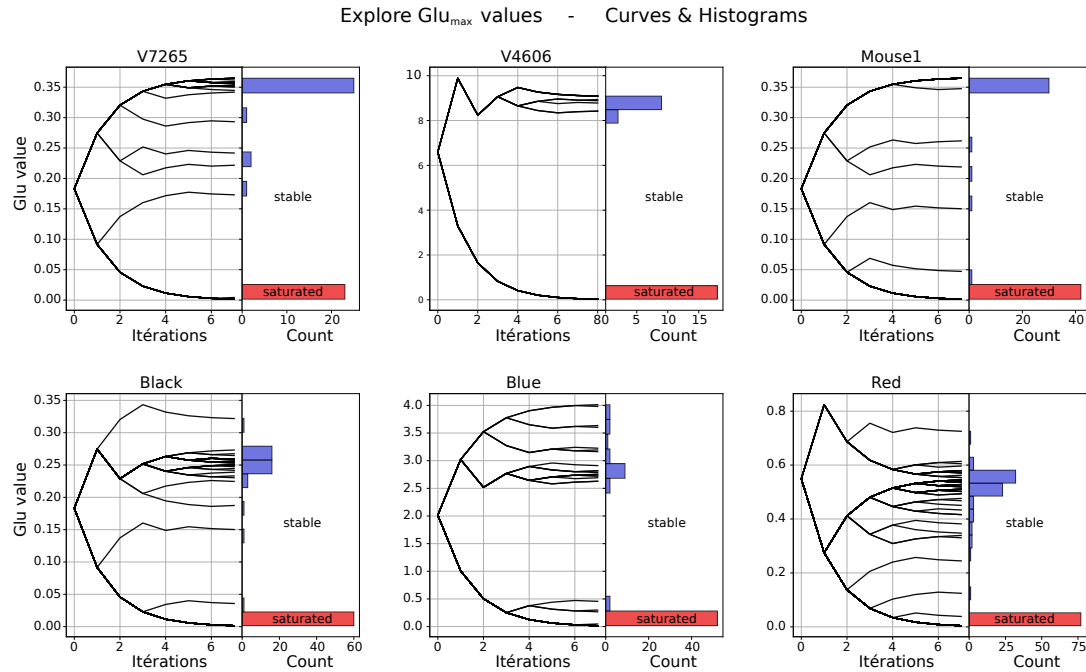


Figure 2.13: Dichotomy exploration tree of Glu_{\max} . Cui *et al.* (2016) model is run with a matched pair of a pre- and post-synaptic spike train. Objective is to find for each pairs its toogle value of Glu_{\max} for which post-synaptic weight do not saturate during baseline period (until 10 second prior to the tape contact). If saturation occurs at step k , next value Glu_{\max}^{k+1} is set to $\text{Glu}_{\max}^k + 2^{-k} \times \text{Glu}_{\max}^0$, and $\text{Glu}_{\max}^k - 2^{-k} \times \text{Glu}_{\max}^0$ otherwise. We started for each mice with the personalized Glu_{\max}^0 taken as the final value obtained in the previous parameter exploration, See Fig 2.12. Distribution of final value is shown as an histogram attached to the right of the tree. Stable (blue) and saturated (red) groups – defined in the main text from the final explored value – are indicated.

Three out of six mice (V7265, Black, and Red) exhibit during the contact a clear shift from the DOWN to the UP state. Remarkably, this transition occurs in mice with vastly different tape contact durations (from approximately 5 seconds to over 100 seconds), suggesting that the observed synaptic switch does not strictly depend on contact duration.

eCB pathway Figure 2.15 shows, for each mouse, the mean pre-synaptic weight w_{pre} over time, computed separately for the same previous two groups of synapses: “saturated” and “stable.” The pre-synaptic weight is controlled by the activation CB1 receptors, which are modulated by endocannabinoids, primarily 2-arachidonoylglycerol (2-AG) and anandamide (AEA), produced in a calcium-dependent manner.

saturated group For the “saturated” group, four out of six mice exhibit a slow but consistent decrease in w_{pre} across the entire simulation window. This corresponds to a long-term depression -like dynamic in these synapses. The two remaining mice (V7265 and Blue) show stable or slightly fluctuating levels without clear potentiation or depression. Recall that the “saturated” group corresponds to synapses for which Glu_{max} had to be minimized to avoid post-synaptic saturation—resulting in low calcium influx. Because the synthesis of 2-AG is calcium-dependent, the insufficient calcium levels prevent CB1R activation strong enough to trigger LTP, favoring instead either no change or a slow drift toward LTD.

stable group In contrast, the “stable” group exhibits a progressive increase in w_{pre} for all mice. In some cases (e.g., V7265, Black and Red), this increase becomes steeper during the tape contact period. Though, similar short monotonic trends can also be observed during baseline.

Interestingly, the slow, monotonic nature of the observed dynamics, even during baseline, suggests a form of pre-synaptic “saturation” or bounded accumulation in w_{pre} , analogous to the bistable behavior observed post-synaptically with CaMKII. This impression of saturation finds its root in the parameters of the model.

eCB LTP-LTD balance We remind that pre-synaptic weight dynamics in the model are governed by the following differential equation:

$$\frac{dw_{\text{pre}}}{dt} = \frac{1}{\tau_{\text{pre}}} (0.5 - 0.2H_{\text{LTD}} + 15H_{\text{LTP}} - w_{\text{pre}}) \quad (2.1)$$

where H_{LTD} and H_{LTP} are Heaviside functions that depend on the concentration levels of the endocannabinoids 2-AG and AEA, respectively. By construction, the model ensures that both Heaviside functions cannot be simultaneously active. Notably, the multiplicative coefficients in this equation reveal a strong asymmetry between the two forms of plasticity: LTP exerts a potentiation 75 times greater than the depression induced by LTD.

Our simulations are based on *in vivo* spike trains—which are both longer and more bursty than the low-frequency protocols used during *ex vivo* experiments. Thus, the synaptic cleft is frequently exposed to diverse quantity of glutamate release, unless it is almost shut down as for the “saturated” subgroup. In such conditions, calcium influx is likely to reach thresholds sufficient to intermittently trigger both LTD and

2.3. Adaptation and Application of the Synaptic Plasticity Model to In Vivo Data: Methods and Results

LTP pathways. However, due to the imbalance in gain between the two mechanisms, any activation of LTP, even if sparse, will dominate the overall trajectory of w_{pre} . For LTD to effectively balance this, it would require highly specific temporal patterns that disproportionately and selectively activate LTD over LTP—by a factor of 75. Moreover, these LTD-inducing patterns would need to occur under glutamate release levels high enough to also permit LTP induction, making the compensation extremely unlikely.

This inherent imbalance in the model leads to a dichotomous outcome: either glutamate release is too low to induce LTP, resulting in a slow decay or stabilization (the “saturated” group), or it can cross the LTP threshold—which will then happen frequently—and rapidly drives w_{pre} to high values (the “stable” group).

As a consequence, this saturation effect likely masks any pre-synaptic plasticity that might be specifically associated with the learning event (i.e., the tape contact). Once w_{pre} reaches a ceiling due to early LTP accumulation, the synapse loses its capacity to reflect further potentiation associated with the learning experience. This undermines our ability to identify any distinct endocannabinoid-mediated signal that correlates with the behavioral marker of one-shot learning.

The adaptation of plasticity gain parameters to *in vivo* conditions is an important and compelling question. However, results obtained from brain-slice recordings impose strong constraints on the parameter space of the model. Most parameters correspond to physiological constants that should remain valid in any—including the *in vivo*—context. In contrast, glutamate release clearly requires adaptation depending on how the neural activity is transferred to the synapse model, defining what a spiking event biologically mean in the model. This is the aspect we focused our efforts on. Adjusting additional parameters, such as plasticity gain, would require substantial rework of the model. This in turn would necessitate new experimental data to fit and validate the added mechanisms, a task that lies beyond the scope of the present work.

Nevertheless, alternative strategies can be developed to adapt the model to *in vivo* data without altering its core structure. In the following section, we introduce a new approach, which we refer to as the **one-to-one connection**.

2.3.5 One to one connection

In the previous section, we aggregated all cortical activity into a single “super neuron”, assuming it could approximate the massive stimulation produced by electrodes in ex vivo experiments. To compensate for the resulting high-frequency input, we reduced the amount of glutamate released per pre-synaptic action potential. This adjustment was guided by the avoidance of NMDA mediated-LTP of post-synaptic weight, during the baseline. The bimodal distribution of retained glutamate release value led to two distinct results. Extremely low value restrict plasticity induction to the LTD window of the eCB pathway. In the other case, the system often entered the LTP window. Due to the strong asymmetry in plasticity gains between LTP and LTD, the dynamics became dominated by LTP, leading to saturation of the post-synaptic weights and rendering further analysis less informative.

In this section, we adopt a different integration scheme. Rather than pooling cortical activity, we define each synapse as a direct match between a single cortical and a single striatal spike train. Since the physiological connectivity between

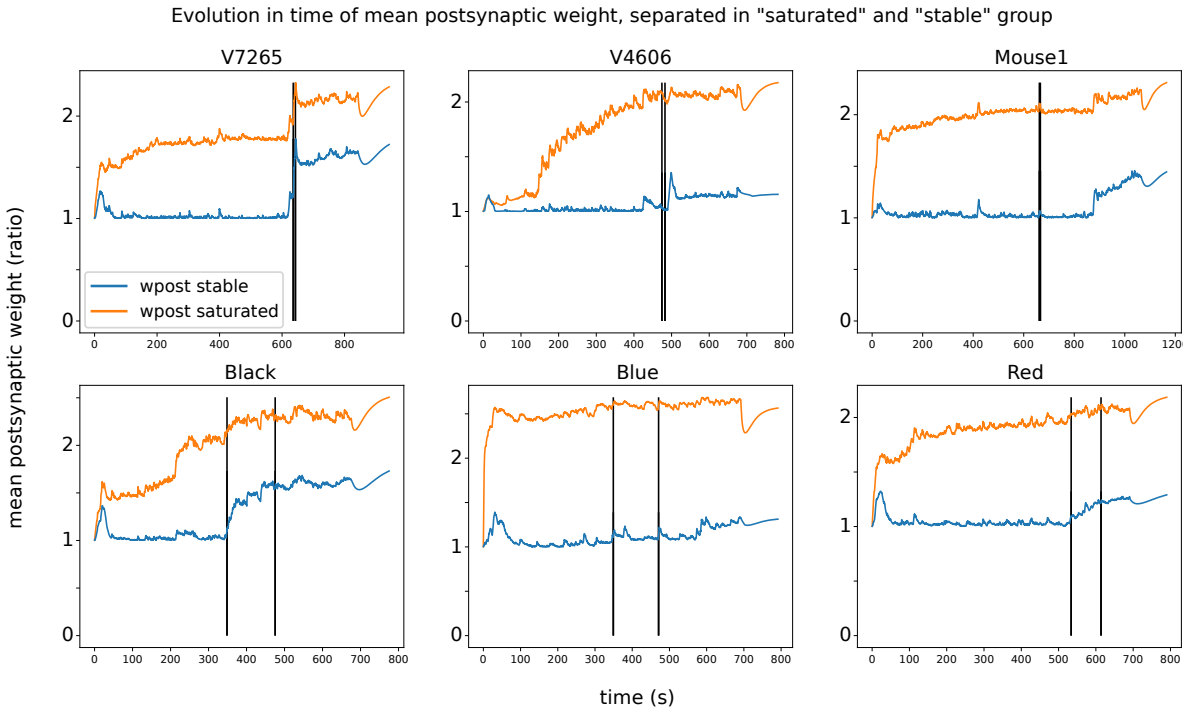


Figure 2.14: Mean post-synaptic weight w_{post} over time for each mouse (V7265, V4606, Mouse1, Black, Blue, Red), computed separately for the two synapse groups: “saturated” (orange line) and “stable” (blue line). Vertical black lines indicate the start and end of the tape contact period.

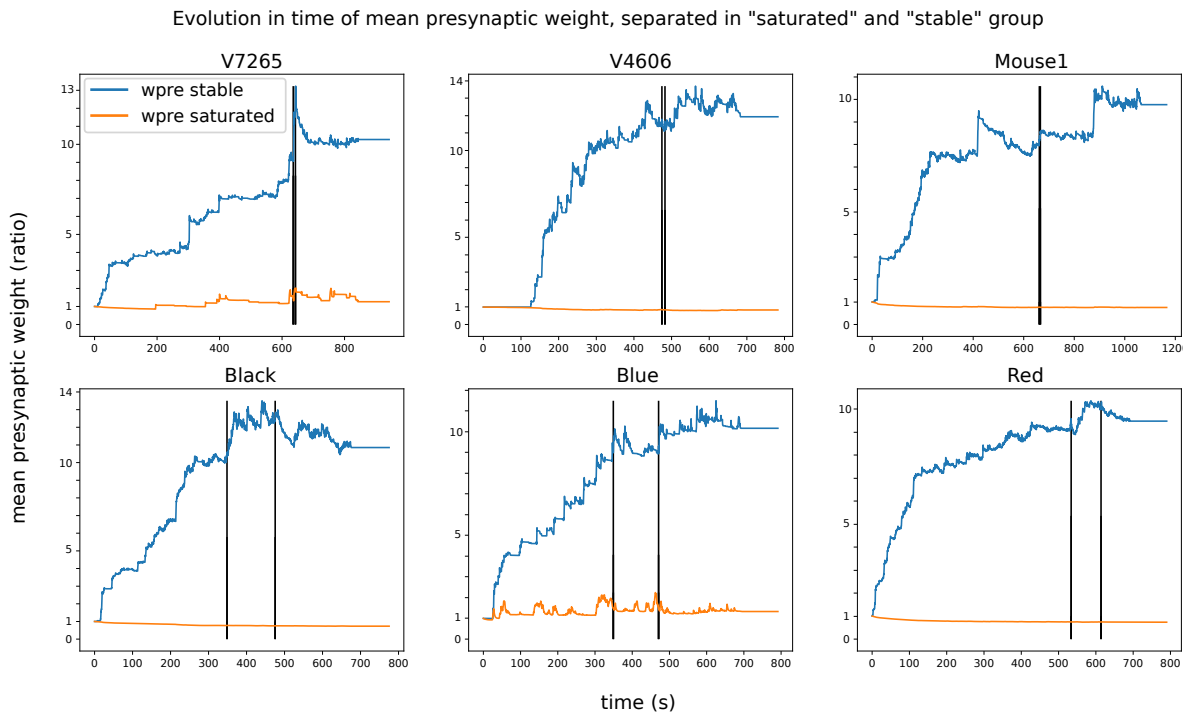


Figure 2.15: Mean pre-synaptic weight w_{pre} over time for each mouse (V7265, V4606, Mouse1, Black, Blue, Red), computed separately for the two synapse groups: “saturated” (orange line) and “stable” (blue line). Vertical black lines indicate the start and end of the tape contact period.

recorded neurons is unknown, we considered all possible pairings, effectively cross-matching every cortical spike train with every striatal one. This one-to-one mapping creates a large set of putative synapses, each of which is treated independently in the simulation framework.

Table 2.3 reports the number of neurons and the total number of computed cortico-striatal pairs for each mouse. Each brain region (cortex and striatum) contained from several dozens to over a hundred recorded neurons, resulting in a few thousand possible synaptic pairs per animal. Note that results from three additional mice are presented here, as new datasets were acquired, processed, and incorporated during the course of this study.

Label	Pre neurons	Post neurons	Computed pairs
V7260	77	111	8547
Mouse1	58	74	4292
V7265	77	51	3927
V4606	98	27	2646
Black	32	96	2451
Blue	32	70	2240
Red	37	148	4512
V4607	38	48	1824
V4609	70	36	2520

Table 2.3: Number of pre- and post-synaptic neurons, and resulting computed synaptic pairs for each mouse. Four first (V7260, Mouse1, V7265, V4606) are short contact mice, five last (Black, Blue, Red, V4607, V4609) are long contact mice.

2.3.5.1 Active pairs definition

The number of possible cortical–striatal pairs is large, and it is unlikely that all simulated pairs correspond to actual anatomical connections. Consequently, some of the synapses we model are the result of unrealistic matches between two spike trains, representing synapses that could not plausibly endure such spike trains. Although the true connectivity at the synaptic level remains unknown, we sought to identify a subset of pairs that are more likely to correspond to functional connections.

In this purpose, we quantified the degree of correlation of each neuron pairs (i, j) during the contact with the sticky tape :

$$C_{i,j} = p_{i,j}/(n_i + n_j)$$

where:

- n_i , n_j are the number of spikes in the train of pre-synaptic neuron i and post-synaptic neuron j respectively, during the first 20 s following the contact time.
- $p_{i,j}$ is the number of pre-post or post-pre spike pairs separated by 200ms or less, during the contact epochs defined as above.

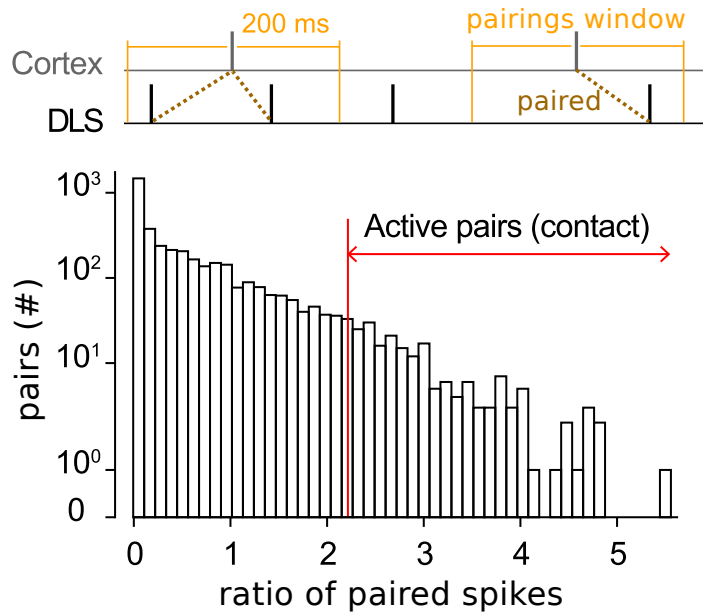


Figure 2.16: **Top.** Schematic of a spike pairing event within a 200 ms time window. Pre-synaptic spikes are taken as reference and draw a time window around them (orange box). Any post-synaptic spikes within this window is considered as "paired" with the pre-synaptic one (dotted line, link "paired" spikes). **Bottom.** Histogram of all $C_{i,j}$ values across neuron pairs. The ratio of paired spikes is defined as $C_{i,j} = p_{i,j}/(n_i + n_j)$, with n_i , n_j the number of spikes in the train of pre-synaptic neuron i and post-synaptic neuron j respectively, during the first 20 s following the contact time and $p_{i,j}$ the number of pre-post or post-pre spike pairs separated by 200 ms or less. The red vertical line indicates the 95th percentile threshold used to define "Active pairs (contact)". From Piette *et al.* 2024 [83]

The neuron pairs (i, j) exhibiting a $C_{i,j}$ within the top 5 percent were labelled as belonging to the "**Active pairs (contact)**" group, see Figure 2.16. In a comprehensive way, $C_{i,j}$ indicates the ratio of spikes that interact within a short temporal window, thereby following Hebbian theory. Such interactions provide a suitable temporal context for STDP mechanisms to occur. These active pairs are assumed to represent stronger candidates for functional connectivity. In subsequent analyses, we will frequently restrict our focus to this subset.

Cumulative distribution function of paired spikes during contact are displayed Fig 2.17. A clear separation in number of paired spikes can be observed, between short contact group (light pink) and long contact group (green).

2.3.5.2 Parameters modification

Even under a simple one-to-one matching scheme, the spiking intensity of striatal neurons remains high and can still lead to NMDA-mediated post-synaptic saturation. To mitigate this effect, we reduced the duration of the depolarization triggered by back-propagating action potentials (bAPs) from 30 ms to 14 ms. Initially, a post-synaptic firing frequency of 16 Hz over a 2-second window was sufficient to induce a transition from the Down to the Up state of the post-synaptic weight. With the shortened bAP duration, this threshold increased to 26 Hz (just above the 25 Hz

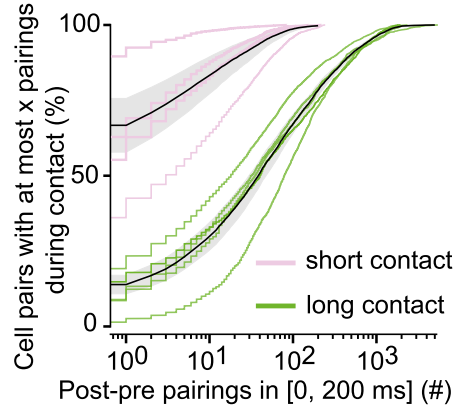


Figure 2.17: Cumulative distribution function for number of spikes during contact and paired spikes during contact. Individual curves are displayed for each mice, separated in short contact (pink) and long contact (green). Standard error of the mean are shown for each group (black curve and grey area).

threshold used for interneuron suspicion), thereby reducing the likelihood of spontaneous or untimely saturation.

Note that the plateau depolarizations should not be regarded as a pure artifact aiming to reproduce those required to induce spike during brain slice stimulation. Similar plateau depolarization have also been observed *in vivo* in striatal medium spiny neurons, where they play a critical role in gating synaptic plasticity [75].

In parallel, we halved the Glu_{max} parameter, reducing it from 2000 to 1000. This adjustment directly impacts calcium influx through ligand-gated channels. As a result, the frequency of isolated pre-synaptic spikes required – over a 2-second window – to trigger eCB-mediated LTP increased from 14 Hz to 21 Hz. These changes allowed for a more selective engagement of plasticity mechanisms and help avoid saturation effect in a larger portion of simulated synapses.

2.3.5.3 Results for NMDA pathway

Figure 2.18 presents, for each mouse, the proportion of synapses exhibiting NMDA saturation over time. Two groups are shown: the full set of computed cortico-striatal pairs, and the previously defined subset of "active pairs". Despite the new one-to-one connectivity approach, saturation of the NMDA pathway remains a major limiting factor for analysis. Across all synapses, between 40% and 80% exhibit saturation, while this proportion exceeds 90% among the active pairs. As a consequence, nearly half of the synapses have already reached the UP state at the time of tape contact, rendering further interpretation of NMDA-dependent plasticity uninformative.

We conclude that the current model, in its original form, would definitely require deep and structural modifications to allow for NMDA-mediated depotentiation, hence be meaningfully applicable to the intensity and duration of Neuropixel recordings. Based on this limitation, we chose to set aside the post-synaptic weight analysis associated with NMDA pathway in the remainder of the study and concentrate our efforts on the pre-synaptic weight associated with the endocannabinoid (eCB) pathway.

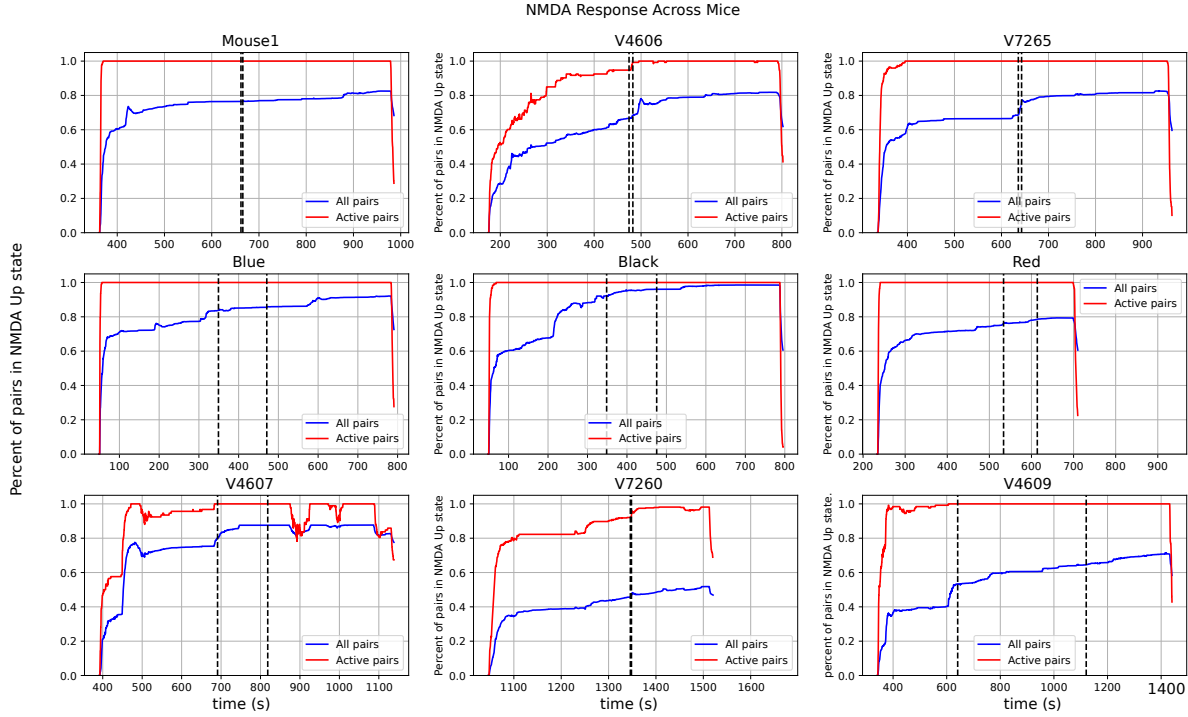


Figure 2.18: Percentage of synapses in the UP state over time, shown for all synaptic pairs (blue) and for the active pairs only (red), for each mouse. Dotted vertical lines indicate the start and end of the contact period.

2.3.5.4 Method for eCB pathway: The plasticitymeter

Here, we take a step back to clarify an important methodological choice. In earlier parts of this work, we occasionally averaged synaptic weights across all cortico-striatal pairs and examined the evolution of the mean synaptic weight over time (Figures 2.14 and 2.15). In the case of the NMDA pathway, the bistable dynamics of post-synaptic weight-mediated by CaMKII phosphorylation—provided a straightforward binary criterion for identifying the occurrence of LTP. This allowed us to quantify, at each time point, the proportion of synapses in which NMDA-dependent LTP had been induced.

For the pre-synaptic weight associated with the eCB pathway, however, the definition of what constitutes LTP turned out to be far less straightforward in the context of our model. We would naturally expect LTP to be reflected by an increase in synaptic weight following the learning task. However, several questions arise: this approach requires defining precise time windows in which to compare a “before” and “after” contact period. The study of the eCB pathway is relatively recent, and the exact temporal cascade and interactions leading from the initiation to the consolidation of memory—starting from synaptic weight changes in sensorimotor regions—are still not well established.

In addition, the pre-synaptic weight trajectories obtained from our simulations (See Fig 2.19) often display strong variability, including during the baseline period. As discussed previously, and as will be discussed again later, the original model was not designed for the high spiking intensity and pattern diversity found in Neuropixel recordings. This raises the possibility that some of the rapid fluctuations in individ-

2.3. Adaptation and Application of the Synaptic Plasticity Model to In Vivo Data: Methods and Results

ual traces could reflect “noise” in the sens of unintended synaptic weight changes, caused by saturation or an “overwhelming” of the model’s dynamics under sustained input, rather than genuine eCB-related plasticity. At the single-synapse level, disentangling such artefactual changes from meaningful plasticity is challenging. Therefore, attempting a categorical classification of whether a pre-synaptic weight display LTP is an uncertain task. We then decided to consider the mean pre-synaptic weight. By averaging across multiple synapses, we increase the likelihood of smoothing noise and revealing the underlying, consistent effects related to the learning task.

Method We previously identified that the strong asymmetry in the synaptic plasticity coefficients from Eq. 2.1 was not well suited for sustained and intense spike trains observed in Neuropixel recordings. While this might reflect a lack of stability or consolidation mechanisms for long-term plasticity in the original model, it does not necessarily imply that the instantaneous dynamics of the pre-synaptic weight—eCB mediated—are inappropriate for *in vivo* data.

To disentangle the issue, we chose to discard the absolute value of the pre-synaptic weight w_{pre} and instead focus solely on its dynamics. From Eq. 2.1, we retained only the binary indicators H_{LTP} and H_{LTD} , and the scaling factor σ . The first two Heaviside functions determine whether the synaptic weight is currently evolving toward LTP or LTD, while σ modulates the speed of these dynamics.

In practice, the dynamics of σ span several orders of magnitude (from ~ 2 up to several millions) and its variations are extremely abrupt. As such, σ effectively acts as a gating mechanism: when its value is high, plasticity is blocked; when low, plasticity is permitted. To simplify interpretation, we binarized σ as follows: it is arbitrarily considered **open** when $\sigma < 100$, and **closed** otherwise.

Combining both the direction of change and the gating mechanism, we defined three distinct plasticity states:

- **LTP dynamic** when $H_{\text{LTP}} = 1$ and σ is open,
- **LTD dynamic** when $H_{\text{LTD}} = 1$ and σ is open,
- **Neutral dynamic** in all other cases.

We then obtained, for each synapse, a three-state temporal profile indicating its ongoing plasticity dynamics: LTP, LTD, or neutral. This representation raises two main questions: (*i*) how to weight LTP and LTD dynamics for comparison, and (*ii*) how to aggregate this information across multiple synapses.

The relative weighting of LTP and LTD dynamics corresponds to choosing the coefficients in Eq. 2.1. Although the precise balance between these two forms of plasticity remains incompletely understood, multiple evidence indicates that the gain of LTP is typically stronger than that of LTD [74, 95]. Additionally, we observed that in our simulations, synapses spent significantly less time in the LTD domain—ranging from 1.5 to 8 times less than in the LTP domain. Given this asymmetry and the central role of LTP in driving effective synaptic change, we chose to focus solely on LTP dynamics as the primary marker of plasticity engagement.

For computational purposes, we discretized time into non-overlapping 200 ms bins and computed, for each bin k , the duration spent in LTP mode. We denote this quantity by $g_{i,j}^k$ for the synapse formed by pre-synaptic cortical neuron i and post-synaptic striatal neuron j .

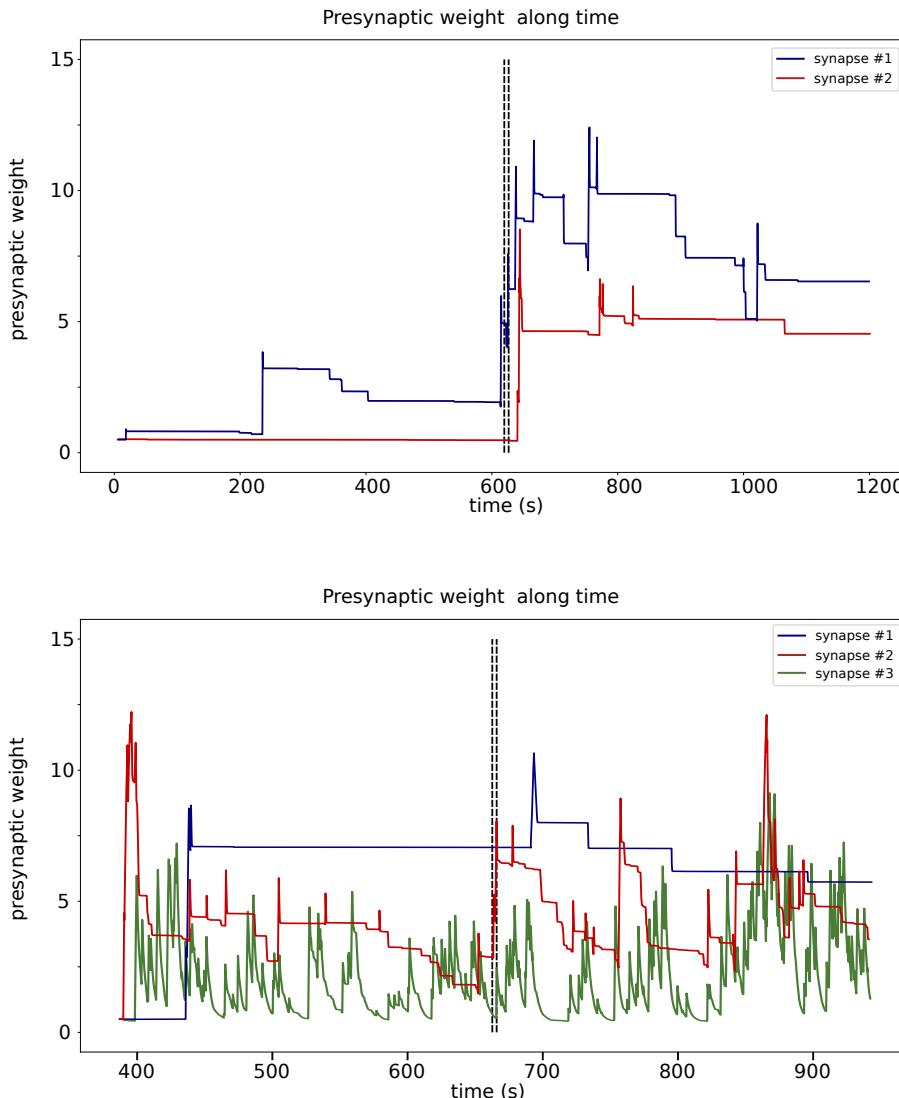


Figure 2.19: Examples of pre-synaptic weight trajectories obtained from the model. **Top.** Two rare examples that could consensually be labeled as LTP: low and stable baseline, followed by a strong and sustained increase during or shortly after contact. **Bottom.** Three more typical examples. Strong fluctuations occur throughout the recording period, making any increase during contact appear random, making sustained increases interpretation difficult.

2.3. Adaptation and Application of the Synaptic Plasticity Model to In Vivo Data: Methods and Results

To combine this information across synapses, we introduced a normalization step. Each synapse's LTP activity vector was normalized by its total LTP engagement across the session, thereby ensuring that each synapse contributed equally to the downstream plasticity profile. This approach avoids biasing the analysis toward highly active synapses and gives greater relative weight to sparse but temporally specific LTP events. Such events are particularly relevant in the context of rapid, one-shot learning, where brief episodes of well-timed plasticity could be disproportionately influential. Biologically, this normalization reflects the hypothesis that weaker synapses—while individually contributing fewer excitatory post-synaptic potentials (EPSPs)—may play a crucial functional role due to their higher plasticity potential or their precise temporal coordination during critical learning periods.

We then define the plasticitymeter of a sub-population A of pairs, as the mean of normalized eCB-LTP engagement over pairs. So that plasticitymeter G of sub-population A at bin k is given by:

$$G_k = \sum_{(i,j) \in A} \frac{g_{i,j}^k}{\sum_k g_{i,j}^k + \epsilon},$$

with ϵ a control parameter which avoid "explosion" of G_k for really sparse eCB engagement. Here, $\epsilon = 1$. We finally use the temporal mean m and standard deviation s of the plasticitymeter values to obtain its **z-score**

$$z_k = \frac{G_k - m}{s}.$$

2.3.5.5 Results for eCB pathway

Active pairs – exhibiting the largest relative increase in correlated activity during contact (Fig 2.16) were associated with high plasticitymeter levels, particularly during behaviorally-relevant states: contact with the sticky tape, active locomotion, grooming and sniffing of the sticky tape (Fig. 2.20). In particular, most eCB-LTP events were concentrated around the contact with the sticky tape in all mice, associated with elevated z-scores (> 2 for all mice in at least 10% of the first 10 seconds after contact onset; also at least three times larger than during baseline). This observation remained consistent when selecting cortico-striatal neuron pairs with a smaller increase in their correlated activity during contact, and even in some mice when taking into account all possible pairs (Fig. 2.21). Overall, the plasticitymeter model shows that the firing patterns of cortical and striatal neurons are compatible with the induction of eCB-LTP during short contacts with the sticky tape.

Z-score provide us insights on "exceptionnal" values. In short contact case, the window of interest is short, and any pike in the z-score value is compatible with the eCB-LTP hypothesis. On the other hand in long contact case, the interpretation of such z-score on a long time window requires to be able to integrate this statistic over time, which remains an unclear process for now.

Yet, to propose a comparison of Plasticitymeter between mice, we looked at the time spent by the z-score during contact, above a certain threshold, that we refer as Plastitime. We found out that despite its natural increased possibily for higher

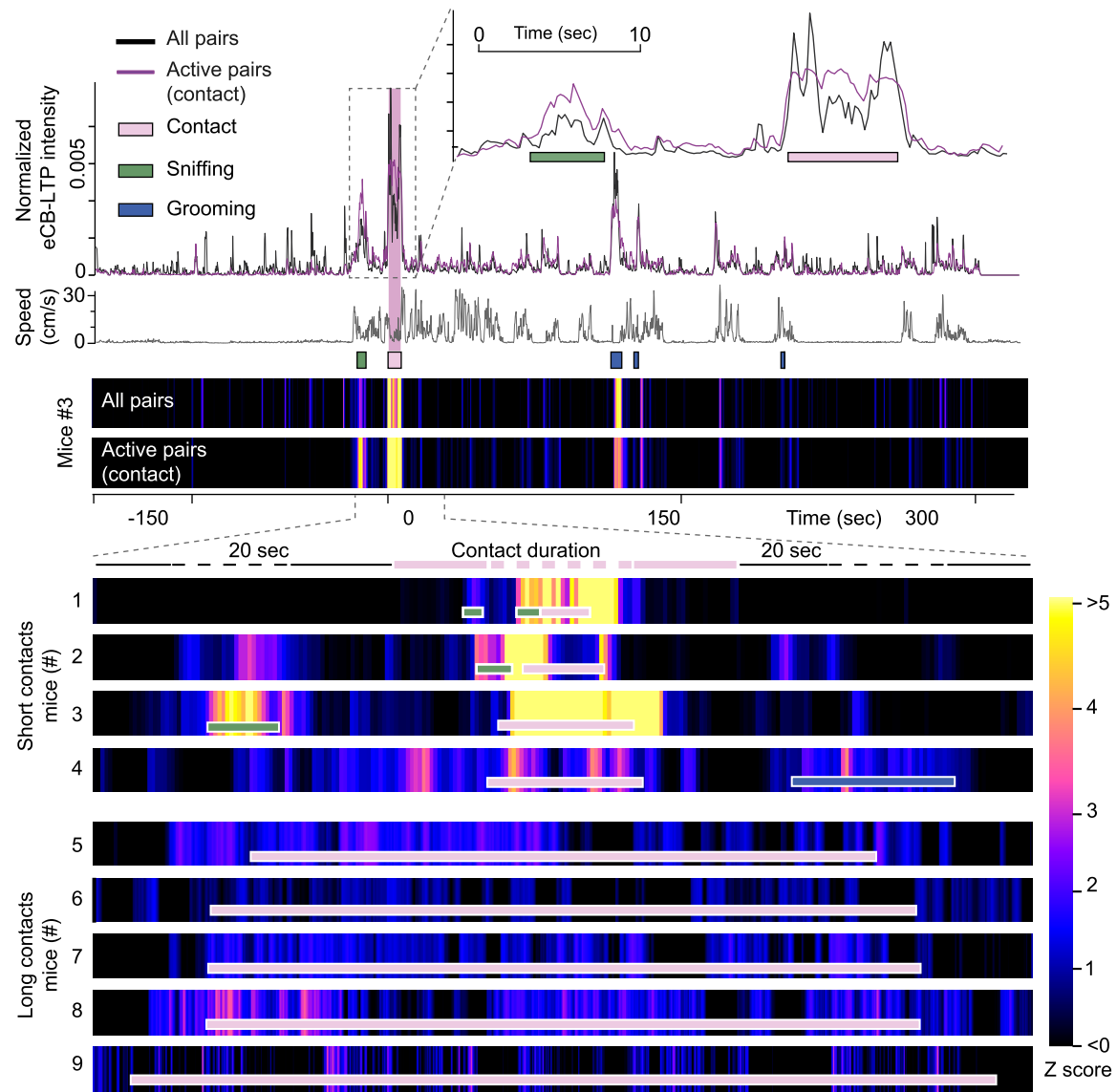


Figure 2.20: Plasticitymeter for a representative mouse (V7265) and behavioral parameters, including mouse instantaneous speed, interactions with the tape or following contact. Plasticitymeter z-scores across all pairs or only active pairs show that the contact with the sticky tape is associated with a significant increase in eCB-LTP induction events (z-score > 2 for every animal at contact time). Z-score maps are aligned to 20 s prior to the start of contact, and displayed up to 20 s posterior to the end of contact.

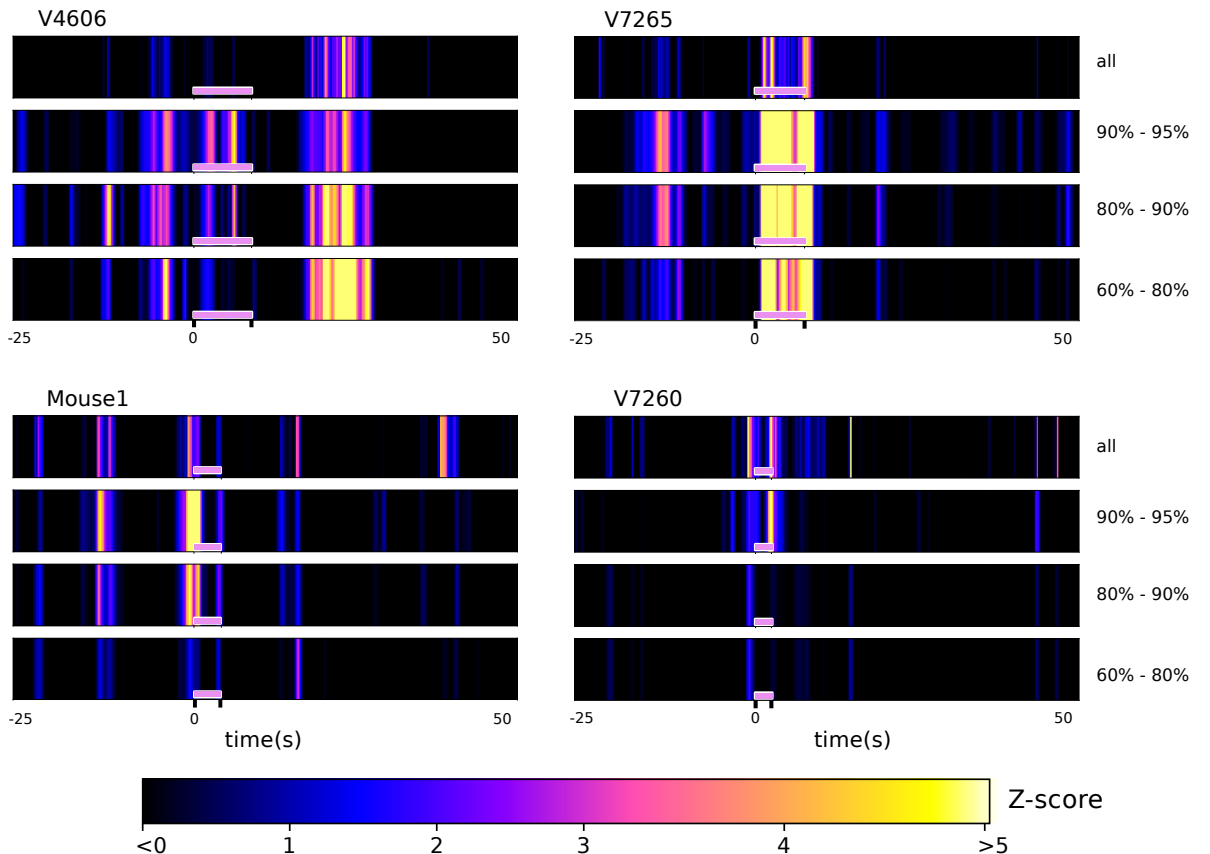


Figure 2.21: Plasticitymeter z-scores across all pairs (top row) or pairs showing elevated correlated activity during contact show that the significant increase in eCB-LTP induction events during contact is robust to the choice of cortico-striatal pairs. The subset of pairs are selected based on the percentage of increase in correlated activity during contact relative to baseline, similarly to the active pairs (corresponding to the 95%-100% range, see main Fig. 3,e c)., Z-score maps are aligned to 25 s prior to the start of contact, and displayed up to 50 s posterior to the start of contact.

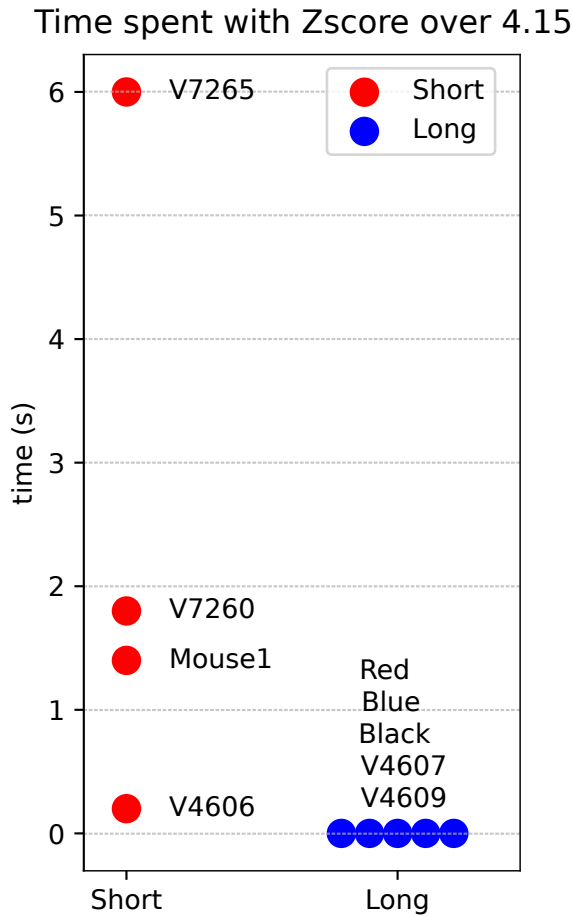


Figure 2.22: Time spent with a plasticitymeter Z-score over 4.15, during contact, separate in short contact group (red dot, left) and long contact group (blue dot, right). Long contact group never pass the threshold, while short contact group stay from 0.2s to 6s for contact during up to 8s.

Plastitime value, long contact group do not exhibit higher value of Plastitime than short contact group. This is particularly visible for a high threshold such as 4.15, which is never crossed by any mouse from the long-contact group, whereas it ranges from 0.2s to 6s in the short-contact group, whose contact durations are up to 8s (Fig. 2.22).

As discussed previously, the separation between short- and long-contact groups was motivated by the hypothesis that the two conditions correspond to qualitatively distinct forms of learning. While the long-contact group more closely resembles a classical incremental learning paradigm, the short-contact group represents a genuine one-shot learning situation. The marked divergence in Plastitime between the two groups strongly supports the view that eCB-LTP constitutes the specific substrate of one-shot learning. From this perspective, one would predict that blocking the eCB pathway should impair learning in mice subjected to short contact durations.

Experiments conducted by Venance's team provide strong support for this prediction. In the sticky tape avoidance (STA) protocol, they used genetically modified

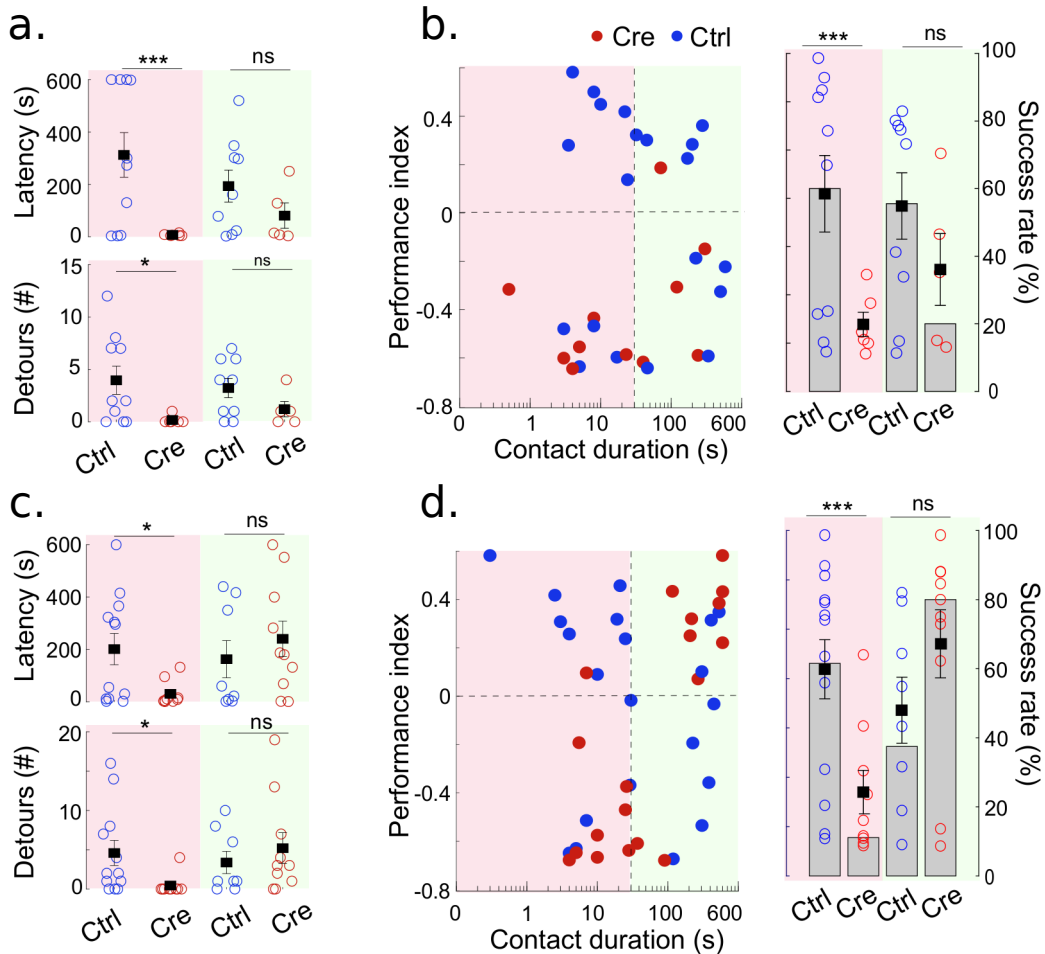


Figure 2.23: **a,c.** Latency-to-contact and detours. Two-sample Welch-test (for short contact duration, <30 seconds, because of unequal variance) and t-test (long contact duration >30 seconds). **b,d.** Avoidance index (circles) and avoiders (bars) are low in Cre mice for short contact duration, but remain high for long contact duration. Two-sample Welch and t-test, Chi-squared test.

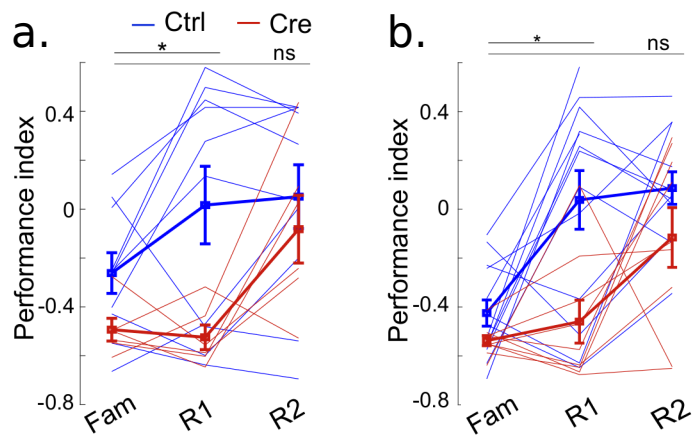


Figure 2.24: **a,b.** Time courses of avoidance index at familiarization, retrieval-1 and -2 sessions for short contact duration mice. Linear Mixed Models.

mice with targeted knockouts of either CB1 or D2 receptors. D2R has been identified as a necessary afferent for eCB-LTP induction [43], whereas CB1R is the primary pre-synaptic receptor mediating endocannabinoid signaling [19]. As expected, *ex vivo* patch-clamp recordings under a classical STDP protocol (15 pairings at 1 Hz) revealed a loss of LTP in knockout preparations.

To link these synaptic impairments with behavior, the team assessed learning performance during the STA task. Strikingly, in the short-contact group, control animals performed significantly better than CB1R- and D2R-knockouts (see Fig. 2.23, left red side of each panels). In contrast, in the long-contact group, CB1R- and D2R-knockout and control mice exhibited similar performance levels (see Fig. 2.23, right green side of each panels).

Taken together, these findings provide us with an experimental confirmation of the model prediction that the eCB-LTP is a substrate for one-shot learning.

To go further, performance was also evaluated by Venance's team during a second retrieval session conducted 24 h later. Interestingly, although the short-contact knock-out group initially performed worse than controls at the first retrieval, their performance caught up by the second retrieval (Fig. 2.24). At this stage, repeated exposure to the sticky tape effectively transformed the task from a one-shot to a more incremental learning paradigm. This behavioral observation suggests that eCB-LTP is specifically required for the rapid, one-shot acquisition of memory, but is dispensable once learning can proceed through repeated experiences. In such incremental regimes, other plasticity mechanisms – such as NMDA receptor-dependent pathways – are likely to take over.

2.4 Additional Exploratory Directions

2.4.1 Using LFP information

Local Field Potentials (LFPs) reflect the summed extracellular voltage fluctuations generated primarily by transmembrane currents in nearby neurons, especially synaptic currents, but also contributions from spikes, voltage- and ligand-gated channels, and intrinsic membrane oscillations [13]. Although influenced by spiking activity, LFPs also integrate substantial subthreshold synaptic activity and membrane oscillations and thus cannot be considered a simple proxy for action potential rates.

In the cortex, the laminar structure and spatial organization of inputs make LFPs relatively interpretable in terms of local network dynamics [28]. In contrast, the dorsal lateral striatum (DLS) presents a markedly different microcircuit: most neurons are medium spiny neurons (MSNs) with small, radially distributed dendritic trees, and there is no layered organization of inputs. Several studies have shown that striatal LFPs can be strongly contaminated by signals from other brain regions, and may not faithfully reflect local cellular activity [54, 105]. This makes the direct interpretation of LFP amplitude in terms of local excitatory drive highly uncertain.

Nevertheless, we tried a simple and exploratory approach in which we used LTP amplitude as a proxy for the glutamate release. The instantaneous Glu_{\max} value was modulated linearly by the LFP amplitude: higher LFP values resulted in proportionally higher Glu_{\max} . This naive implementation did not produce variations in the

simulations leading to interpretable and biologically meaningful way. We therefore discontinued this direction.

2.4.2 On neuron and synaptic specialization

During this work, we recurrently faced a major difficulty: the strong mismatch in the statistical properties of spike trains between *ex vivo* experiments and Neuropixel recordings, which regularly challenged the reliability of the model under such *in vivo* conditions.

To address this, we explored a retrospective approach aiming to sort and extract the most meaningful plasticity-related information. Starting from the Plasticitymeter output — representing, for each synapse, the temporal distribution of LTP recruitment via the eCB pathway —, we applied time-series clustering to identify distinct functional subgroups of synapses. For this, we used the K-means method for time series from the `tslearn` package [104]. Note that, as with most K-means implementations, the clustering is not fully deterministic since it depends on random initialization.

Remarkably, synapses were consistently separated into two groups with highly interpretable biological significance. The first group, which we term **Motor**, showed a strong correlation with the animal’s motion speed (Pearson correlation $r = 0.65$). The second group, referred to as **Learning**, displayed narrow activation windows, most often coinciding with behaviors directly related to the task: sniffing the sticky tape, contact periods, or grooming behavior. Interestingly, the mean firing rates of the two subgroups were indistinguishable. This is not unexpected, as the model can reproduce classical STDP paradigms where precise spike timing, rather than mean rate, drives plasticity. However, this result provides direct evidence that, despite the overwhelming *in vivo* firing activity, the model is not purely rate-driven but is sensitive to more subtle, time-dependent spike interactions.

Note that K-means is an unsupervised method: the two groups ”motor” and ”learning” emerged naturally from the clustering procedure in a single animal. Such clearly separated functional subgroups of synapses did not appear in other mice recordings. However, we believe that applying more guided clustering approaches, could yield similar functional separations.

This preliminary result on synapse specialization related to learning behavior has given rise to a poster presentation at the Bernstein Conference 2024.

2.5 Python Package: Synacomp

The analyses presented throughout this work required extensive computational processing, including data management, model implementation and optimisation, simulation scheduling, and post-processing of results. Over time, this led to several hundred lines of Python code where I developed many new skills.

Guided and supervised by Jan-Michael Rye, our team’s research engineer in charge of code quality, this effort matured into a dedicated Python package: **Synacomp**. The aim of **Synacomp** is to provide a modular, reproducible tool to implement our full analysis pipeline—from spike-sorted data to final Plasticitymeter Z-score plots.

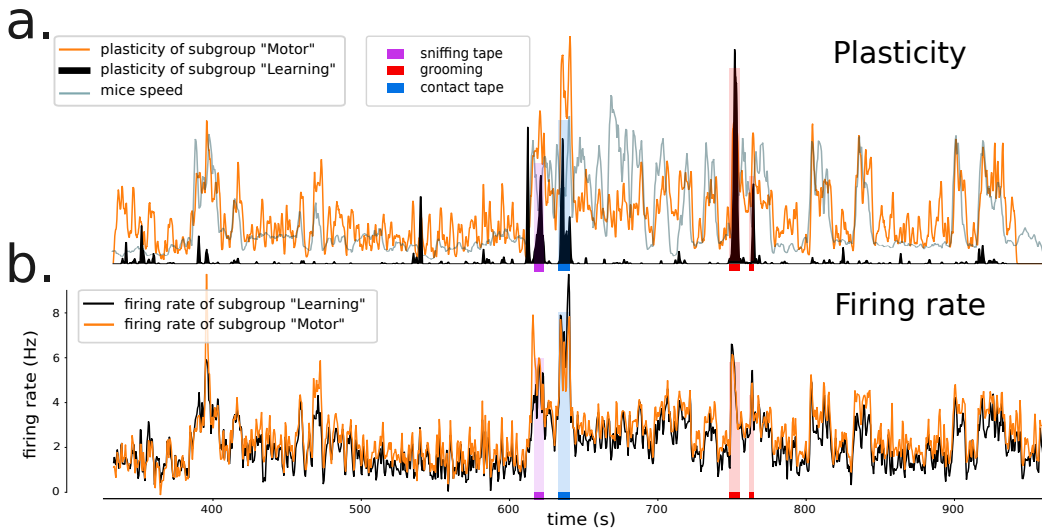


Figure 2.25: **a.** Clustering of synapses based on the temporal profile of eCB-mediated LTP recruitment (plasticitymeter output). Two groups emerged: Motor (orange) correlating with locomotor speed, and Learning (black) with activation during task-relevant behavioral events. **b.** Mean firing rate for each group (Learning and Motor). While their plasticitymeter values differ strongly, their mean firing rates are almost identical.

This tool is valuable for our collaborators from the Venance team, and is designed to be reused in future experiments with similar computational needs.

One of the strengths of Synacomp is its modular architecture (Fig. 2.26). It is built around two main classes:

- **Mouse class** – Handles all data associated with a single animal. This includes file paths to spike-sorted recordings, but also a flexible event system. Events are stored as lists of ranges, allowing annotation of relevant behavioural episodes (e.g., grooming, sniffing, contact with the sticky tape) as well as technical information (e.g., extraction windows relative to the recording).
- **Model class** – Implements a synaptic plasticity model (currently the Cui et al., 2016 model) that can operate directly on data from a `Mouse` object. Model selection and mouse assignments are defined via a YAML configuration file (Fig. 2.27 and Fig. 2.28).

Running a complete analysis is straightforward: the command `synacomp-compute` reads the configuration file, executes the selected model on all specified mice, and manages results via the Hydronaut library—a combination of MLflow and Hydra—ensuring parameter traceability and standardised result storage.

Once a simulation is completed and stored under an automatically generated run ID, the associated `Model` class provides a dedicated post-processing routine to process and aggregate results across the listed mice.

Efficiency Attention was brought to computational efficiency. We made use of vectorization, which allow us to use numba library [55]. This library can make part of python code approach the speed of C. In the analysis function, we also used sparse

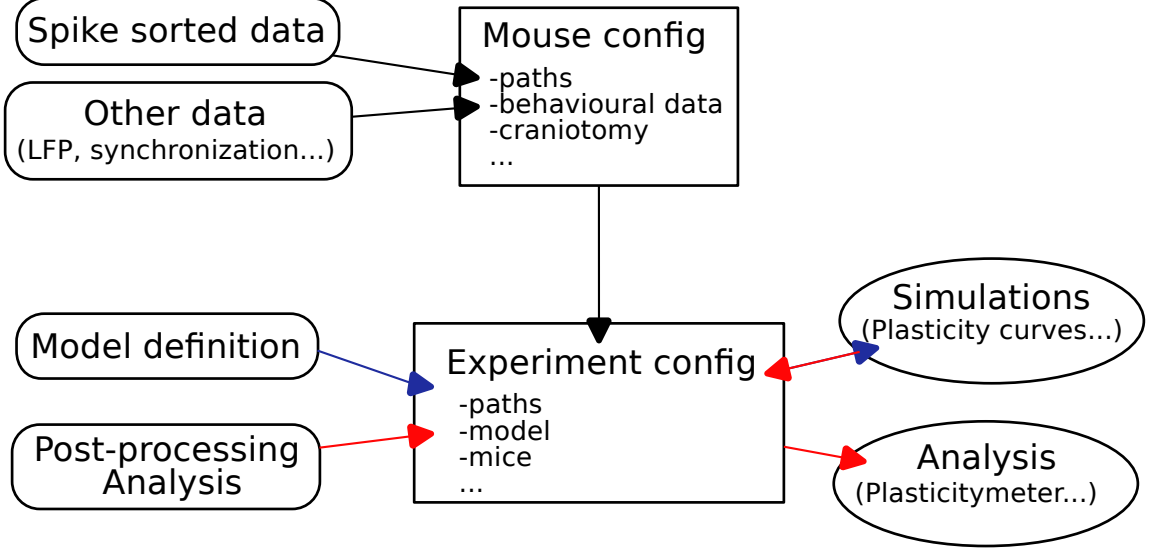


Figure 2.26: Schematic overview of the `Synacomp` package architecture, showing modular interaction between Mouse objects, Model definition, and the configuration system.

format for both memory save and built our function around it to get better speed. For process like working on cross ISI, our approach is faster in order 100 to 1000 compared to a naive implementation with for loop and save of full cross ISI matrix.

Attention was devoted to computational efficiency. We relied extensively on vectorization and employed the `numba` library [55], which allows portions of Python code to reach execution speeds close to those of C. In addition, several analysis functions were implemented using sparse data structures, both to reduce memory requirements and to accelerate computations. For instance, in processes such as cross-interspike-interval (cross-ISI) analysis, our sparse-based implementation proved to be between faster by 2 to 3 orders of magnitude compared to a naive implementation relying on for-loops and storage of full cross-ISI matrices.

Availability The full `Synacomp` package is available at: <https://gitlab.inria.fr/aistrosight/synacomp>, and keeps being update.

2.6 Conclusion

Keypoints

- Multiple findings suggest that one-shot learning is mediated by the endocannabinoid pathway in cortico-striatal projections. Simulations with the model of Cui *et al.* (2016) [21] predict a marked recruitment of eCB-LTP in the DLS during tape contact, but only when the contact duration is short (<8 s). Consistently, experimental data show that mice with impaired eCB signaling (via CB1 or D2 receptor knock-out) perform worse in the STA task than control animals.

- **The endocannabinoid pathway is not required for other learning paradigms.** In long-contact conditions (>60 s), knock-out mice exhibit similar performance to controls. Moreover, mice with impaired eCB signaling that failed to learn at the first retrieval, succeeded upon re-exposure. This indicates that incremental learning can proceed via alternative mechanisms, likely NMDA-dependent.
- **Preliminary evidence suggests functional specialization of eCB-dependent synapses.** In one subject, clustering analysis revealed two distinct groups of synapses: one whose eCB-LTP dynamics correlated with learning-related behaviors (e.g., tape contact, grooming), and another correlated with locomotion speed. Notably, these differences could not be explained by average firing rate alone, underscoring the time-dependent and pathway-specific contribution of eCB plasticity.

Altogether, this chapter reinforces the view that the dorsolateral striatum (DLS) is capable of supporting both incremental and one-shot learning, depending on activity patterns and ultimately pathways recruited.

Discussion

Beyond the specific conclusions on one-shot-learning and eCB-plasticity, this work highlights the challenges of generalizing mechanistic models in order to bridge multiple data sets and experimental observations within a unified framework.

Our first major difficulty appeared when realizing that the model from Cui et al. (2016) did not easily allow for NMDA depotentiation. Indeed, a return from UP to DOWN could only occur through very specific transient dynamics. This limitation originates in the fact that the model was calibrated exclusively on *ex vivo* slice data, where such transitions were not observed. This raises an important open question: could an alternative set of parameters both fit the original slice data and allow for NMDA depotentiation, or would a modification of the model's core mechanisms be required? During my thesis, this problematic was set aside, since our work concentrated on the implication of eCB pathway in one-shot-learning. However, I hope to have the chance to address those questions in the future. The more a mechanistic model can reproduce diverse experimental conditions, the more it can constrain underlying biological constants and improve its explanatory power.

There are three primary modifications that I would like to bring to the model. The first concerns the glutamate release, which for now is very simplified. Introducing a more precise description of vesicle pool dynamics, together with an uptake mechanism, could strongly impact calcium signaling and all downstream pathways. Such an extension could call for the implementation of a tripartite synapse, incorporating astrocytes.

The second one is the refinement of pre-synaptic mechanisms following CB1R activation. In its current form, the model relies primarily on phenomenological descriptions of CB1R-mediated effects. However, recent literature continues to uncover detailed molecular and cellular processes associated with CB1R signaling [58,68,111]. Incorporating these advances would allow for a more mechanistic representation of

the pre-synaptic pathway, thereby improving both the explanatory power and predictive capacity of the model. Yet, how these mechanisms contribute to eCB-LTP, and whether they apply to cortico-striatal synapses, is still to determine.

Finally, third one is an enhanced study of TRPV1 channel. This channel was identified as required for eCB-LTP [19]. However, despite its representation in the model, its presence is not required for eCB-LTP during simulations. Adding the presence of TRPV1 as a necessity for eCB-LTP could provide other parameters set, or highlight other key mechanisms that should be rework.

The big gap between *ex vivo* and *in vivo* is strongly related with our need for the "plasticitymeter" analysis introduced during this chapter (see Sec 2.3.5.4). While our pipeline successfully highlighted an over-recruitment of the eCB pathway during short-contact trials, this conclusion still depends on several preprocessing and normalization steps aimed at isolating the most relevant signals. A more generalized mechanistic model, validated against a variety of data sources, would ideally allow for a more direct interpretation of simulation results. However, obtaining such ground truth directly from Neuropixel-scale recordings is technically out of reach with current methods. This limitation is precisely what makes mechanistic modeling a valuable tool: it provides access to otherwise unobservable variables, offering the only current window into synaptic plasticity dynamics during *in vivo* learning.

All these points required an extensive amount of simulations. Data integration was modified several times, we played with parameters to explore model's reaction, and for each mouse we ran up to thousands of simulations each time. Such a workload necessitated a robust computational framework that could guarantee efficiency, reproducibility, modularity, and extensibility.

To address this, I developed **Synacomp**, under the supervision of our team engineer Jan-Michael Rye. This package was designed not only to support the present work, but also to serve as a methodological tool for future analysis, that want to continue to develop. It enables user-friendly execution of large-scale simulations, while providing a flexible structure to incorporate additional models of synaptic plasticity and compare their predictions. Given the richness of Neuropixel data, we believe that such a framework is particularly valuable for extracting biologically meaningful insights in a reproducible and systematic way.

<code>experiment:</code>	Provide a name and description to the experiment
<code>params:</code>	Default directories. Can be specified to manage yourself your data organization.
<code>model:</code>	Specify the model that should be used for simulations and define its key parameters.
<code>mouse_ids:</code>	Invoke on which data you should apply the model
<code>post_processing:</code>	You can specify ids of already proceed simulations and only run post-process.
<code>system:</code>	You have control over computational parameters, as number of CPU used for parallel computation.

Figure 2.27: Example of a YAML configuration file defining model parameters and mouse assignments for a Synacomp experiment.

<code>identifier: V7265</code>	Id used to identify the mouse
<code>paths:</code>	Paths where to find the corresponding data
<code>events:</code>	
<code>grooming:</code>	
<code>- start: 751.0</code>	
<code>- stop: 756.8</code>	
<code>- start: 764.5</code>	
<code>- stop: 765.5</code>	
<code>sniffing:</code>	
<code>- start: 619.78</code>	
<code>- stop: 624.5</code>	
<code>contact:</code>	
<code>- start: 635.8</code>	
<code>- stop: 642.75</code>	
<code>time_extracted:</code>	
<code>- start: 700</code>	
<code>- stop: 1800</code>	
<code>regions:</code>	
<code>striatum:</code>	
<code> first: 0</code>	
<code> last: 180</code>	
<code>cortex:</code>	
<code> first : 200</code>	
<code> last: 380</code>	

Figure 2.28: Example of a YAML configuration file defining a Mouse object, including data paths and annotated event ranges.

Chapter 3

Reconstructing Large-Scale Heterogeneous Quadratic-Integrate-and-Fire Networks Using Their Dominant Modes.

*Le macrocosme et le microcosme
sont construits exactement sur le
même modèle.*

Swami Vivekananda

3.1 Introduction

In the previous chapter, we investigated synaptic-level mechanisms of one-shot learning, emphasizing the role of endocannabinoid (eCB) signaling in enabling bidirectional plasticity. Notably, eCB pathway was shown to mediate long-term potentiation (LTP) with very few spike pairings, identifying this mechanism as a proved supported candidate for the engram of fast learning.

We now shift our focus to the network level, where we seek to understand how eCB-dependent plasticity affects global neural dynamics. Specifically, we ask how eCB-mediated synaptic plasticity shapes the collective behavior of neural populations in a fast learning regime? Can such plasticity rule also lead to analogous potentiation at the population level?

To address these questions, we adopt a mean-field approach, leveraging the analytical tractability of the Lorentzian ansatz framework introduced by Montbrió, Pazó, and Roxin (2015) [69]. This model, derived from networks of Quadratic Integrate-and-Fire (QIF) neurons, offers an exact low-dimensional description of macroscopic activity in terms of mean firing rate and membrane potential. Its strength lies in its analytical solvability, which makes it well-suited for systematically exploring how microscopic plasticity rules impact emergent population-level phenomena.

Before incorporating biologically inspired plasticity mechanisms such as those mediated by endocannabinoid (eCB) signaling an essential methodological step is required: extending the Lorentzian mean-field formalism to allow heterogeneity in synaptic weights. Classical formulations typically rely on either homogeneous coupling or sparse connectivity, which limits their ability to represent realistic, structured networks. In contrast, biological neural circuits display pronounced diversity in synaptic weights, which may critically influence their dynamical properties and capacity for learning [56, 63].

In the following chapter, we present a new method that Hugues Berry and I published at the *International Conference on Computational and Mathematical Neuroscience*. We build upon the Lorentzian mean-field framework, which reduces a fully connected QIF network with homogeneous synaptic weights to a system of two population-level equations. We introduce heterogeneity by coupling multiple such populations, each described by its own pair of mean-field variables. This construction allows us to represent structured networks while preserving the exactness of the underlying mean-field reduction.

This extension constitutes a necessary step toward embedding biologically realistic plasticity mechanisms. However, as the number of coupled populations increases, the dimensionality of the resulting system grows accordingly, which counteracts the original goal of mean-field reduction by limiting analytical tractability.

To overcome this limitation, we introduce an additional reduction step based on dominant eigenmode techniques. This approach consists of a change of basis guided by the spectral properties of the connectivity matrix. Originally developed in other fields such as electrodynamics, eigenmode decompositions have proven effective in capturing the essential dynamics of high-dimensional systems. In a neuroscience context, they have shown to provide meaningful low-dimensional representations of structured brain activity [87, 108]. Here, we demonstrate that retaining only a small number of dominant eigenmodes is sufficient to accurately reproduce the behavior of the full heterogeneous network.

3.2 From Global to Pairwise Synaptic Heterogeneity

Montbrió, Pazó, and Roxin originally addressed the lack of heterogeneity by considering a distribution over the synaptic weights J , so the input of neuron j reads:

$$I_j(t) = \eta_j + J_j s(t) + I(t). \quad (3.1)$$

with

- η_j , the synaptic excitability,
- $s(t)$, the mean synaptic activation. In this case, for an infinitely fast synapse, it is equal to the mean firing rate $r(t)$.
- $I(t)$ an external current, shared by all neurons.

Following the Lorentzian Ansatz, the distribution of membrane potential now depends on the synaptic weight J :

$$\rho(V|\eta, J, t) = \frac{1}{\pi} \frac{x(\eta, J, t)}{(V - y(\eta, J, t))^2 + x((\eta, J, t)^2)}. \quad (3.2)$$

If the synaptic weights J are drawn independently from a Lorentzian distribution centered at \bar{J} with half-width Γ , and are uncorrelated with the η , they showed that the mean-field reduction remains analytically tractable. The resulting macroscopic system reads:

$$\begin{cases} \frac{dr}{dt} = \frac{\Delta}{\pi} + \Gamma \frac{r}{\pi} + 2 r v, \\ \frac{dv}{dt} = v^2 - \pi^2 r^2 + \bar{J} r + \bar{\eta} + I(t) \end{cases} \quad (3.3)$$

However, in this formulation, each post-synaptic neurons share the same synaptic weight with the entire presynaptic population. This global heterogeneity, while useful analytically, does not capture the level of specificity required to represent biological mechanisms such as the eCB-induced LTP, where precise pre- and post-synaptic spike timing is essential at the individual synapse level. In contrast, the form of heterogeneity relevant to our study is pairwise, or one-to-one, in nature, where each synaptic weight $J_{i,j}$ depends explicitly on both the presynaptic neuron i and the postsynaptic neuron j . In this formulation, the input current to neuron j becomes:

$$I_j = \eta_j + \frac{1}{N} \sum_{i=1}^N J_{i,j} r_i + I(t), \quad (3.4)$$

where $J_{i,j}$ denotes the synaptic weight from neuron i to neuron j .

This dependence of $J_{i,j}$ on both pre- and post-synaptic indices introduces a fundamental challenge to macroscopic mean-field reductions. Previous reductions, such as those derived by Montbrió, Pazó, and Roxin, rely critically on the ability to factor the recurrent input into a population-averaged term. In their formulation, the mean membrane potential follows:

$$\frac{dv}{dt}(\eta, J) = v^2 \underbrace{-\pi^2 r^2 + J s}_{\text{recurrent term}} + I(t) \quad (3.5)$$

To close the system, authors remark that $s(t) = r(t)$ (see Sec 1.3, Infinitely fast synapses). It is made possible by assuming that synaptic coupling J could be factorized over the recurrent term. Assuming a Lorentzian distribution for η and J , they are finally able to formally compute the average over the whole network and provide an exact analytical reduction.

However, when $J_{i,j}$ varies across both indices, the mean synaptic activation can no longer be expressed only as a function of the mean firing rate. The firing rate r_i of each individual neuron must be explicitly retained. In practice, this adds significant complexity to the relationship between synaptic input and overall network dynamics. As we will come back to that later, we now denote s_j , the synaptic activation of neuron j , as the recurrent part of the input current.

$$s_j = \frac{1}{N} \sum_i J_{i,j} r_i,$$

where the synaptic weight $J_{i,j}$ cannot be factored out and is included into the synaptic activation expression.

This formulation reflects the microscopic specificity of biological synaptic connections, but complicates any attempt at analytical simplification or reduction to low-dimensional dynamics. The explicit neuron-to-neuron heterogeneity embedded in the connectivity matrix $J_{i,j}$ breaks the symmetry that allowed earlier reductions. In the continuous formulation, the resulting integro-differential formulation intrinsically encodes this pairwise heterogeneity and prevents straightforward analytical treatment. The possibility of deriving a closed-form, low-dimensional description of the network dynamics seems severely limited.

This modeling gap is biologically motivated and addresses the need for more realistic mean-field approaches. Numerous experimental studies have demonstrated that synaptic strengths are not uniform across postsynaptic targets, even when originating from a common presynaptic neuron. Instead, synaptic efficacies exhibit a high degree of variability, shaped by a combination of factors including pre- and postsynaptic activity history, dendritic location, and neuromodulatory context [18, 56, 64].

Furthermore, spike-timing-dependent plasticity (STDP) mechanisms—such as those mediated by endocannabinoids require precise pre-post interactions at the level of individual synapses [19, 21], reinforcing the relevance of modeling fine-grained, pair-specific connectivity.

In the following, we formalize a network representation that explicitly incorporates this one-to-one synaptic heterogeneity, and investigate how the Lorentzian ansatz may be adapted or extended to capture the resulting dynamics.

3.3 Introducing Heterogeneity

We introduce an additional structural index $z = 1 \dots, M$, for which Sys 1.29 is now defined for each z :

$$\frac{dr_z}{dt} = \frac{\Delta}{\pi} + 2 r_z v_z, \quad (3.6)$$

$$\frac{dv_z}{dt} = \bar{\eta} + I(t) + v_z^2 - \pi^2 r_z^2 + s_z. \quad (3.7)$$

with

$$s_z(t) = \frac{1}{M} \sum_{w=1}^M J_{wz} r_w(t). \quad (3.8)$$

In this formulation, the QIF network is organized in M distinct populations (or layers). Then J_{wz} is the synaptic strength from population w to population z . Each population follows the MPR formalism and is described by its MPR mean-field variables (r_z, v_z) . The core difference with Sys 1.29 is encapsulated in the term $s_z(t)$ from Eq 3.8. This term is a coupling between the different populations, with a one-to-one connectivity strength. When $J_{wz} = J_C$ is constant for all z and w , it can be factored out of the sum, resulting in the emergence of the mean firing rate $J_C \bar{r}$. This is an essential step to close the system (Eq 3.6, Eq 3.7). However, as this is no longer possible with heterogeneous synaptic strength, $s_z(t)$ has to be fully explicated in our case.

The resulting system has dimensionality $2M$. For large M , this quickly becomes analytically intractable and the computational cost of numerical simulations scales quadratically with the number of populations. This motivates the need for an efficient reduction method that preserves the essential dynamics of the network.

3.4 Modal Decomposition

We introduce a change of basis based on the eigendecomposition of the square coupling matrix J . The new dimensions are called modes. Let T be the square matrix whose columns are the normalized eigenvectors of J . Assuming J is symmetric, we define the projection of any vector $x \in \mathbb{R}^M$ in this basis as:

$$\tilde{x} = T^\top x. \quad (3.9)$$

$$\tilde{J} = T^\top JT, \quad (3.10)$$

is then a diagonal matrix with the eigenvalues of J on the diagonal.

In vector notation, the synaptic input term Eq 3.8 becomes:

$$\tilde{s}(t) = \tilde{J} \tilde{r}(t) = (\lambda_z r_z)_z. \quad (3.11)$$

where λ_z denotes the eigenvalue associated with the z -th mode.

In this new basis, the synaptic inputs which is composed of linearly coupling terms across populations (Eq 3.8), are fully decoupled across modes (Eq 3.11). While this population interactions are decoupled, modes coupling are introduced in the nonlinear terms r_z^2 and v_z^2 .

To make this explicit, we rewrite Eq 3.6 and Eq 3.7 in the modal basis. Using $\tilde{r} = T^\top r$ and $\tilde{v} = T^\top v$, we obtain:

$$\frac{d\tilde{r}_z}{dt} = \frac{\Delta}{\pi} U_z + 2 \sum_{w,k,\ell=0}^{M-1} C_{zwk\ell} \tilde{r}_k \tilde{v}_\ell \quad (3.12)$$

$$\frac{d\tilde{v}_z}{dt} = (\bar{\eta} + I(t)) U_z + \sum_{w,k,\ell=0}^{M-1} C_{zwk\ell} (\tilde{v}_k \tilde{v}_\ell - \pi^2 \tilde{r}_k \tilde{r}_\ell) + \lambda_z \tilde{r}_z, \quad (3.13)$$

where

$$U_z = \sum_{w=0}^{M-1} T_{wz},$$

$$C_{zwk\ell} = T_{wz} T_{wk} T_{w\ell},$$

For most connectivity matrices J , the dominant dynamical components are associated with the eigenmodes corresponding to the largest eigenvalues. By truncating the modal description to these dominant modes only, the full network dynamics can often be reconstructed with high accuracy.

Special case: Circulant matrix

When J is a circulant matrix, (i.e., when connectivity depends solely on the distance between populations arranged on a ring topology), explicit expressions are known for both eigenvalues and eigenvectors. For $z = 0, 1, \dots, M - 1$, the z -th eigenvalue is the complex number:

$$\lambda_z = \sum_{w=0}^{M-1} J_{0w} (\omega_M)^{wz}, \quad \omega_M = e^{-2\pi i/M}.$$

with associated eigenvector:

$$v^{(z)} = \begin{pmatrix} 1 \\ \omega_M^z \\ \omega_M^{2z} \\ \vdots \\ \omega_M^{(M-1)z} \end{pmatrix}.$$

For this special case, the modal basis corresponds to the discrete Fourier basis. For any M , the first mode is always the same: $v_k^{(0)} = 1, \forall k = 1, \dots, M$. Hence, $\tilde{r}_0 = \frac{1}{\sqrt{M}} \sum_{k=0}^{M-1} r_k$ and $\tilde{v}_0 = \frac{1}{\sqrt{M}} \sum_{k=0}^{M-1} v_k$. This mode captures a weighted mean firing rate, and mean membrane potential across populations. Higher modes contains combination of populations around this mean profile, with increasing oscillatory frequency.

The spectral energy is concentrated in only a few dominant modes, which tend to contain most of the system dynamics.

3.5 Numerical comparison

To assess the practical effectiveness of the modal truncation approach, we simulate a network composed of $M = 50$ populations, each containing 5000 QIF neurons. The connectivity matrix between layers is constructed as:

$$J_{wz} = \begin{cases} 0, & \text{if } |w - z| > R, \\ \frac{(R - |w - z|)}{R^2} J_{\max}, & \text{otherwise,} \end{cases} \quad (3.14)$$

so that J_{wz} forms a triangular profile as a function of the population distance $|w - z|$. The global coupling strength is normalized such that:

$$\sum_{w,z} J_{wz} = J_{\max} = 15.$$

We simulate both (i) the full QIF network and (ii) the corresponding mean-field MPR system with heterogeneous coupling. The latter is expressed in the modal basis associated with the eigenvectors of J , and truncated to retain only the $K = 10$ modes associated with the largest eigenvalues. The eigenvalue repartition weight is largely concentrated in those 10 modes (91%).

Based on the truncated modal representation, we reconstruct the population activity by projecting back into the original basis. As illustrated Fig 3.2, the resulting mean firing rates and membrane potentials (red curves) closely match those obtained

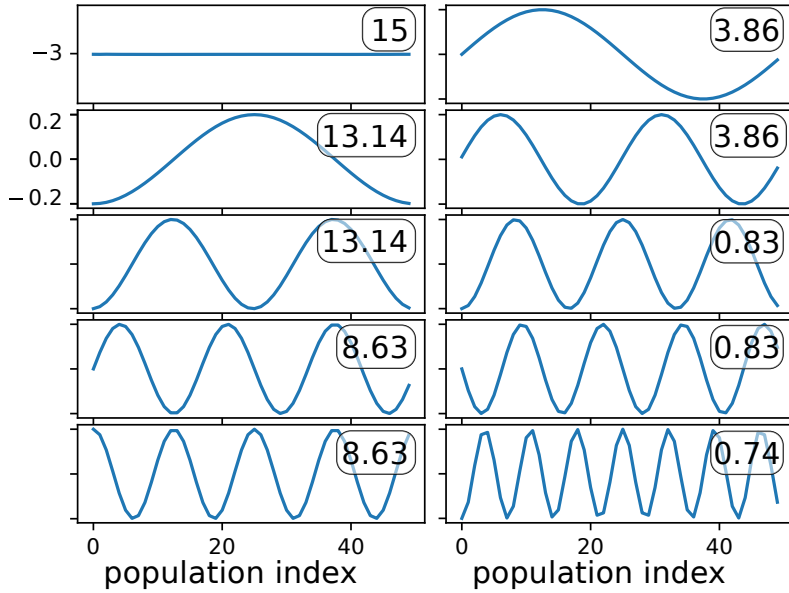


Figure 3.1: Eigenvectors (blue curves) and their eigen-values (top right corner values), of connectivity matrix used for simulations, defined in Eq 3.14 with $R = 10$, $J_{\max} = 15$. Eigenvectors correspond to the discrete Fourier basis, whose profiles exhibit sinusoidal oscillations with increasing spatial frequency. The $k = 0$ mode, associated with the largest eigenvalue ($\lambda_0 = 15$), represents a nearly homogeneous activity pattern across populations.

from the full heterogeneous network (blue curve), for both constant and sinusoidal external input. This demonstrates that only a small number of dominant modes is sufficient to accurately capture the macroscopic network dynamics.

To determine whether the residual mismatch with the full network originates from the modal truncation or from the mean-field reduction itself, we also simulate the full heterogeneous MPR model consisting of $M = 50$ coupled MPR populations, governed by Eq 3.12), Eq 3.13 and connected via the original matrix J .

Remarkably, the truncated modal system provides an excellent match to the full MPR dynamics (see Fig 3.2). This indicates that the dominant eigenmodes capture almost all relevant macroscopic variability, and that the main source of discrepancies with the microscopic QIF simulation stems from our mean-field approximation rather than from modal projection.

Regarding local dynamics, the truncated model inherently loses spatial resolution. Since only ten modes are retained, the reconstructed spatial activity exhibits a corresponding level of precision, characterized by ten distinct bands along the time axis with sharp transitions between them (see Fig 3.3).

3.6 Code and Simulation Details

As in previous sections, we emphasize that reproducibility and shareability are fundamental aspects of scientific research. Accordingly, the code used for all simulations is publicly available at:

<https://gitlab.inria.fr/ahubert/simqif>

The implementation has been optimized for both computational speed and mem-

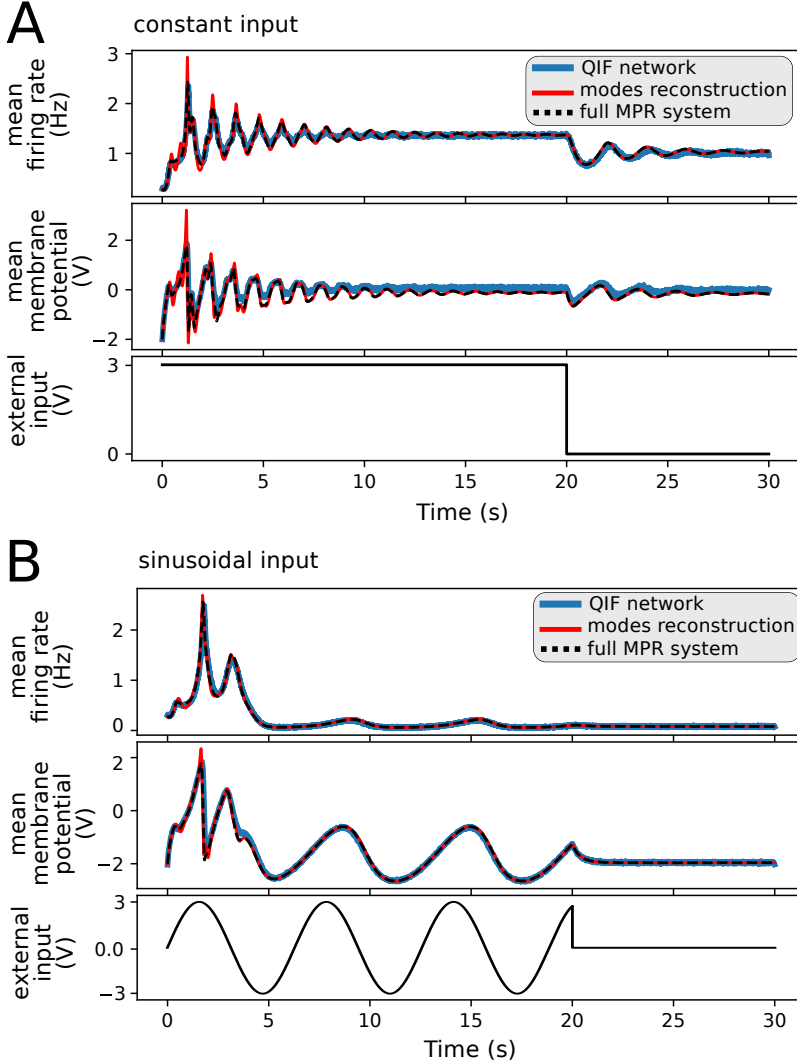


Figure 3.2: A–B. Comparison between the full heterogeneous QIF simulation, the full MPR population model, and the truncated modal reconstruction. The modal approach faithfully reproduces the time evolution of both the mean firing rate $r(t)$ and the mean membrane potential $v(t)$ across the network for multiple types of external input: (A) constant and (B) sinusoidal.

ory efficiency. As a result, the simulations return only population-level quantities, namely the mean firing rate and mean membrane potential. This optimization makes it possible to run the large-scale simulations described below, on standard hardware, with typical runtimes of a few tens of minutes on a laptop equipped with 16 GB of RAM.

3.6.1 Simulations details

QIF Network The QIF network is composed of 50 populations of 5000 QIF neurons (total of 250 000 neurons in the whole network). The connectivity matrix between populations is constructed as (3.14), with $R = 10$. Simulations use a synaptic time constant $\tau_s = 5 \times 10^{-3}$ s. The firing rate is estimated using a temporal smoothing window of 10^{-2} s. The spike threshold and reset values are set to

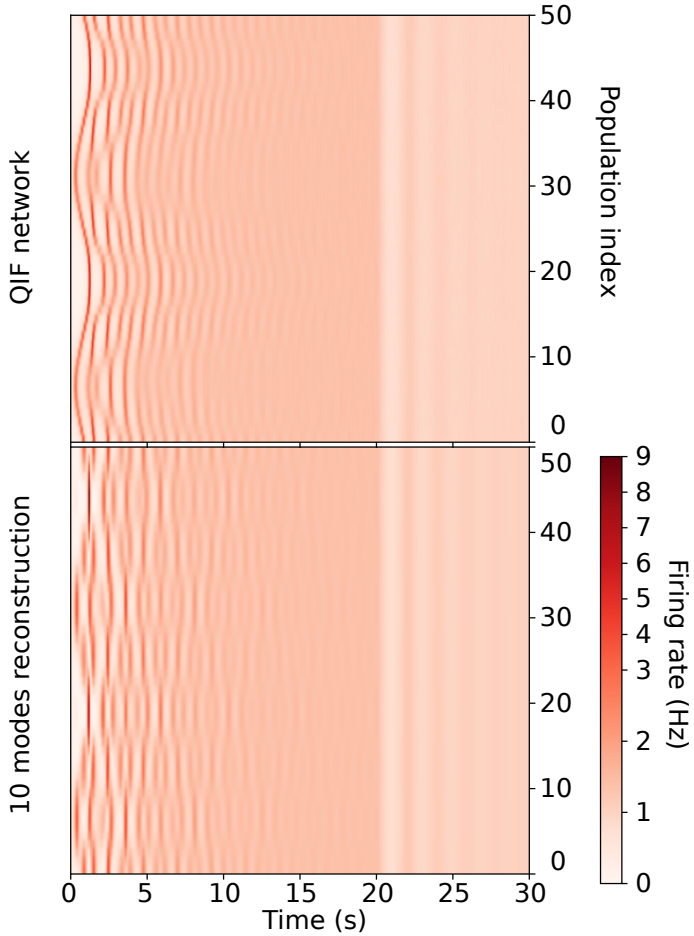


Figure 3.3: Spatiotemporal dynamics of the firing rate across populations for the full QIF network under constant external input. The dominant patterns observed are accurately reconstructed using only the first ten synaptic modes.

$V_t = -V_r = 1000$. Neuron excitabilities are distributed according to a Lorentzian distribution with mean $\bar{\eta} = -5$ and half-width $\Delta = 1$.

Two types of external input are considered: a constant input $I(t) = 3$, and a sinusoidal input $I(t) = 3 \sin(t)$. Initial membrane potentials are drawn from a Cauchy distribution and modulated by a spatial perturbation $4 \sin(4\pi z/N)$, with $z = 1, \dots, N$. Time integration is performed using an explicit Euler scheme with a time step $\Delta t = 5 \times 10^{-5}$ s. Simulations are optimized using `Numba` [55].

MPR System For the MPR population model, the initial firing rate is set to $r_z(0) = 0.29$ for all populations, based on numerical observations. Time integration is performed using the `RK45` solver implemented in `SciPy` [107].

3.7 A Hint on Bifurcation

Here, we present results obtained under alternative simulation conditions. We drop the ring topology, thereby introducing boundary effects, and consider the external input of the form $I(t) = \sin(t) + 1$. We then compare the network dynamics under a small variation of the total synaptic strength J_{\max} .

As shown in Fig. 3.4, a relatively small change in the global coupling strength ($J = 15$ in panel A and $J = 13$ in panel B) leads to a drastic qualitative modification of the network dynamics. This behavior suggests the presence of a critical regime, possibly associated with a bifurcation in the underlying dynamical system. Importantly, in both cases, the truncated modal simulation provides an accurate reconstruction of the fully simulated network dynamics, even close of such a transition.

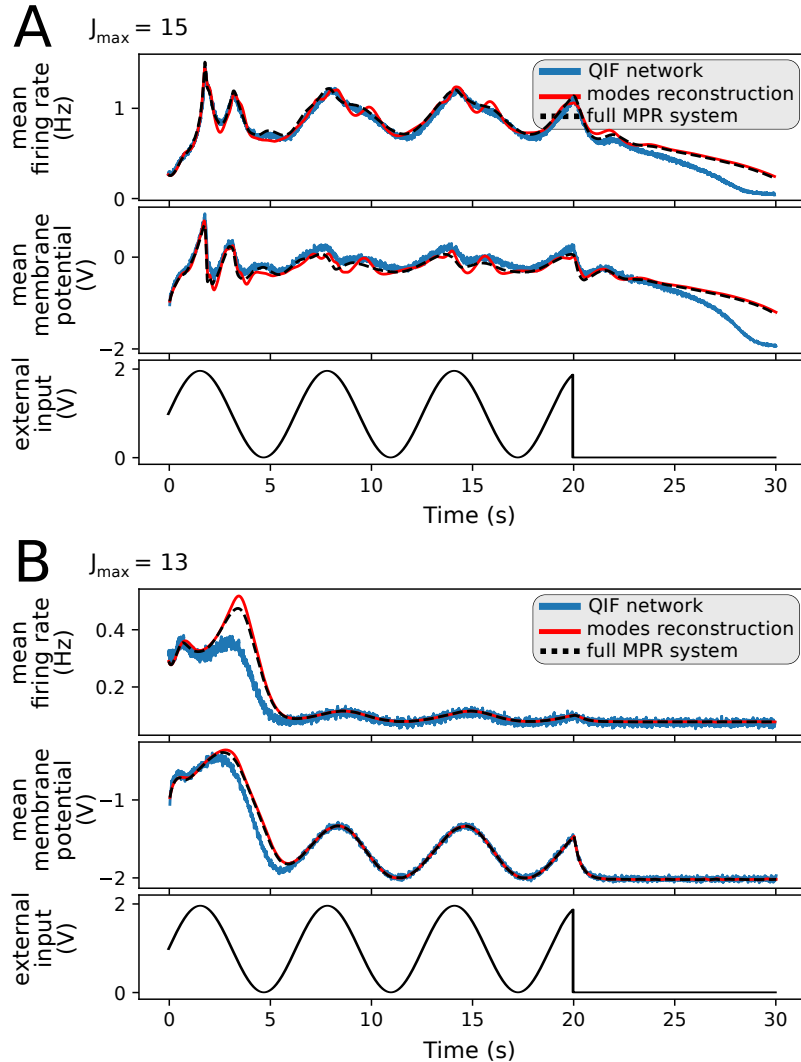


Figure 3.4: A–B. Comparison between the full heterogeneous QIF simulation, the full MPR population model, and the truncated modal reconstruction under non-circulant connectivity and sinusoidal input. A small change in the total synaptic strength ($J_{\max} = 15$ in A, $J_{\max} = 13$ in B) induces a qualitative change in network dynamics, which is captured by the reduced modal system.

Reducing the number of equations required to capture network dynamics is not merely a computational advantage. In order to gain a deeper understanding of how local interactions shape global network behavior, the system must be analytically tractable, which is the core objective of mean-field approaches. By sufficiently reducing the system dimensionality, numerical bifurcation and stability analysis become feasible for our model that accounts for heterogeneous synaptic connectivity

strength.

3.8 Conclusion and Discussion

In this chapter, we proposed a method to approximate the mean dynamics a QIF network while introducing a form of heterogeneity in the synaptic strength. This heterogeneity is done by coupling populations of QIF neurons, by a function of distance. Our methods lies on the combination of two techniques:

1. The Lorentzian Ansatz, which allow to reduce each layer to a system of 2 population equations.
2. The eigen-modes, which project the dynamics on the eigen-spaces of the connectivity matrix. This projection stays accurate even with a truncated number of dimension.

We showed that our method could accurately reproduce the dynamics of a network composed by 50 layers of 5000 QIF neurons, with a triangle connectivity function (see Fig. 3.2). Remarkably, this is done thanks to a system of 20 equations only.

The presented method includes two distinct steps. We seek to emphasize the specific contribution associated with each one.

1. The reduction to a multiple MPR systems is a tremendous gain in computational cost. While the number of operations increase at a square speed of size for the QIF network, the complexity of the MPR system increase with the number of layers only, and is a continuous ode problem, which allow for more integration tools. Yet, large number of layer still prevents for analytical studies, like bifurcation and stability analysis, which are crucial to understand the network’s dynamics.
2. We showed that eigenmode reduction is compatible with mean-field modeling. In addition to further reduces computational cost, this combination calls for further investigations of mean-field models using eigenmode based tools. In particular, the special case of circulant connectivity matrices, which leads to a projection onto the discrete Fourier space, offers a powerful and well-established mathematical framework for the analysis of network dynamics.

This constitutes a first step toward the long-term objective of embedding explicit plasticity rules into mean-field models. Such progress would open the way to understanding how learning emerges at the population level, offering novel perspectives on how multiple distinct paradigms – including one-shot learning – can arise from collective network dynamics.

Our decision to build upon the Montbrió–Pazó–Roxin (MPR) reduction was strongly motivated. The MPR framework has become a reference in mean-field modeling, providing a reliable basis for multiple extensions. More recently, ongoing theoretical work led by our ex fellow post-doc Leonardo Trujillo, has shown that the Lorentzian hypothesis is not simply a convenient reduction technique but the unique and natural candidate, under general mathematical constraints – involving

two-parameter manifold, Möbius maps and Riccati equation). This reinforces its status as the most consistent foundation for future developments.

In the original Lorantzian ansatz work [69], the authors showed that although the analytical results were derived under the assumption of a Lorentzian distribution, numerical simulations with alternative distributions, such as Gaussian, exhibited qualitatively similar behavior. Following this line, numerical exploration will also allow us to test whether the results obtained here remain valid as approximations beyond the Lorentzian case.

General Discussion, Conclusion and Perspectives

During this thesis, we adopted two complementary approaches to address questions related to one-shot-learning. In Chapter 2, the model predicted that eCB-LTP was specifically recruited in the case of short contact during the Sticky Tape Avoidance task. This was tested and observed experimentally, with mice failing to learn through a one-shot learning paradigm, when their eCB pathway was impaired. This provides an additional line of evidence positioning the endocannabinoid pathway as the engram of fast learning. In Chapter 3, we prepared the incorporation of synaptic plasticity rules into the Lorentzian Ansatz framework by studying the implications of introducing one-to-one synaptic strengths in the network. We demonstrated that strong constraints naturally emerge, linking temporal and structural variables in non-trivial ways.

Mechanistic models are powerful tools because of their ability to reproduce experimental data in a biologically meaningful manner. They can then be used not only for explanation but also for prediction. However, this strength comes with complexity and specific challenges. Such models are often highly sensitive to precise parameter values, which questions their robustness across experimental conditions and their ability to generalize phenomena observed in restricted settings. This was precisely the challenge encountered in Chapter 2: the experimental setup used to build and calibrate the model (*ex vivo* slice protocols) differed substantially from the *in vivo* Neuropixel recording conditions. The two contexts yielded spike trains with very different characteristics, and determining when the model remained reliable for prediction was a recurrent issue. Notably, NMDA-mediated depotentiation was identified as very difficult to trigger with the model in its current form, questioning our capability to interpret the predicted NMDA-mediated plasticity on long time scale.

To overcome this difficulty, we explored several approaches to integrate Neuropixel data into the model, originally fit in controlled brain slice condition. In addition, we focused on eCB-related results and introduced intermediate analytical steps to extract meaningful information, such as normalization procedures and z-score based interpretations. An alternative approach would have been to incorporate additional experimental knowledge (e.g., glutamate release dynamics, fatigue, uptake) to refine the model. Such an approach would allow for a more direct integration of the data and a clearer interpretation of the results, but it is also considerably more demanding. In this thesis, we developed a methodology of analysis designed to mitigate these limitations. Future work could take advantage of new bibliographic insights and experimental data to add and refit key processes and thereby improve

the predictive power of the model.

Beyond these methodological considerations, it is important to emphasize the novel contribution of this work. The demonstration of genuine eCB-LTP in the dorsolateral striatum, and its implication in one-shot learning, represents a disruptive finding. Traditionally, endocannabinoids have been associated with LTD in multiple brain regions, such as the hippocampus [15], visual cortex [96], amygdala [4] or Purkinje cells [90]. Although a form of eCB-LTP has been reported in hippocampal CA1, this case differs fundamentally from the cortico-striatal mechanism, as it arises from the depotentiation of inhibitory synapses rather than direct excitatory strengthening [57, 114].

In parallel, paradigms reminiscent of one-shot learning have been described in the hippocampus under the framework of one-trial memory. While such processes are indeed induced after a single encounter with a novel context, they remain primarily cognitive, relating to episodic memory, and differ from the procedural learning observed in the sticky tape avoidance task. In this case, the underlying substrate is also distinct and require NMDA receptor at presynaptic sites [72]. Taken together, these comparisons further underline the novelty of cortico-striatal eCB-LTP as a candidate engram for rapid procedural learning.

Another natural direction concerns the further development of **Synacomp**. Currently, the library constitutes a structured version of the code developed for this thesis, but it still lacks the full range of analyses implemented here. Beyond my commitment to reproducibility, the effort invested in the numerical framework was strongly motivated by the needs of our collaborators in Venance’s team. Performing numerical analyses on such large datasets requires coding practices including good organization, modularity, and optimization. Experimental biologists often rely on collaboration to fully exploit the potential of their data, and I knew that similar protocols were planned for the future. Extending and adapting **Synacomp** for our collaborators use will ensure that it becomes a sustainable tool beyond the scope of this thesis.

One of the major strengths of **Synacomp** is the possibility of using and adding any synaptic model while retaining the automation and organizational features of the framework. However, such integration requires time development, and in this thesis we restricted ourselves to the implementation of the model by Cui *et al.* (2016). A key future objective will be to extend **Synacomp** by incorporating additional models and, importantly, by making this integration step more accessible to external users.

Theoretical and numerical approaches can stand on their own, independently of immediate experimental information. Thanks to that, they may notably guide future experiments by providing consistent hypotheses and predictions. In Chapter 3, we tackled the one-shot-learning problem from a mean-field perspective. Such approach allows to investigate how macroscopic network dynamics emerge from local description. This area still offers a wide range of directions to explore. At the most fundamental level, by building from alternative neuronal models beyond QIF or LIF, broadening the analytical foundations of mean-field approaches. More specific refinements also remain crucial, such as the accurate modeling of refractory periods or the integration of EPSPs. In addition, the inclusion of non-neuronal elements –notably astrocytes– is increasingly necessary, as they are now recognized to play crucial roles in neural dynamics and plasticity across multiple scales.

Numerous methods have been proposed to address the incorporation of synaptic plasticity into mean-field models. For example, a form of plasticity observed during working memory was implemented within the Lorentzian Ansatz framework, allowing for heterogeneous coupling between populations [101]. However, this strategy increases the dimensionality of the system, as the number of differential equations to be solved scales with the number of considered populations, which limit the number of considered population. This remains conceptually different from the one-to-one synaptic plasticity we seek to explore. Gast *et al.* (2021) [33] emphasized the scarcity of proposals explicitly incorporating plasticity at the synaptic level. The authors remark, that plasticity occurring at presynaptic terminals like vesicle depletion, is excluded from models of short-term adaptation [34]. They acknowledged the difficulty of obtaining an exact derivation and instead proposed accurate approximations. To this day, an exact mean-field formulation for QIF neuron networks that explicitly integrates a genuine synaptic plasticity rule so remains elusive. Another important line of work is Phase-Difference-Dependent Plasticity (PDDP), first introduced by Seliger *et al.* (2002) [93]. This approach leverages the conformal transformation between QIF and Kuramoto models to map the problem onto a network of oscillators. PDDP aims to replicate STDP-like mechanisms within this framework, and exact derivations are indeed possible [27]. Nevertheless, introducing PDDP breaks the conformal equivalence between Kuramoto oscillators and QIF neurons. PDDP does not yet provide a formal counterpart for oscillatory networks equivalent to the role of STDP in QIF networks, leaving our central problem unresolved.

The work presented during chapter 3 is only a first step toward the goal to understand how learning can emerge from a network level. We believe this step is an essential one. The decision to build upon the Montbrió-Pazó-Roxin framework is strongly motivated. The MPR reduction has established itself as a reference in the field of mean-field modeling, serving as a foundation for numerous extensions. But more importantly, recent ongoing research conducted by Leonardo Trujillo and Hugues Berry has demonstrated that the Lorentzian Ansatz is not merely a convenient reduction method, but the unique and natural candidate given theoretical constraints. As such, it provides the most consistent foundation for future extensions. At this stage, the proposed formulation for introducing heterogeneity in synaptic weights primarily provides a gain in computational efficiency for numerical simulations. However, its main interest lies in opening a new avenue toward analytically tractable reduced descriptions of such networks, a direction that I intend to pursue in future work.

Annexe

Annexe: Montbrió–Pazó–Roxin

Trivial solutions We can start by solving Eq 1.20 in the trivial case $I = 0$ and $\partial_t \rho = 0$. Corresponding to a situation where there are no external input, and the system is in its stationary state and do not evolve in time. Eq 1.20 simplifies to:

$$\frac{\partial}{\partial V} [(V^2 + \eta + Jr)\rho] = 0 \Leftrightarrow (3.15)$$

$$(V^2 + \eta + Jr)\rho = c_0, \Leftrightarrow (3.16)$$

$$p = c_0(V^2 + \eta + Jr)^{-1} \quad (3.17)$$

with $c_0 = \frac{\sqrt{\eta+Jr}}{\pi}$ an initial condition, ensuring that the solution is scaled as a probability density function. The solution has the form of a Lorentzian distribution:

$$\frac{1}{\pi} \frac{x}{(V - y)^2 + x^2}. \quad (3.18)$$

with $x = \sqrt{\eta + Jr}$ and $y = 0$.

From this special solution, we can intuit and remark that any Lorentzian distribution solve Eq 1.17.

Firing rate In the continuous description, the firing rate is defined as the probability flux crossing the threshold V_t . With the chosen infinite threshold, the expression of firing rate is finally given by:

$$r(t, \eta) = \lim_{V \rightarrow +\infty} \rho(V|\eta, t) \frac{dV}{dt}, \quad (3.19)$$

$$= \lim_{V \rightarrow +\infty} \frac{1}{\pi} \frac{x(V^2 + \eta + I + Jr)}{(V - y)^2 + x^2}, \quad (3.20)$$

$$= \lim_{V \rightarrow +\infty} \frac{1}{\pi} \frac{x(1 + \frac{1}{V^2}(\eta + I + Jr))}{1 - \frac{2y}{V} + \frac{y^2}{V^2} + \frac{x^2}{V^2}}, \quad (3.21)$$

$$= \boxed{\frac{1}{\pi} x(t, \eta)}. \quad (3.22)$$

as $x(1 + \frac{1}{V^2}(\eta + I + Jr)) \xrightarrow[V \rightarrow +\infty]{} x$ at nominator and $1 - \frac{2y}{V} + \frac{y^2}{V^2} + \frac{x^2}{V^2} \xrightarrow[V \rightarrow +\infty]{} 1$ at denominator.

The mean firing rate of the whole network is then given by:

$$\begin{aligned} r(t) &= \int r(t, \eta) g(\eta) d\eta, \\ &= \boxed{\frac{1}{\pi} \int x(t, \eta) g(\eta) d\eta}. \end{aligned} \quad (3.23)$$

Mean membrane potential Let's compute the mean membrane potential given by:

$$v(t, \eta) = \int \rho(V|\eta, t) V dV. \quad (3.24)$$

However this integral is ill-defined because of Lorentzian's heavy tail. $v(t, \eta)$ can still be characterized by its Cauchy principal value (p.v), thus

$$v(t, \eta) = p.v \left(\int \rho(V|\eta, t) V dV \right). \quad (3.25)$$

$$= \lim_{R \rightarrow +\infty} \int_{-R}^R \rho(V|\eta, t) V dV. \quad (3.26)$$

$$\int_{-R}^R \rho(V|\eta, t) V dV = \int_{-R}^R \frac{1}{\pi} \frac{Vx}{(V-y)^2 + x^2} dV \quad (3.27)$$

$$= \underbrace{\frac{x}{\pi} \int_{-R}^R \frac{(V-y)}{(V-y)^2 + x^2} dV}_{(A)} - \underbrace{\frac{x}{\pi} \int_{-R}^R \frac{-y}{(V-y)^2 + x^2} dV}_{(B)} \quad (3.28)$$

For part (A), we can apply the variable change $\bar{V} = V - y$, thus (A) become:

$$\int_{-R-y}^{R-y} \frac{\bar{V}}{\bar{V}^2 + x^2} d\bar{V} = \int_{-(R-y)}^{R-y} \frac{\bar{V}}{\bar{V}^2 + x^2} d\bar{V} + \int_{-R-y}^{-R+y} \frac{\bar{V}}{\bar{V}^2 + x^2} d\bar{V}. \quad (3.29)$$

First part is the integral of an even function on a symmetric segment around 0, then is equal to 0. Second part is equivalent to $y \frac{1}{\bar{V}}$ and converge to 0 for \bar{V} great enough. Finally, (A) $\rightarrow 0$ when $R \rightarrow +\infty$.

Part (B) can be solved explicitly:

$$\int_{-R}^R \frac{-y}{(V-y)^2 + x^2} dV = \left[\frac{y}{x} \arctan\left(\frac{y-V}{x}\right) \right]_{-R}^R, \quad (3.30)$$

$$\xrightarrow[R \rightarrow +\infty]{ } \frac{y}{x} \left(\arctan\left(\frac{-\infty}{x}\right) - \arctan\left(\frac{+\infty}{x}\right) \right), \quad (3.31)$$

$$= \frac{y}{x} \pi. \quad (3.32)$$

We replace expression found for (A) and (B) at the limit in Eq 3.28).

$$v(t, \eta) = 0 + \frac{x}{\pi} \frac{y}{x} \pi = \boxed{y(t, \eta)}. \quad (3.33)$$

Special case of Lorentzian excitability We suppose that excitability η is distributed according to a Lorentzian distribution

$$g(\eta) = \frac{1}{\pi} \frac{\Delta}{(\eta - \bar{\eta})^2 + \Delta^2}. \quad (3.34)$$

Let's demonstrate a powerful property of Lorentzian distributions. We want to compute the integral:

$$\int_{\mathbb{R}} f(\eta)g(\eta) d\eta. \quad (3.35)$$

with $g(\eta)$ defined as above, and $f(\eta)$ an holomorphic function without singularity, on which we will add some hypothesis when it will be needed.

First, we extent $g(\eta)$ to its analytical continuation, so it is now an holomorphic defined on the whole complex plane. On \mathbb{C} , $g(\eta)$ admit two singularities $\eta_- = \bar{\eta} - i\Delta$ and $\eta_+ = \bar{\eta} + i\Delta$. We denote C_R the arc of radius R in the lower half plane, closed by the segment $[-R, R]$. We remark that our integral of interest appears when we consider the limit $R \rightarrow +\infty$ of the integral on C_R :

$$\int_{C_R} f(z)g(z) dz = \int_{\mathbb{R}} f(z)g(z) dz + \int_0^\pi f(Re^{i\theta})g(Re^{i\theta}) d\theta. \quad (3.36)$$

As C_R is a positivly oriented simple closed curve, the Residue theorem says that:

$$\int_{C_R} f(z)g(z) dz = 2\pi i \sum_{z_* \in S} \text{Res}(fg, z_*) \quad (3.37)$$

were S is the set of singularities of $f.g$ inside C_R , and $\text{Res}(fg, z_*)$ is the residue of function $f.g$, evaluated at the singularity z_* . In this case, $S = \eta_-$.

$$\text{Res}(fg, \eta_-) = \lim_{\eta \rightarrow \eta_-} (\eta - \eta_-) f.g(\eta). \quad (3.38)$$

$$(\eta - \eta_-) f(\eta) g(\eta) = (\eta - \eta_-) f(\eta) \frac{1}{\pi} \frac{\Delta}{(\eta - \bar{\eta})^2 + \Delta^2}, \quad (3.39)$$

$$= (\eta - \eta_-) f(\eta) \frac{1}{\pi} \frac{\Delta}{(\eta - \eta_-)(\eta - \eta_+)}, \quad (3.40)$$

$$= f(\eta) \frac{1}{\pi} \frac{\Delta}{\eta - \eta_+}. \quad (3.41)$$

We take the limit $\eta \rightarrow \eta_-$, and conclude:

$$\text{Res}(fg, \eta_-) = f(\eta_-) \frac{1}{\pi} \frac{\Delta}{(\bar{\eta} + i\Delta) - (\bar{\eta} - i\Delta)}, \quad (3.42)$$

$$= -f(\eta_-) \frac{i}{2\pi}. \quad (3.43)$$

Injecting into equation (3.37):

$$\int_{C_R} f(z)g(z) dz = 2\pi i f(\eta_-) \frac{-i\Delta}{2\pi} = \boxed{f(\eta_-)}. \quad (3.44)$$

We still need to compute

$$\int_0^\pi f(Re^{i\theta})g(Re^{i\theta}) d\theta. \quad (3.45)$$

We assume that $f(z)g(z)$ is bounded, and that $RM_R \rightarrow 0$, for $R \rightarrow +\infty$, were $M_R = \sup_{z \in \gamma_R} |f(z)g(z)|$, and γ_R is the arc of radius R in the lower half plane.

$$\left| \int_0^\pi f(Re^{i\theta})g(Re^{i\theta}) d\theta \right| \leq \int_0^\pi |f(Re^{i\theta})g(Re^{i\theta})| d\theta, \quad (3.46)$$

$$= \int_0^\pi \frac{1}{\pi} \frac{|f(Re^{i\theta})|\Delta}{|(Re^{i\theta} - \bar{\eta})^2| + \Delta^2} d\theta, \quad (3.47)$$

$$\leq \int_0^\pi \frac{1}{\pi} \frac{|f_{\max,R}|\Delta}{(R - \bar{\eta})^2 + \Delta^2} dx\theta, \quad (3.48)$$

$$= \frac{1}{\pi} \frac{\pi R |f_{\max,R}| \Delta}{(R - \bar{\eta})^2 + \Delta^2}, \quad (3.49)$$

$$\sim \Delta \frac{|f_{\max,R}|}{R}, \quad \text{for } R \rightarrow +\infty. \quad (3.50)$$

In order to simplify Eq. 3.50 and explicitly solve Eq. 3.36, we assume that f grows sufficiently slowly compared to $1/x$. Under this assumption, Eq. 3.50 converges to zero, and consequently so does Eq. 3.45.

Combined with Eq 3.44 and Eq 3.36 we conclude that

$$\boxed{\int_{\mathbb{R}} f(z)g(z) dz = f(\bar{\eta} - i\Delta)} \quad (3.51)$$

Solved firing rate The previous result can be used to compute explicitly Eq 3.23 and gloabl mean membrane potential accros η .

$$r(t) = \frac{1}{\pi} \int_{\mathbb{R}} x(t, \eta) g(\eta) d\eta, \quad (3.52)$$

$$= \frac{1}{\pi} x(t, \bar{\eta} - i\Delta). \quad (3.53)$$

$$v(t) = \int_{\mathbb{R}} y(y, \eta) g(t, \eta) d\eta, \quad (3.54)$$

$$= y(y, \bar{\eta} - i\Delta). \quad (3.55)$$

We have

$$\pi r(t) + iv(t) = w(t, \bar{\eta} - i\Delta) \quad (3.56)$$

When replacing in Eq 1.27:

$$\pi \partial_t r(t) + i \partial_t v(t) = i(\bar{\eta} - i\Delta + Jr - (\pi r(t) + iv(t))^2 + I(t)), \quad (3.57)$$

$$= \Delta + 2\pi r(t)v(t) + i(\pi^2 v(t)^2 - r(t)^2 + Jr + \bar{\eta} + I(t)) \quad (3.58)$$

By identification we obtain the following system:

$$\boxed{\begin{cases} \partial_t r(t) &= \frac{\Delta}{\pi} + 2r(t)v(t), \\ \partial_t v(t) &= v(t)^2 - \pi^2 r(t)^2 + Jr + \bar{\eta} + I(t) \end{cases}} \quad (3.59)$$

Bibliography

- [1] L.F Abbott. Lapicque's introduction of the integrate-and-fire model neuron (1907). *Brain Research Bulletin*, 50(5):303–304, 1999.
- [2] Jung-Hyuck Ahn, Jee Young Sung, Thomas McAvoy, Akinori Nishi, Veerle Janssens, Jozef Goris, Paul Greengard, and Angus C. Nairn. The b"/pr72 sub-unit mediates ca2+ dependent dephosphorylation of darpp-32 by protein phosphatase 2a. *Proceedings of the National Academy of Sciences*, 104(23):9876–9881, 2007.
- [3] Alfonso Araque, Giorgio Carmignoto, Philip G. Haydon, Stéphane H.R. Oliet, Richard Robitaille, and Andrea Volterra. Gliotransmitters travel in time and space. *Neuron*, 81(4):728–739, 2014.
- [4] Shahnaz C. Azad, Krisztina Monory, Giovanni Marsicano, Benjamin F. Cravatt, Beat Lutz, Walter Zieglgänsberger, and Gerhard Rammes. Circuitry for associative plasticity in the amygdala involves endocannabinoid signaling. *Journal of Neuroscience*, 24(44):9953–9961, 2004.
- [5] Frederico A.C. Azevedo, Ludmila R.B. Carvalho, Lea T. Grinberg, José Marcelo Farfel, Renata E.L. Ferretti, Renata E.P. Leite, Wilson Jacob Filho, Roberto Lent, and Suzana Herculano-Houzel. Equal numbers of neuronal and nonneuronal cells make the human brain an isometrically scaled-up primate brain. *Journal of Comparative Neurology*, 513(5):532–541, 2009.
- [6] Danielle Bassett and Olaf Sporns. Network neuroscience. *Nature Neuroscience*, 20(3):353–364, 2017.
- [7] Hadley C. Bergstrom, Anna M. Lipkin, Abby G. Lieberman, Courtney R. Pinard, Ozge Gunduz-Cinar, Emma T. Brockway, William W. Taylor, Mio Nonaka, Olena Bukalo, Tiffany A. Wills, F. Javier Rubio, Xuan Li, Charles L. Pickens, Danny G. Winder, and Andrew Holmes. Dorsolateral striatum engagement interferes with early discrimination learning. *Cell Reports*, 23(8):2264–2272, 2018.
- [8] Guoqiang Bi and Mu-ming Poo. Synaptic modifications in cultured hippocampal neurons: Dependence on spike timing, synaptic strength, and postsynaptic cell type. *The Journal of neuroscience : the official journal of the Society for Neuroscience*, 18:10464–72, 01 1999.
- [9] Katie C. Bittner, Aaron D. Milstein, Christine Grienberger, Sandro Romani, and Jeffrey C. Magee. Behavioral time scale synaptic plasticity underlies CA1 place fields. *Science*, 357(6355):1033–1036, 2017.

BIBLIOGRAPHY

- [10] T. V. P. Bliss, G. L. Collingridge, R. G. M. Morris, and Roger A. Nicoll. Expression mechanisms underlying long-term potentiation: a postsynaptic view. *Philosophical Transactions of the Royal Society of London. Series B: Biological Sciences*, 358(1432):721–726, 2003.
- [11] Romain Brette and Wulfram Gerstner. Adaptive exponential integrate-and-fire model as an effective description of neuronal activity. *Journal of neurophysiology*, 94:3637–42, 12 2005.
- [12] Michael A. Buice and Carson C. Chow. Dynamic finite size effects in spiking neural networks. *PLOS Computational Biology*, 9(1):1–21, 01 2013.
- [13] György Buzsáki, Costas A. Anastassiou, and Christof Koch. The origin of extracellular fields and currents — EEG, ECoG, LFP and spikes. *Nature Reviews Neuroscience*, 13(6):407–420, 2012.
- [14] Pablo E. Castillo, Thomas J. Younts, Andrés E. Chávez, and Yuki Hashimoto-dani. Endocannabinoid signaling and synaptic function. *Neuron*, 76(1):70–81, 2012.
- [15] Vivien Chevaleyre and Pablo E. Castillo. Heterosynaptic ltd of hippocampal gabaergic synapses: A novel role of endocannabinoids in regulating excitability. *Neuron*, 38(3):461–472, 2003.
- [16] Vivien Chevaleyre, Kanji A. Takahashi, and Pablo E. Castillo. Endocannabinoid-mediated synaptic plasticity in the cns. *Annual Review of Neuroscience*, 29(Volume 29, 2006):37–76, 2006.
- [17] Ami Citri and Robert Malenka. Synaptic plasticity: Multiple forms, functions, and mechanisms. *Neuropsychopharmacology : official publication of the American College of Neuropsychopharmacology*, 33:18–41, 02 2008.
- [18] Lee Cossell, Maria Francesca Iacaruso, David R. Muir, Rebecca Houlton, Elie Sader, Ho Ko, Sonja B. Hofer, and Thomas D. Mrsic-Flogel. Functional organization of excitatory synaptic strength in primary visual cortex. *Nature*, 518(7539):399–403, 2015.
- [19] Yihui Cui, Vincent Paillé, Hao Xu, Stéphane Genet, Bruno Delord, Elodie Fino, Hugues Berry, and Laurent Venance. Endocannabinoids mediate bidirectional striatal spike-timing-dependent plasticity. *The Journal of Physiology*, 593(13):2833–2849, 2015.
- [20] Yihui Cui, Ilya Prokin, Alexandre Mendes, Hugues Berry, and Laurent Venance. Robustness of stdp to spike timing jitter. *Scientific Reports*, 8, 05 2018.
- [21] Yihui Cui, Ilya Prokin, Hao Xu, Bruno Delord, Stephane Genet, Laurent Venance, and Hugues Berry. Endocannabinoid dynamics gate spike-timing dependent depression and potentiation. *eLife*, 5:e13185, feb 2016.
- [22] Peter Dayan and L. F. Abbott. *Theoretical Neuroscience: Computational and Mathematical Modeling of Neural Systems*. MIT Press, Cambridge, MA, 2001.

- [23] Maurizio De Pitta, Mati Goldberg, Vladislav Volman, Hugues Berry, and Eshel Ben-Jacob. Glutamate regulation of calcium and ip₃ oscillating and pulsating dynamics in astrocytes. *Journal of Biological Physics*, 35, 12 2009.
- [24] Gustavo Deco, Viktor Jirsa, Peter Robinson, Michael Breakspear, and Karl Friston. The dynamic brain: From spiking neurons to neural masses and cortical fields. *PLoS computational biology*, 4:e1000092, 02 2008.
- [25] Alain Destexhe, Zachary F. Mainen, and Terrence J. Sejnowski. Fast kinetic models for simulating ampa, nmda, gabaaand gababreceptors. In James M. Bower, editor, *The Neurobiology of Computation*, pages 9–14, Boston, MA, 1995. Springer US.
- [26] Alain Destexhe, Zachary F. Mainen, and Terrence J. Sejnowski. Kinetic models of synaptic transmission. In Christof Koch and Idan Segev, editors, *Methods in Neuronal Modeling: From Ions to Networks*, pages 1–25. MIT Press, Cambridge, MA, 2nd edition, 1998.
- [27] Benoit Duchet, Christian Bick, and Áine Byrne. Mean-field approximations with adaptive coupling for networks with spike-timing-dependent plasticity. *Neural Computation*, 35(9):1481–1528, 08 2023.
- [28] Gaute T. Einevoll, Christoph Kayser, Nikos K. Logothetis, and Stefano Panzeri. Modelling and analysis of local field potentials for studying the function of cortical circuits. *Nature Reviews Neuroscience*, 14(11):770–785, 2013.
- [29] G. Bard Ermentrout and Nancy Kopell. Parabolic bursting in an excitable system coupled with a slow oscillation. *SIAM Journal on Applied Mathematics*, 46(2):233–253, 1986.
- [30] C. J. Fontaine, E. L. Gräfe, C. Pinar, I. Bonilla-Del Río, P. Grandes, and B. R. Christie. Endocannabinoid receptors contribute significantly to multiple forms of long-term depression in the rat dentate gyrus. *Learning & Memory*, 27(9):380–389, 2020.
- [31] Robert C. Froemke, Ishan A. Tsay, Mohamad Raad, John D. Long, and Yang Dan. Contribution of individual spikes in burst-induced long-term synaptic modification. *Journal of Neurophysiology*, 95(3):1620–1629, 2006. PMID: 16319206.
- [32] Min Fu and Yi Zuo. Experience-dependent structural plasticity in the cortex. *Trends in Neurosciences*, 34(4):177–187, 2011.
- [33] Richard Gast, Thomas R. Knösche, and Helmut Schmidt. Mean-field approximations of networks of spiking neurons with short-term synaptic plasticity. *Phys. Rev. E*, 104:044310, Oct 2021.
- [34] Richard Gast, Helmut Schmidt, and Thomas R. Knösche. A mean-field description of bursting dynamics in spiking neural networks with short-term adaptation. *Neural Computation*, 32(9):1615–1634, 09 2020.

BIBLIOGRAPHY

- [35] Gregory L. Gerdeman, Jennifer Ronesi, and David M. Lovinger. Postsynaptic endocannabinoid release is critical to long-term depression in the striatum. *Nature Neuroscience*, 5(5):446–451, 2002.
- [36] Wulfram Gerstner and Werner M. Kistler. Leaky integrate-and-fire model with absolute refractory period. <https://lcnwww.epfl.ch/gerstner/SPNM/node26.html>.
- [37] Wulfram Gerstner, Werner M. Kistler, Richard Naud, and Liam Paninski. *Neuronal Dynamics: From Single Neurons to Networks and Models of Cognition*. Cambridge University Press, Cambridge, UK, 2014.
- [38] Steve Goldstein, Detlef Bockenhauer, Ita O’Kelly, and Noam Zilberman. Potassium channels and the kcnk family of two-p-domain subunits. *Nature reviews Neuroscience*, 2:175–84, 04 2001.
- [39] Stephen Gotts. Incremental learning of perceptual and conceptual representations and the puzzle of neural repetition suppression. *Psychonomic Bulletin & Review*, 23, 05 2015.
- [40] Michael Graupner and Nicolas Brunel. Stdp in a bistable synapse model based on camkii and associated signaling pathways. *PLoS computational biology*, 3:e221, 12 2007.
- [41] Michael Graupner and Nicolas Brunel. Calcium-based plasticity model explains sensitivity of synaptic changes to spike pattern, rate, and dendritic location. *Proceedings of the National Academy of Sciences*, 109(10):3991–3996, 2012.
- [42] Ann Graybiel and Scott Grafton. The striatum: Where skills and habits meet. *Cold Spring Harbor perspectives in biology*, 7, 08 2015.
- [43] Xu Hao, Sylvie Perez, Amandine Cornil, Bérangère Detraux, Ilya Prokin, Yihui Cui, Bertrand Degos, Hugues Berry, Alban de Kerchove d’Exaerde, and Laurent Venance. Dopamine–endocannabinoid interactions mediate spike-timing-dependent potentiation in the striatum. *Nature Communications*, 9(1):4118, 2018.
- [44] Donald O. Hebb. *The Organization of Behavior: A Neuropsychological Theory*. Wiley, New York, 1949.
- [45] Valerie Hedges. *Introduction to Neuroscience*. Michigan State University Libraries, East Lansing, MI, 2022. Open-access first edition.
- [46] Alan L. Hodgkin and Andrew F. Huxley. Currents carried by sodium and potassium ions through the membrane of the giant axon of *Loligo*. *The Journal of Physiology*, 116(4):449–472, 1952.
- [47] Eugene M. Izhikevich. *Dynamical Systems in Neuroscience: The Geometry of Excitability and Bursting*. MIT Press, Cambridge, MA, 2007.
- [48] CE Jahr and CF Stevens. A quantitative description of nmda receptor-channel kinetic behavior. *Journal of Neuroscience*, 10(6):1830–1837, 1990.

- [49] Sheena A. Josselyn and Susumu Tonegawa. Memory engrams: Recalling the past and imagining the future. *Science*, 367(6473):eaaw4325, 2020.
- [50] James J. Jun, Nicholas A. Steinmetz, Joshua H. Siegle, Daniel J. Denman, Marius Bauza, Brian Barbarits, Albert K. Lee, Costas A. Anastassiou, Alexandru Andrei, Çağatay Aydin, Mladen Barbic, Timothy J. Blanche, Vincent Bonin, João Couto, Barundeb Dutta, Sergey L. Gratiy, Diego A. Gutnisky, Michael Häusser, Bill Karsh, Peter Ledochowitsch, Carolina Mora Lopez, Catalin Mitelut, Silke Musa, Michael Okun, Marius Pachitariu, Jan Putzeys, P. Dylan Rich, Cyrille Rossant, Wei lung Sun, Karel Svoboda, Matteo Carandini, Kenneth D. Harris, Christof Koch, John O’Keefe, and Timothy D. Harris. Fully integrated silicon probes for high-density recording of neural activity. *Nature*, 551(7679):232–236, 2017.
- [51] Dimitri M. Kullmann and Fredrik Asztely. Extrasynaptic glutamate spillover in the hippocampus: evidence and implications. *Trends in Neurosciences*, 21(1):8–14, 1998.
- [52] David A. Kupferschmidt, Konrad Juczewski, Guohong Cui, Kevin A. Johnson, and David M. Lovinger. Parallel, but dissociable, processing in discrete corticostriatal inputs encodes skill learning. *Neuron*, 96(2):476–489.e5, 2017.
- [53] Yoshiki Kuramoto. *Chemical Oscillations, Waves, and Turbulence*. Springer-Verlag, 1984.
- [54] Laetitia Lalla, Pavel E. Rueda-Orozco, Maria-Teresa Jurado-Parras, Andrea Brovelli, and David Robbe. Local or not local: Investigating the nature of striatal theta oscillations in behaving rats. *eNeuro*, 4(5):ENEURO.0128–17.2017, 2017.
- [55] Siu Kwan Lam, Antoine Pitrou, and Stanley Seibert. Numba: a llvm-based python jit compiler. In *Proceedings of the Second Workshop on the LLVM Compiler Infrastructure in HPC*, LLVM ’15, New York, NY, USA, 2015. Association for Computing Machinery.
- [56] Sylvain Lefort, Christian Tomm, J. Carlos Floyd Sarria, and Carl C. H. Petersen. The excitatory neuronal network of the c2 barrel column in mouse primary somatosensory cortex. *Neuron*, 61(2):301–316, 2009.
- [57] Fouad Lemtiri-Chlieh and Eric S. Levine. 2-ag and anandamide enhance hippocampal long-term potentiation via suppression of inhibition. *Frontiers in Cellular Neuroscience*, Volume 16 - 2022, 2022.
- [58] Luciana M. Leo and Mary E. Abood. Cb1 cannabinoid receptor signaling and biased signaling. *Molecules*, 26(17), 2021.
- [59] John Lisman, Ryohei Yasuda, and Sridhar Raghavachari. Mechanisms of camkii action in long-term potentiation. *Nature reviews. Neuroscience*, 13:169–82, 02 2012.
- [60] Christian Lüscher and Robert C. Malenka. Nmda receptor-dependent long-term potentiation and long-term depression (ltp/ltd). *Cold Spring Harbor Perspectives in Biology*, 4(6), 2012.

BIBLIOGRAPHY

- [61] Zachary Mainen, Roberto Malinow, and Karel Svoboda. Synaptic calcium transients in single spines indicate that nmda receptors are not saturated. *Nature*, 399:151–5, 06 1999.
- [62] Robert C. Malenka and Mark F. Bear. Ltp and ltd: An embarrassment of riches. *Neuron*, 44(1):5–21, 2004.
- [63] Eve Marder and Jean-Marc Goaillard. Variability, compensation and homeostasis in neuron and network function. *Nature Reviews Neuroscience*, 7(7):563–574, 2006.
- [64] Henry Markram, Joachim Lübke, Michael Frotscher, and Bert Sakmann. Regulation of synaptic efficacy by coincidence of postsynaptic aps and epsps. *Science*, 275(5297):213–215, 1997.
- [65] S.J. Martin and R.G.M. Morris. New life in an old idea: The synaptic plasticity and memory hypothesis revisited. *Hippocampus*, 12(5):609–636, 2002.
- [66] José A. Matta and Gerard P. Ahern. Voltage is a partial activator of rat thermosensitive trp channels. *The Journal of Physiology*, 585(2):469–482, 2007.
- [67] Aaron D. Milstein, Yiding Li, Katie C. Bittner, Christine Grienberger, Ivan Soltesz, Jeffrey C. Magee, and Sandro Romani. Bidirectional synaptic plasticity rapidly modifies hippocampal representations. *eLife*, 10:e73046, 2021.
- [68] Hannah R Monday, Mathieu Bourdenx, Bryen A Jordan, and Pablo E Castillo. Cb₁-receptor-mediated inhibitory ltd triggers presynaptic remodeling via protein synthesis and ubiquitination. *eLife*, 9:e54812, sep 2020.
- [69] Ernest Montbrió, Diego Pazó, and Alex Roxin. Macroscopic description for networks of spiking neurons. *Physical Review X*, 5(2):021028, 2015.
- [70] Catherine Morris and Harold Lecar. Voltage oscillations in the barnacle giant muscle fiber. *Biophysical Journal*, 35(1):193–213, 1981.
- [71] J. Nagumo, S. Arimoto, and S. Yoshizawa. An active pulse transmission line simulating nerve axon. *Proceedings of the IRE*, 50(10):2061–2070, 1962.
- [72] Kazu Nakazawa, Linus D Sun, Michael C Quirk, Laure Rondi-Reig, Matthew A Wilson, and Susumu Tonegawa. Hippocampal ca3 nmda receptors are crucial for memory acquisition of one-time experience. *Neuron*, 38(2):305–315, 2003.
- [73] Richard Naud and Wulfram Gerstner. *The Performance (and Limits) of Simple Neuron Models: Generalizations of the Leaky Integrate-and-Fire Model*, pages 163–192. Springer Netherlands, Dordrecht, 2012.
- [74] Daniel H. O'Connor, Gayle M. Wittenberg, and Samuel S.-H. Wang. Graded bidirectional synaptic plasticity is composed of switch-like unitary events. *Proceedings of the National Academy of Sciences*, 102(27):9679–9684, 2005.

- [75] Katerina D. Oikonomou, Mandakini B. Singh, Enas V. Sterjanaj, and Srdjan D. Antic. Spiny neurons of amygdala, striatum, and cortex use dendritic plateau potentials to detect network up states. *Frontiers in Cellular Neuroscience*, Volume 8 - 2014, 2014.
- [76] Marius Pachitariu, Cyrille Rossant, Nick Steinmetz, Jennifer Colonell, Adrian Gopnik Bondy, Olivier Winter, kushbang, Jai Bhagat, Mari Sosa, Dan O'Shea, Jose Guzman, Kouichi C. Nakamura, geffenlab, Paul Botros, Rajat Saxena, Alan Liddell, John Pellman, Martin Spacek, bryzgalovdm, carsen stringer, daniel denman, Dimokratis Karamanlis, and Maxime Beau. Mouse-land/kilosort: Kilosort 2.5, January 2021.
- [77] Marius Pachitariu, Nicholas Steinmetz, Shabnam Kadir, Matteo Carandini, and Harris Kenneth D. Kilosort: realtime spike-sorting for extracellular electrophysiology with hundreds of channels. *bioRxiv*, 2016.
- [78] Bjørn Pedersen, Morten Buch-Pedersen, Jens Preben Morth, Michael Palmgren, and Poul Nissen. Crystal structure of the plasma membrane proton pump. *Nature*, 450:1111–4, 08 2008.
- [79] Elodie Perrin and Laurent Venance. Bridging the gap between striatal plasticity and learning. *Current Opinion in Neurobiology*, 54:104–112, 2019.
- [80] Carl C. H. Petersen, Robert C. Malenka, Roger A. Nicoll, and John J. Hopfield. All-or-none potentiation at ca3-ca1 synapses. *Proceedings of the National Academy of Sciences*, 95(8):4732–4737, 1998.
- [81] Bastian Pietras and Andreas Daffertshofer. Network dynamics of coupled oscillators and phase reduction techniques. *Physics Reports*, 819:1–105, 2019. Network dynamics of coupled oscillators and phase reduction techniques.
- [82] Charlotte Piette, Yihui Cui, Nicolas Gervasi, and Laurent Venance. Lights on endocannabinoid-mediated synaptic potentiation. *Frontiers in Molecular Neuroscience*, Volume 13 - 2020, 2020.
- [83] Charlotte Piette, Arnaud Hubert, Sylvie Perez, Hugues Berry, Jonathan Touboul, and Laurent Venance. Striatal endocannabinoid-long-term potentiation mediates one-shot learning. *bioRxiv*, 2024.
- [84] Charlotte Piette, Jonathan Touboul, and Laurent Venance. Engrams of fast learning. *Frontiers in Cellular Neuroscience*, 14:575915, 2020.
- [85] Panayiota Poirazi, Terrence Brannon, and Bartlett Mel. Arithmetic of sub-threshold synaptic summation in a model ca1 pyramidal cell. *Neuron*, 37:977–87, 04 2003.
- [86] Liston K. Purvis and Robert J. Butera. Ionic current model of a hypoglossal motoneuron. *Journal of Neurophysiology*, 93(2):723–733, 2005. PMID: 15653786.
- [87] P.A. Robinson, X. Zhao, K.M. Aquino, J.D. Griffiths, S. Sarkar, and Grishma Mehta-Pandejee. Eigenmodes of brain activity: Neural field theory predictions and comparison with experiment. *NeuroImage*, 142:79–98, 2016.

BIBLIOGRAPHY

- [88] Cyrille Rossant, Alessio Buccino, Michael Economo, Cedric Gestes, Dan Goodman, Max Hunter, Shabnam Kadir, Christopher Nolan, Martin Spacek, and Nick Steinmetz. phy: interactive visualization and manual spike sorting of large-scale ephys data. <https://github.com/cortex-lab/phy>. Version 2.0b4, BSD-3-Clause License.
- [89] Bernardo L. Sabatini and Karel Svoboda. Analysis of calcium channels in single spines using optical fluctuation analysis. *Nature*, 408, 2000.
- [90] Patrick K. Safo and Wade G. Regehr. Endocannabinoids control the induction of cerebellar ltd. *Neuron*, 48(4):647–659, 2005.
- [91] Daniel L. Schacter, James Eric Eich, and Endel Tulving. Richard semon’s theory of memory. *Journal of Verbal Learning and Verbal Behavior*, 17(6):721–743, 1978.
- [92] Almut Schüz and Günther Palm. Density of neurons and synapses in the cerebral cortex of the mouse. *Journal of Comparative Neurology*, 286(4):442–455, 1989.
- [93] Philip Seliger, Stephen C. Young, and Lev S. Tsimring. Plasticity and learning in a network of coupled phase oscillators. *Phys. Rev. E*, 65:041906, Mar 2002.
- [94] Harel Z. Shouval, Mark F. Bear, and Leon N Cooper. A unified model of nmda receptor-dependent bidirectional synaptic plasticity. *Proceedings of the National Academy of Sciences*, 99(16):10831–10836, 2002.
- [95] Per Jesper Sjöström, Gina G. Turrigiano, and Sacha B. Nelson. Rate, timing, and cooperativity jointly determine cortical synaptic plasticity. *Neuron*, 32(6):1149–1164, 2001.
- [96] Per Jesper Sjöström, Gina G. Turrigiano, and Sacha B. Nelson. Endocannabinoid-dependent neocortical layer-5 ltd in the absence of post-synaptic spiking. *Journal of Neurophysiology*, 92(6):3338–3343, 2004. PMID: 15240760.
- [97] Spencer Smith, Ikuko Smith, Tiago Branco, and Michael Häusser. Dendritic spikes enhance stimulus selectivity in cortical neurons. *Nature*, 503, 10 2013.
- [98] Sen Song, Kenneth Miller, and L.F. Abbott. Competitive hebbian learning through spike timing-dependent plasticity. *Nature neuroscience*, 3:919–26, 10 2000.
- [99] Katarzyna Starowicz, Santosh Nigam, and Vincenzo Di Marzo. Biochemistry and pharmacology of endovanilloids. *Pharmacology , Therapeutics*, 114(1):13–33, 2007.
- [100] Rafael Sánz-Galvez, Dominic falardeau, Arlette Kolta, and Yanis Inglebert. The role of astrocytes from synaptic to non-synaptic plasticity. *Frontiers in Cellular Neuroscience*, 18, 10 2024.

- [101] Halgurd Taher, Alessandro Torcini, and Simona Olmi. Exact neural mass model for synaptic-based working memory. *PLOS Computational Biology*, 16(12):1–42, 12 2020.
- [102] Shiming Tang, Yimeng Zhang, Zhihao Li, Ming Li, Fang Liu, Hongfei Jiang, and Tai Sing Lee. Large-scale two-photon imaging revealed super-sparse population codes in the v1 superficial layer of awake monkeys. *eLife*, 7:e33370, apr 2018.
- [103] Yong Tang, Jens Nyengaard, Didima de Groot, and Hans Gundersen. Total regional and global number of synapses in the human brain neocortex. *Synapse*, 41:258–73, 10 2001.
- [104] Romain Tavenard, Johann Faouzi, Gilles Vandewiele, Felix Divo, Guillaume Androz, Chester Holtz, Marie Payne, Roman Yurchak, Marc Rußwurm, Kushal Kolar, and Eli Woods. Tslearn, a machine learning toolkit for time series data. *Journal of Machine Learning Research*, 21(118):1–6, 2020.
- [105] Dan Valsky, Shai Heiman Grosberg, Zvi Israel, Thomas Boraud, Hagai Bergman, and Marc Deffains. What is the true discharge rate and pattern of the striatal projection neurons in Parkinson’s disease and dystonia ? *eLife*, 9:e57445, 2020.
- [106] Silvana Valtcheva, Vincent Paillé, Yulia Dembitskaya, Sylvie Perez, Giuseppe Gangarossa, Elodie Fino, and Laurent Venance. Developmental control of spike-timing-dependent plasticity by tonic gabaergic signaling in striatum. *Neuropharmacology*, 121:261–277, 2017.
- [107] Pauli Virtanen, Ralf Gommers, Travis E. Oliphant, Matt Haberland, Tyler Reddy, David Cournapeau, Evgeni Burovski, Pearu Peterson, Warren Weckesser, Jonathan Bright, Stéfan J. van der Walt, Matthew Brett, Joshua Wilson, K. Jarrod Millman, Nikolay Mayorov, Andrew R. J. Nelson, Eric Jones, Robert Kern, Eric Larson, C J Carey, İlhan Polat, Yu Feng, Eric W. Moore, Jake VanderPlas, Denis Laxalde, Josef Perktold, Robert Cimrman, Ian Henriksen, E. A. Quintero, Charles R. Harris, Anne M. Archibald, Antônio H. Ribeiro, Fabian Pedregosa, Paul van Mulbregt, and SciPy 1.0 Contributors. SciPy 1.0: Fundamental algorithms for scientific computing in python. *Nature Methods*, 17:261–272, 2020.
- [108] Maxwell B. Wang, Julia P. Owen, Pratik Mukherjee, and Ashish Raj. Brain network eigenmodes provide a robust and compact representation of the structural connectome in health and disease. *PLOS Computational Biology*, 13(6):1–20, 06 2017.
- [109] Hugh R. Wilson and Jack D. Cowan. Excitatory and inhibitory interactions in localized populations of model neurons. *Biophysical Journal*, 12(1):1–24, 1972.
- [110] Hugh R. Wilson and Jack D. Cowan. A mathematical theory of the functional dynamics of cortical and thalamic nervous tissue. *Kybernetik*, 13(2):55–80, 1973.

BIBLIOGRAPHY

- [111] Bryony Laura Winters and Christopher Walter Vaughan. Mechanisms of endocannabinoid control of synaptic plasticity. *Neuropharmacology*, 197:108736, 2021.
- [112] John A. Wolf, Jason T. Moyer, Maciej T. Lazarewicz, Diego Contreras, Marianne Benoit-Marand, Patricio O'Donnell, and Leif H. Finkel. Nmda/ampa ratio impacts state transitions and entrainment to oscillations in a computational model of the nucleus accumbens medium spiny projection neuron. *Journal of Neuroscience*, 25(40):9080–9095, 2005.
- [113] Stephen H. Wright. Generation of resting membrane potential. *Advances in Physiology Education*, 28(4):139–142, 2004. PMID: 15545342.
- [114] Jian-Yi Xu and Chu Chen. Endocannabinoids in synaptic plasticity and neuroprotection. *The Neuroscientist*, 21(2):152–168, 2015. PMID: 24571856.
- [115] Henry Yin and Barbara Knowlton. The role of the basal ganglia in habit formation. *Nature reviews. Neuroscience*, 7:464–76, 07 2006.
- [116] Henry Yin, Shweta Mulcare, Monica Hilário, Emily Clouse, Terrell Holloway, Margaret Davis, Anita Hansson, David Lovinger, and Rui Costa. Dynamic reorganization of striatal circuits during the acquisition and consolidation of a skill. *Nature neuroscience*, 12:333–41, 03 2009.
- [117] Robert S. Zucker and Wade G. Regehr. Short-term synaptic plasticity. *Annual Review of Physiology*, 64(Volume 64, 2002):355–405, 2002.